University of New Mexico
UNM Digital Repository

3-1-2013

Compressive cooperative obstacle mapping with see-through capabilities in mobile networks

Alejandro Gonzalez Ruiz

Recommended Citation

Alejandro Gonzalez Ruiz

Candidate

Electrical and Computer Engineering

Department

This dissertation is approved, and it is acceptable in quality and form for publication:

Approved by the Dissertation Committee:

Yasamin Mostofi
, Chairperson

Chaouki Abdallah

Majeed Hayat

Shuang Luan

_____

_____

_____

_____

_____

Compressive Cooperative Obstacle Mapping with See-Through Capabilities in Mobile Networks

by

Alejandro González Ruiz

B.S., Electronics Engineering, Universidad del Valle de Guatemala, 2006
M.S., Electrical Engineering, University of New Mexico, 2009

DISSERTATION

Submitted in Partial Fulfillment of the
Requirements for the Degree of

Doctor of Philosophy
Engineering

The University of New Mexico

Albuquerque, New Mexico

December, 2012

Dedication

To my mother Emma

Acknowledgments

I would like to thank my advisor, Professor Yasamin Mostofi. Working under her guidance her has been a true honor. Her passion, dedication and enthusiasm for research have been an example to follow. I thank her for all the encouragement, support, kindness and guidance that she has given me during all these years.

My gratitude also goes to Dr. Chaouki Abdallah and Dr. Majeed Hayat for always taking time out of their busy schedules to help me and share their expertise in order to make this work better. I thank also Dr. Shuang Luan for accepting to be part of my dissertation committee and for useful comments.

I would also like to express my gratitude to the Fulbright Foreign Student program for its financial support during my Master's degree. I also want to thank Dr. Rafael Fierro, Dr. Wennie Shu, Dr. Balu Santhanam and Dr. Nasir Ghani for sharing their expertise through their classes and for their support.

I also thank my family, especially my mother Emma and my father Rodolfo, my sisters Paola and Matty, and their families for their love, encouragement and for always being there for me.

Finally, I would like to thank my friends Luis Rivera, José Velasquez, Kim Nichols, Jorge Crichigno, Antonio Hurtado, Jorge Pezoa, my colleagues and friends at our lab especially Mehrzad Malmirchegini, Alireza Ghaffarkhah and Yuan Yan and everyone who in one way or another has helped me develop this work.

Compressive Cooperative Obstacle Mapping with See-Through Capabilities in Mobile Networks

by

Alejandro González Ruiz

B.S., Electronics Engineering, Universidad del Valle de Guatemala, 2006

M.S., Electrical Engineering, University of New Mexico, 2009

Ph.D., Engineering, University of New Mexico, 2012

Abstract

Mobile intelligent networks can play a key role in many different areas from emergency response, surveillance and security, and battlefield operations to smart homes and factories and environmental monitoring. Accurate mapping of the obstacles/objects in the environment is key to the robust operation of unmanned autonomous networks as it is an integral part of navigation and path planning. In the robotics community, the problem of mapping has been widely explored. However, in the existing mapping approaches, only areas that can be directly sensed by the sensors are mapped. In several scenarios, it may be necessary to have *see-through* capabilities and map occluded objects without direct sensing. For instance, the robots may need to build an understanding of the objects inside a room before entering it. Having see-through capabilities can also reduce the overall mapping time and energy in any networked robotic operation.

In this dissertation, we consider a mobile robotic network that is tasked with building a map of the objects/obstacles in an environment including the occluded ones. Since we

vi

are interested in see-through capabilities, in our framework the robots cooperate to build the map based on a small number of *wireless channel measurements*. This allows the robots to efficiently map occluded areas of the workspace. By using the recent results in the area of compressive sensing, we exploit the sparse representation of the map in space, wavelet or spatial variations, in order to build it with minimal sensing. We discuss three mapping strategies based on frequency sampling, coordinated space and random space measurements and show the underlying tradeoffs of the possible sampling, sparsity and reconstruction techniques. For instance, we shed light on the optimum number of angular motion directions of the robots, as well as the choice of the angles, to distribute a given number of wireless measurements. We establish that the total number of available channel measurements should be distributed over a small number of angles, that is bigger than or equal to the number of jump (discontinuity) angles of the structure, with a preference given to the angles of jumps.

We then propose an integration of our wireless-based mapping framework with existing mapping techniques in order to map more complicated structures. More specifically, we propose an integrated framework where laser measurements are used to map the visible parts of the environment (the parts that can be sensed directly by the laser scanners) using occupancy grid mapping approaches. The parts that can not properly be mapped are then identified and mapped based on wireless channel measurements. We show how to integrate occupancy grid mapping with two reconstruction methods based on wireless measurements and compressive sensing: Bayesian compressive sensing (BCS) and total variation (TV) minimization. We compare the performance of these two integrated approaches and shed light on the underlying tradeoffs. Finally, we propose an adaptive path planning strategy that utilizes the current estimate of uncertainty to collect wireless measurements that are more informative for obstacle mapping. Overall, our integrated framework enables mapping occluded structures that can not be mapped with laser scanner data alone or a small number of wireless measurements.

Most importantly, we show how to design an experimental robotic platform in order to implement our approach. We then show the performance of our framework in efficiently mapping a number of real obstacles including blocked ones. Our experimental results confirm the feasibility of the proposed framework for mapping structures that include occluded parts.

Contents

Contents

Contents

Contents

List of Figures

Chapter 1

Introduction

Over the past few years, considerable progress has been made in the area of mobile sensor and robotic networks [9–18]. Mobile robotic networks can play a key role in areas such as emergency response, surveillance and security, and battlefield operations. In order for a such a network to be autonomous and robust, accurate mapping of obstacles/objects is needed. The obstacle/object map can be a 2D (or 3D) grid map of the environment, where we have zeros at locations where there is no obstacle and non-zero values at obstacle locations. In several scenarios, it may be necessary to have *see-through capabilities* and map the objects without direct sensing. For instance, the robots may need to build an understanding of the objects inside a room, before entering it. See-through mapping furthermore allows the robots to map the obstacles for navigation purposes, without having to sense them directly. This can be of particular interest in several scenarios such as search and rescue, surveillance or threat detection. It also saves the overall obstacle mapping time and energy in any cooperative robotic application, by eliminating the need for direct sensing of all the objects.

In this dissertation, we consider cooperative mapping of obstacles (including occluded ones) in robotic networks based on a small number of *wireless transmissions*. In the wire-

less communication literature, it is well-established that the shadowing component of a wireless transmission contains implicit information on the objects located on the path between the transmitter and receiver [1]. Thus, wireless measurements between pairs of robots can possibly be utilized for obstacle mapping, with the advantage that it can allow the robots to map the areas that are not directly sensed (mapping of occluded parts). This has opened a new and different venue for the mapping of obstacles as shown by Mostofi [6–8] and is the approach we shall pursue in this thesis.

In general, extracting the obstacle information, without making a prohibitive number of wireless transmissions, is considerably challenging due to all the propagation phenomena. In order to address this and enable the mapping based on a small number of wireless transmissions, we utilize the new theories of *compressive sensing* [3, 4]. The Nyquist-Shannon sampling theorem [19] revolutionized several different fields by showing that, under certain conditions, it is indeed possible to reconstruct a uniformly sampled signal perfectly. The new theory of compressive sensing (also known by other terms such as compressed sampling, compressive sensing or sparse sensing) shows that under certain conditions, it is possible to reconstruct a signal from a considerably incomplete set of observations, i.e. with a number of measurements much less than predicted by the Nyquist-Shannon theorem [3, 4]. This opens new and fundamentally different possibilities in terms of information gathering and processing in mobile networks, as we shall utilize in this thesis.

We next summarize the related work in the literature and continue with a summary of our contributions.

1.1 Prior Work

1.1.1 Obstacle Mapping in Robotics Literature

In the robotics community, the problem of mapping has been widely explored [20–23]. However, in the current approaches using sonar/laser sensors, only areas that are directly sensed by the sensors are mapped. Depending on whether the positions and orientations of the robots are known, the mapping problem can be tackled using different techniques. In mapping with known poses, occupancy grid mapping approaches [23, 24] have been proposed. The objective there is to build a grid map of the obstacles by sequentially updating the posterior of having an obstacle in each cell of a grid, based sensory (sonar or laser) measurements.

In mapping with unknown poses, the Simultaneous Localization and Mapping (SLAM) approaches are used to incrementally build a map of the environment, while estimating the location of the robot within the map [25–30]. The SLAM problem is among the most challenging problems in autonomous robotics. Several techniques based on using extended Kalman filters (EKF) [31] and Rao-Blackwell particle filters [32–35] have been proposed by the researchers to solve this problem. Both occupancy grid maps and landmark maps (a set of known landmarks in the environment) can be considered in SLAM, depending on the algorithm used and type of the environment [25]. Approaches based on generating an occupancy map address reducing the uncertainty of direct sensing [36, 37]. One common limitation of all these approaches is that only areas that can be directly sensed by the sensors are mapped.

Another set of approaches are based on the Next Best View (NBV) problem [38–42]. In NBV approaches, the aim is to move to the positions "good" for sensing by guiding the vehicles to the perceived next safest area (area with the most visibility) based on the current map [38]. However, similar to the approaches above, areas that are not sensed directly are not mapped in NVB.

1.1.2   Through-the-wall Radar for Detection

Though-the wall radar (TWR) is mostly focused on the detection of a single occluded object, for instance a person or a weapon which is occluded by walls. The most common approaches for TWR are multilateration [43–45], and synthetic aperture radar (SAR) [46, 47]. In multilateration, range measurements from multiple sensors are correlated to specific points in the image. Spatial diversity is used to have a large set of Transmitter/Receiver combinations. SAR is an extension to the multilateration concept where a complex matched filter is used. A key tool for successful TWR is the use of diversity [48]. Possible ways of attaining diversity include: frequency, sensor position, angle, waveform choice, and multiple-input multiple-output (MIMO). A popular approach for TWR is the use of a model-based reconstruction in which a priori structure information is utilized [48].

Ultra-wideband (UWB) has also been shown to yield good detection properties for TWR. For instance, in [49] the authors use an UWB MIMO phased array radar system to perform real-time detection of (possibly occluded) moving objects. To detect movement, the radar system subtracts previously-acquired raw data sets from real-time readings and then displays the image of the difference. In other words, this approach requires coherent change detection, i.e. previous measurements of the scene of interest without the target, so the changes can be detected. Furthermore, the approach is focused on detection of single targets, not on mapping the layout of an environment. In [50], a handheld device is used to detect motion of individuals. However, it similarly requires prior knowledge of building models to develop a ground truth to compare the predicted and the real measurements. Along the same line, in [51], authors use a transmitter that is buried underground and several fixed receivers on the surface to detect underground tunnels/facilities using radar.

In summary, a common characteristic of TWR is that it either requires a priori measurements when the target is not present or some knowledge on the dielectric properties of the first layer of occluders (or transparent first layer).

1.1.3   Wireless-based Obstacle Mapping

In [6–8], Mostofi proposed a framework for see-through mapping based on using very few wireless channel measurements and by exploiting the sparse representation of the map in another domain such as wavelet or spatial variations. In this thesis, we follow this line of work. On a related topic, there are also a number of concurrent recent papers on detecting an object using fixed sensors. In [52, 53], for instance, the authors build a network of 28 fixed sensors in order to detect presence of a person. The framework is based on making wireless measurements between pairs of sensors. Then the goal is to roughly track a person as opposed to building a map of obstacles. There is a need for prior learning in the area of interest as well. As such, [52, 53] is more on detecting an obstruction to a wireless signal as opposed to obstacle mapping with minimal measurements.

We next summarize the contributions of this thesis.

1.2   Contributions of this Dissertation

This dissertation is on the development of a framework for building obstacle maps with see-through capabilities. We discuss three mapping strategies based on frequency sampling, coordinated space and random space measurements. Then, we use compressive sensing in order to exploit the sparse representation of the map in space, wavelet or spatial variations, so that the map can be built with a small number of wireless measurements. We furthermore show the underlying tradeoffs of the possible sampling, sparsity and reconstruction techniques using both simulation and experimental results. We thoroughly compare the performance of our random and coordinated sampling strategies. Along this line, we discuss the optimum number of angular motion directions of the robots, as well as the choice of the angles, in order to distribute a given number of wireless measurements. We establish that the total number of available channel measurements should be

distributed along a small number of angles, that is bigger than or equal to the number of jump angles of the structure, with a preference given to the angles of jumps.

We then propose a novel integrated occupancy grid and wireless-based mapping approach for mapping with see-through capabilities. Our proposed approach uses occupancy grid mapping (with known poses or with unknown poses using SLAM) to map the parts of the environment that can be sensed directly by the laser scanners of the robots. The parts of the map that can not be seen by the laser scanners are then mapped based on the wireless channel measurements and by using our proposed wireless-based mapping framework. We rigorously show how to integrate occupancy grid mapping with two different wireless-based compressive map reconstruction methods: our previous TV-based approach and a probabilistic Bayesian Compressive Sensing-based approach. More specifically, we propose an integrated probabilistic approach based on utilizing Bayesian Compressive Sensing (BCS) for extracting the map of the occluded parts from wireless measurements. We then compare the performance of our BCS-based integrated framework with that of our TV-based integration and shed light on the underlying tradeoffs. For instance, our results indicate that the integrated BCS-based method is more appropriate for mapping based on random wireless measurements while TV-based integrated approach performs better with coordinated wireless measurements.

Another contribution of this thesis is to propose adaptive sample collection strategies that can enable pairs of robots to efficiently choose the positions from which to take the next wireless measurements such that the mapping performance is improved. More specifically, we propose two strategies: *ad-hoc* and *variance-based*. The variance-based approach, for instance, utilizes the current estimated variance of our integrated BCS approach to identify the map cells with highest uncertainty and plans the motion of the robots to cover those cells next.

Finally, we also show how to design an experimental robotic platform in order to implement the proposed mapping approaches. We then show the performance of our frame-

work in efficiently mapping a number of real obstacles (including blocked ones) using our robotic testbed. We discuss hardware requirements, such as the use of directional adaptive antennas, in order to mitigate the effects of multipath fading. Our experimental results demonstrate the feasibility and good performance of the proposed framework for mapping real structures that have occluded parts.

1.3   Dissertation Overview

This dissertation is organized as follows: Chapter 2 serves as an overview of the characterization of the underlying multi-scale dynamics of a wireless link, the knowledge of which would be useful for the subsequent chapters. We further describe our experimental setup for automating the channel measurement process, using our robots. In Chapter 3 we give a brief summary of the area of compressive sampling, as relevant to our proposed framework and explain our wireless-based mapping approach. In Chapter 4, we discuss different possibilities for compressive sampling and reconstruction and show their underlying tradeoffs. We furthermore show how to properly design a robotic platform to implement our proposed mapping framework. In that chapter, we then validate our results through simulations and experimental data gathered with our robots. In Chapter 5, we propose an integrated framework for mapping with see-through capabilities using both laser and wireless channel measurements. In this framework, laser measurements are used to map the visible parts of the environment while the rest of the map (e.g. the occluded parts) are then mapped based on our wireless-based mapping framework. We also propose an adaptive exploration strategy which enables a pair of robots to efficiently collect wireless measurements that are more informative for see-through mapping. We conclude in Chapter 6.

Chapter 2

Wireless Channel Modeling and Experimental Validation

This chapter serves as an overview of the characterization of the underlying multi-scale dynamics of a wireless link. By utilizing the knowledge available in the wireless communication literature, we summarize a probabilistic framework for the characterization of the three dynamics of a wireless channel. We furthermore describe our experimental setup for automating the channel measurement process, using our robots. In this chapter, we use this experimental setup to confirm the probabilistic channel characterization framework, by making an extensive number of channel measurements. The three wireless channel dynamics are then used in the next chapters as the basis for the sensing model of our wireless-based compressive mapping framework.

In a realistic communication settings, such as an urban area or an indoor environment, Line-Of-Sight (LOS) communication between a wireless transmitter and a receiver may not be possible due to the existence of several objects that can attenuate,reflect, diffract or block the transmitted signal. The received signal power typically experiences considerable variations and can change drastically in even a small distance. As an example, consider

8

Fig. 1, where channel measurements in our building are shown. It can be seen that channel can change drastically even within small distance intervals. Thus, communication between mobile units can degrade due to factors such as shadowing, fading or distance-dependent path loss [1], which can impact the overall performance of the network considerably.
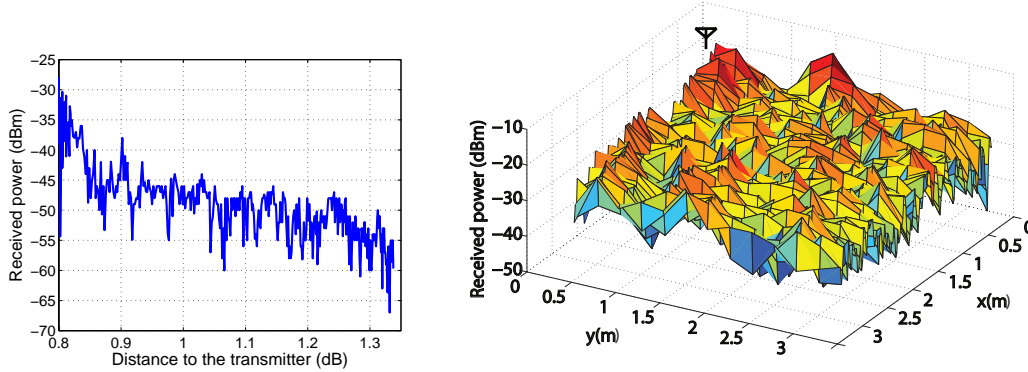
Figure 2.1: Sample channel measurements in (left) 1D and (right) 2D.

Exact mathematical characterization of a wireless channel is extremely challenging, due to its time-varying and unpredictable nature. One can possibly solve Maxwell's equations with proper boundary conditions that reflect all the physical constraints of the environment. However, such calculation is difficult and requires the knowledge of several geometric and dielectric properties of the environment, which is not easily available. In wireless communication systems, it is therefore common to model the channel probabilistically, with the goal of capturing its underlying dynamics. The utilized probabilistic models are the results of analyzing several empirical data over the years. In general, a communication channel between two mobile robotic platforms can be modeled as a multi-scale dynamical system with three major dynamics: *small-scale fading (multipath fading)*, *shadowing (shadow fading)* and *path loss*. These three dynamics are key to the realistic characterization of the performance of networked robotic systems. We start this chapter by providing a description of our robotic testbed, which was used to automate the channel measurement process.

2.1 An Experimental Robotic Platform for Channel Measurement Collection

The analyses of this dissertation are all accompanied by experimental validations. As such, in this section we briefly describe our experimental testbed. This can help the readers understand the conditions under which our measurements are collected so they can reproduce the results.

Traditionally, there has been considerable interest in measurement and characterization of the received communication signal strength in the context of cellular systems [54–58]. Automating the measurement process, however, has been difficult in the past due to the lack of an automated mobile system. For outdoor measurements, vehicle-mounted transceivers have been used in some experiments [57, 58]. Collecting indoor measurements, however, is more challenging. For instance, in [54], the authors use a cart to move the receiver and transmitter units, resulting in a positioning accuracy of about 10 cm, which may not suffice depending on the required analysis. Using rails with motorized positioners is another common approach for moving the transmitter/receiver [59]. The advent of robotic networks facilitates the design of an automated measurement system considerably and allows for collecting measurements with flexibility, reconfigurability and a high spatial resolution. As such, we have developed a robotic testbed to automate our channel measurement process. The testbed consists of two Pioneer 3-AT (P3-AT) mobile robots from MobileRobots Inc. [60], each equipped with an onboard PC, an IEEE 802.11g (WLAN) card and various sensors used for localization and obstacle avoidance. Each robot acts as a mobile transceiver and can record its received signal strength as it moves. The resulting data set is then used in this chapter for the characterization of wireless channels for mobile robotic networks and most importantly, for wireless-based obstacle mapping in the later chapters of this dissertation.

Next, we explain the hardware and software components of our testbed in more details,

including our software-based controller and navigation infrastructure.

2.1.1   Hardware Architecture

Our setup consists of two P3-AT mobile robots [60]. Pioneer 3-AT is a high performance robotic platform from MobileRobots, which is a popular and reliable team performer for indoor, outdoor and rough-terrain projects. We equipped each robot with a removable electromechanical fixture to possibly hold a directional antenna. Fig. 2.2 (right) shows one of our robots in its original form, while the left figure shows the robot with a directional antenna mounted on it. A block diagram of the hardware architecture of one of the robots is shown in Fig. 2.3. The remote PC is a supervising unit, in charge of planning the motion of the robots and collecting the signal strength data from the robots. Each P3-AT base comes with an onboard PC104 and a Renesas SH7144-based microcontroller platform to control the motors, actuators and sensors. MobileRobots provides a C/C++ application programming interface (API) library called ARIA [60] to program and control the robot via its onboard microcontroller platform. We also developed a servo mechanism to intelligently rotate the directional antenna of the robot. The servo mechanism is controlled by the onboard PC of the robot through a microcontroller-based external hardware. We make use of Hitec HS-7955TG high performance coreless digital servo motors with $180°$ rotation in our servo mechanism. As for the directional antennas, we use a GD24-15 2.4GHz parabolic grid antenna from Laird Technologies [61]. This model has a 15 dBi gain with $21°$ horizontal and $17°$ vertical beamwidth and is suitable for IEEE 802.11b/g applications (Fig. 2.2-left).

Robot Localization

Accurate localization of the robots is crucial to proper channel measurement and analysis. For instance, characterizing the spatial correlation of different channel dynamics requires

Figure 2.2: (left) Pioneer 3-AT robot equipped with a servo mechanism and a directional antenna. (right) Pioneer 3-AT robot equipped with an omnidirectional antenna.

accurate position information. In our testbed, each robot uses both the onboard gyroscope and the wheel encoders for localization. Since the localization error is additive in time, the calibration unit resets the gyroscope and the wheel encoders periodically, after an adjustable number of steps. Currently, our localization error is less than 2.5 cm for every 1 m of a straight line movement. If additional accuracy is needed over longer distances, more advanced localization strategies, from the robotic literature, can also be utilized. Alterna-
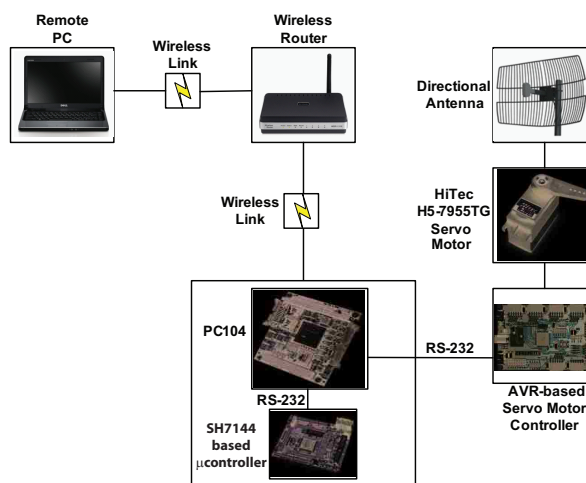
Figure 2.3: A block diagram of the hardware architecture of one of the robots.

tively, a long route can be divided into shorter sub-routes and the robot can be manually repositioned at the beginning of each sub-route to provide a better overall accuracy.

2.1.2 Software Architecture

A high-level schematic of the software architecture is shown in Fig. 2.4. The software-based control infrastructure consists of two application layers running on different machines: The *robot-side* application runs on the onboard PC of the robot whereas the *client-side* application runs on the remote PC. The robot-side application is developed as a TCP/IP server and is in charge of reading the sensory data, sending it to the client-side application, receiving the high-level control of motion/antenna angle commands from the client-side application and executing the commands. The client-side application, which runs as a TCP/IP client for robot-side application, is in charge of supervising the entire operation, planning the motion, generating the high-level control commands to be sent to the robots and collecting the signal strength data from the robots for future processing. The microcontroller of the servo mechanism is also programmed to decode the rotation commands and send the corresponding Pulse Width Modulation (PWM) signals to the servo motor that rotates the antenna. The operating system is Microsoft Windows XP and all the programs are developed in C++ using MS Visual Studio 2008. The user can run both robots simultaneously, calibrate and test the servo mechanism and run several automatic data gathering scenarios. Among all the possible scenarios, the following two are used extensively for the analysis presented in this dissertation:

- Scenario 1: The transmitter is a wireless 802.11g router with an omnidirectional antenna at a height of 1.5 m. The receiver is a robot with an omnidirectional antenna at the height of 27 cm (see Fig. 2.2 (right)).

- Scenario 2: Both the transmitter and receiver are robots with different combinations of directional/omnidirectional TX/RX antennas. The directional antenna is as shown

in Fig. 2.2 (left).
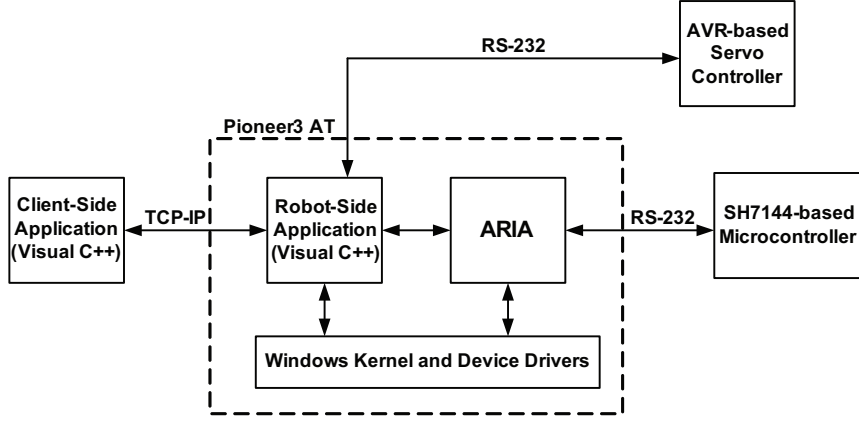
Figure 2.4: The overall software architecture of the robotic platform.

2.2 Characterization of the Spatial Variations of a Wireless Channel [1, 2]

In this section, our goal is to summarize the existing results on the probabilistic characterization of wireless channels, from the wireless communication literature, and to confirm this characterization with our robots. As we have previously mentioned, a communication channel between two robotic platforms can be modeled as a multi-scale dynamical system with three major dynamics: *small-scale fading (multipath fading)*, *shadowing (shadow fading)* and *path loss*. These three dynamics are key to the realistic characterization of the performance of networked robotic systems. We first show an example of these three dynamics through an experiment with our robotic testbed.

Fig. 2.5 shows the blueprint of the basement of our building where we made several measurements along more than 70 routes using our experimental setup. In this chapter, unless we specifically indicate otherwise, the experimental setup consists of a Pioneer P3-AT

robot (receiver) and a fixed wireless router (transmitter), both of which were equipped with omnidirectional antennas. The transmitter is fixed at the height of 1.5 m and the receiver is at a height of 27 cm. The figure also shows a colormap of our measured received signal power for the transmitter at location#1. It should, however, be noted that the framework of this dissertation is also fully applicable for modeling outdoor wireless measurements. We used indoor measurements in this chapter since wireless link quality is typically worse inside a building (due to the higher chance of lacking a line of sight communication).
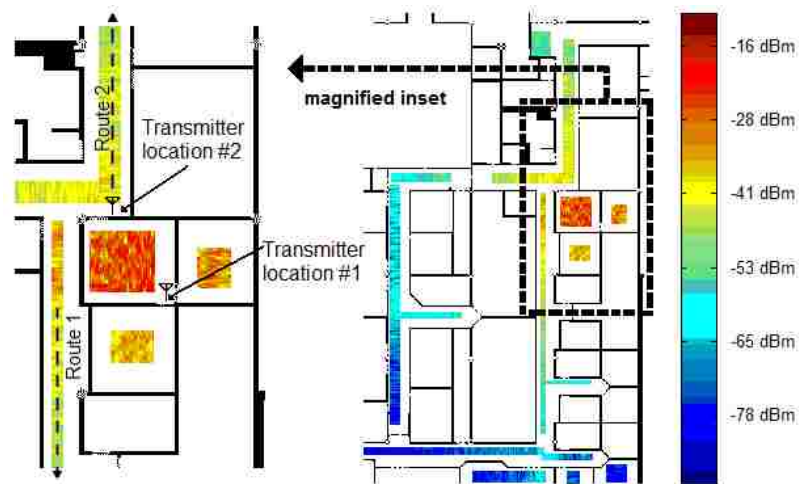
Figure 2.5: (right) Blueprint of the basement of our building, where channel measurements are collected – a colormap of the measured received signal power is superimposed on the map for the transmitter at location#1 (see the pdf file for a color version). (left) A magnified inset of the blueprint.

As an example, Fig. 2.6 shows the received signal power across route 1, as marked in Fig. 2.5, for the transmitter at location#1 and as a function of the distance to the transmitter. The three main dynamics of the received signal power are marked on the figure. As can be seen, the received power can have rapid spatial variations that are referred to as small-scale fading. By spatially averaging the received signal locally and over distances that channel can still be considered stationary, a slower dynamic emerges, which is called shadowing. Finally, by averaging over the variations of shadowing, a distance-dependent

trend is seen, which is referred to as path loss. In this chapter, we provide an understanding and modeling of these underlying dynamics.
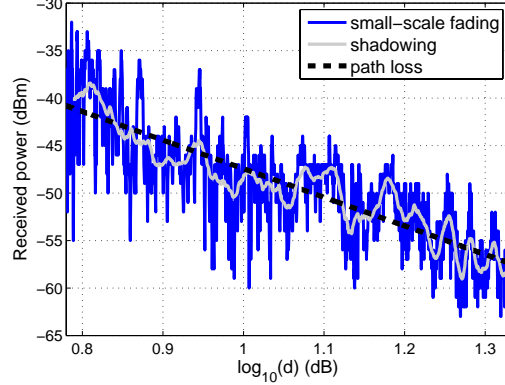
Figure 2.6: Underlying dynamics of the received signal Power across route 1 of Fig. 2.5 and for the transmitter at location#1. The blue curve is the measured received power which exhibits small-scale fading. By averaging locally over small-scale variations, the underlying shadowing variations can be seen (gray). The average of the shadowing variations then follows the distance-dependent path loss curve (dashed line).

2.2.1 Small-Scale Fading (Multipath Fading)

When a wireless transmission occurs, replicas of the transmitted signal will arrive at the receiver due to phenomena such as reflection and scattering. This results in the following baseband equivalent channel at time instant t:

$$ch(t) = \sum_{i=1}^{N(t)} \kappa_i(t) e^{j\varsigma_i(t) - j2\pi f_c \tilde{\tau}_i(t)}, \tag{2.1}$$

where $N(t)$ represents the total number of paths that arrive at the receiving robot at time t, f_c is the carrier frequency, and κ_i, $\tilde{\tau}_i$ and ς_i are the attenuation, delay and Doppler phase shift of the ith path respectively. As can be seen from (2.1), different paths can be added constructively or destructively depending on the phase terms of individual paths.

As a result, with a small movement, the phase terms can change drastically, resulting in the rapid variations of the channel. Such rapid variations are referred to as small-scale fading (multipath fading) and can be seen in Fig. 2.6. The higher the number of reflectors and scatterers in the environment, the more severe small-scale variations could be. Next, we characterize the distribution of $|ch(t)|$ (which easily translates to a distribution for the received Signal to Noise Ratio (SNR) since it is proportional to $|ch(t)|^2$).

In the wireless communications literature, several efforts have been made in order to mathematically characterize the behavior of small-scale fading. As can be seen from Fig. 2.6, the small-scale fading curve is non-stationary over large distances as its average is changing. Therefore, it is common to characterize the behavior of it over small enough distances where channel can be considered stationary. Then, the behavior of the average of the small-scale variations is characterized in order to address channel dynamics over larger distances, as we shall see in the next part. Over small enough distances where channel (or equivalently the received signal power) can be considered stationary, it can be mathematically shown that Rayleigh distribution is a good match for the distribution of $|ch(t)|$ if there is no Line Of Sight (LOS) path while Rician provides a better match if an LOS exists. These distributions also match several empirical data. A more general distribution that was shown to match empirical data is Nakagami distribution [2, 62, 63], which has the following pdf for $z(t) = |ch(t)|$:

$$p(z) = \frac{2m^m z^{2m-1}}{\Gamma(m)\overline{P}_z^m} \exp\left[\frac{-mz^2}{\overline{P}_z}\right], \text{ for } z \geq 0, \tag{2.2}$$

where $m \geq 0.5$ is the fading parameter, $\overline{P}_z = \mathbb{E}[|ch(t)|^2]$ represent the average power of the channel (averaged over small-scale fading) and $\Gamma(.)$ is the Gamma function. If $m = 1$, this distribution becomes Rayleigh: $p^{\text{ray}}(z) = \frac{2z}{\overline{P}_z} \exp\left[\frac{-z^2}{\overline{P}_z}\right]$, for $z \geq 0$, whereas for $m = \frac{(m'+1)^2}{2m'+1}$, it is approximately reduced to a Rician distribution with parameter m':

$$p^{\text{ric}}(z) = \frac{2z(m'+1)}{\overline{P}_z} \exp\left[-m' - \frac{(m'+1)z^2}{\overline{P}_z}\right] I_0\left(2z\sqrt{\frac{m'(m'+1)}{\overline{P}_z}}\right), \tag{2.3}$$

for $z \geq 0$. Similarly, distributions of the power of the channel ($|ch|^2$), the received power

and SNR can be derived by a change of variables. Such distributions can be very helpful in generating realistic communication links for the purpose of mathematical analysis, optimization as well as simulation in robotic networks.

We verified the Nakagami distribution using several measurements in our building. While Rayleigh and Rician distributions are more heavily assumed for the purpose of analysis involving wireless channels, we found that a general Nakagami distribution is a better match for most of our gathered data. As an example, consider the measurement of Fig. 2.6, which is across route 1 of Fig. 2.5 and for the transmitter at location#1. Fig. 2.7 shows the probability density function (pdf) and cumulative distribution function (cdf) of three different sections of the small-scale variations across this route. These parts are chosen such that the data can be considered stationary within each section (since small-scale analysis is only relevant to the small enough and thus stationary parts). It can be seen that the distribution of the gathered data matches power distribution for Nakagami fading with parameters $m = 1.20$ and $m = 1.30$ well. Note that since the distribution of the power of the received signal, which is proportional to $|ch(t)|^2$, is plotted, the figure does not show a Nakagami distribution directly. It shows the power distribution of Nakagami fading, i.e. the distribution of a non-negative variable whose square root has a Nakagami distribution.

While Nakagami distribution shows a good match for the distribution of small-scale fading, mathematical analysis of the performance of a robotic network under such a distribution is generally challenging. Alternatively, a simpler but sub-optimum match is lognormal. In [64], the authors showed that a Gaussian distribution can possibly provide an acceptable match for the distribution of the small-scale variations in dB (albeit with some loss of performance as compared to Nakagami). Fig. 2.8 compares the match of both Nakagami and lognormal to the distribution of small-scale fading for two different stationary sections of the data of Fig. 2.6. As can be seen, Nakagami provides a considerably better match while lognormal can be acceptable depending on the required accuracy.
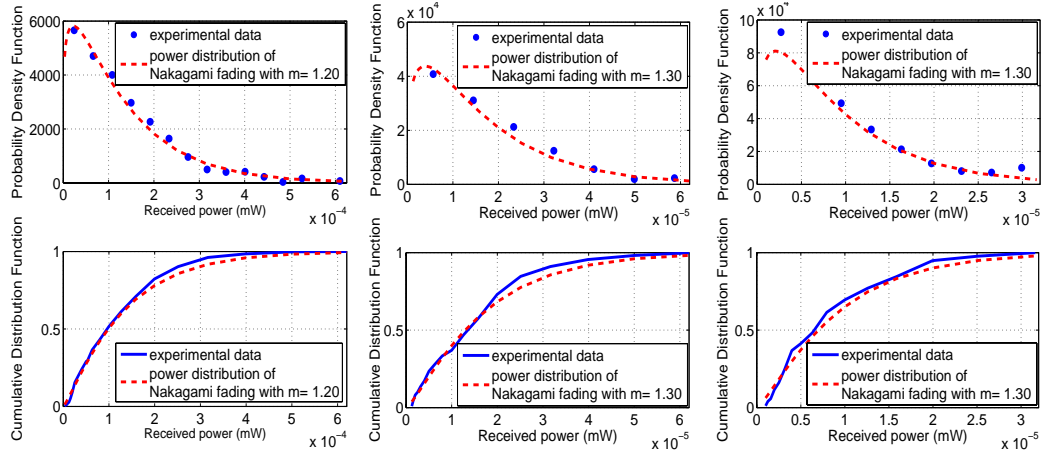
Figure 2.7: The distribution of small-scale fading using three different parts of our gathered measurements. Nakagami distribution shows a very good match – (top figures) pdf and (bottom figures) cdf.
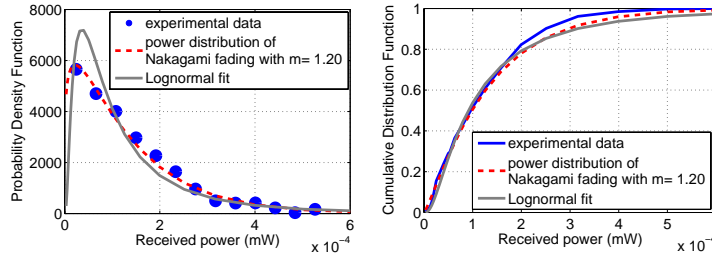
Figure 2.8: Comparison of Nakagami and lognormal for the distribution of small-scale fading – (left) pdf and (right) cdf.

2.2.2 Shadow Fading (Shadowing)

As discussed in the previous part, the received wireless signal is non-stationary over large distances. While small-scale fading characterizes the behavior of the channel over a small distance, it does not suffice for characterizing the channel over larger distances. Small-scale variations are the result of a number of paths arriving at the receiver at approximately the same time but being added constructively or destructively, depending on their phase terms, which results in rapid variations. As Fig. 2.9 shows, once we average over small-scale variations, another dynamic can be observed which changes at a slower rate. Let

$\overline{P}_z = \mathbb{E}\big[|ch(t)|^2\big]$ represent the average power of the channel (averaged over small-scale fading), as defined for (2.2). This signal varies over larger distances and is referred to as shadow fading or shadowing. Shadowing is the result of the transmitted signal being possibly blocked by a number of obstacles before reaching the receiver. Empirical data has shown $\overline{P}_z$ to have a lognormal distribution (mathematical justification also exists by using Central Limit Theorem [2]). Let $\overline{P}_{z,\mathrm{dB}} = 10 \log_{10}(\overline{P}_z)$. We have the following for the distribution of $\overline{P}_{z,\mathrm{dB}}$ [2, 63, 65, 66]:

$$p\big(\overline{P}_{z,\mathrm{dB}}\big) = \frac{1}{\sqrt{2\pi}\sigma_{\mathrm{dB}}}e^{-\frac{(\overline{P}_{z,\mathrm{dB}}-\mu_{\mathrm{dB}})^2}{2\sigma_{\mathrm{dB}}^2}}, \tag{2.4}$$

where $\mu_{\mathrm{dB}} = \beta_{\mathrm{dB}} - 10\eta \log_{10}(d)$ and σ_{dB} is the standard deviation of $\overline{P}_{z,\mathrm{dB}}$. Consider the distance-dependent path loss, $\mu = \beta/d^\eta$, where d represents the distance between the transmitting and receiving robots, η denotes the power fall-off rate and $\beta > 0$ is a constant. Then, it can be seen from (2.4) that $\mu_{\mathrm{dB}} = 10 \log_{10}(\mu) = \beta_{\mathrm{dB}} - 10\eta \log_{10}(d)$ represents the average of shadowing variations. Note that average SNR will also have a lognormal distribution.
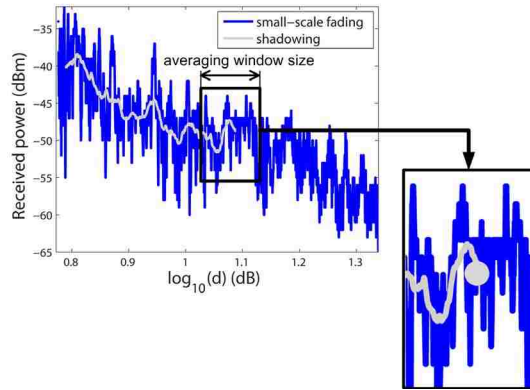
Figure 2.9: Illustration of moving average over small-scale variations in order to obtain shadowing dynamics. An appropriate window length is chosen such that the small-scale variations can be considered stationary over that length. Then, the value of shadowing at the center of this window corresponds to the average of all the data points within the window. Alternatively, the window size can be adaptive.

Fig. 2.10 shows the pdf and cdf of shadow fading for all the collected data in the basement of our building, as shown in Fig. 2.5, and for the transmitter at location#1. In order to access the shadowing variations, the gathered data of each route is averaged locally over small-scale fading, as illustrated in Fig. 2.9. It should be noted that the resulting shadowing variation is non-stationary as its average changes with distance. The distance-dependent path loss component for each route can be easily estimated by finding the best linear fit that relates the log of the received power of the collected data to the log of the distance traveled (see Fig. 2.6 for an example). We then remove the distance-dependent average from shadowing variations before characterizing the distribution of the collected data. As a result, the distribution of the resulting gathered data should match a zero-mean lognormal distribution. It can be seen from Fig. 2.10 that the distribution of the log of the shadowing variations (after removing the distance-dependent average) matches a zero-mean normal distribution very well. The three columns correspond to averaging window sizes of 0.4λ, 1λ and 10λ from left to right, where λ is the wavelength of operation. The standard deviations for these matches are $\sigma_{\text{dB}} = 2.7$, $\sigma_{\text{dB}} = 2.3$ and $\sigma_{\text{dB}} = 1.4$, respectively. As can be seen, as the averaging window size increases, the standard deviation of the best fit becomes smaller. This is as expected since by averaging over larger distances, the resulting signal becomes closer to the underlying overall average (distance-dependent path loss). For this specific data, the best fit corresponds to the averaging window size of 0.4λ, with a Normalized Mean Square Error of 2.89×10^{-4}.

2.2.3 Distance-dependent Path Loss

It can be seen from (2.4) that the distance-dependent path loss, characterized as $\beta_{\text{dB}} - 10\eta \log_{10}(d)$, is the average of the shadowing variations. This completes the relationship between the three underlying dynamics: small-scale fading, shadow fading and path loss. As mentioned earlier, the distance-dependent path loss component can be found by finding the best linear fit that relates the log of the received signal power to the log of the distance
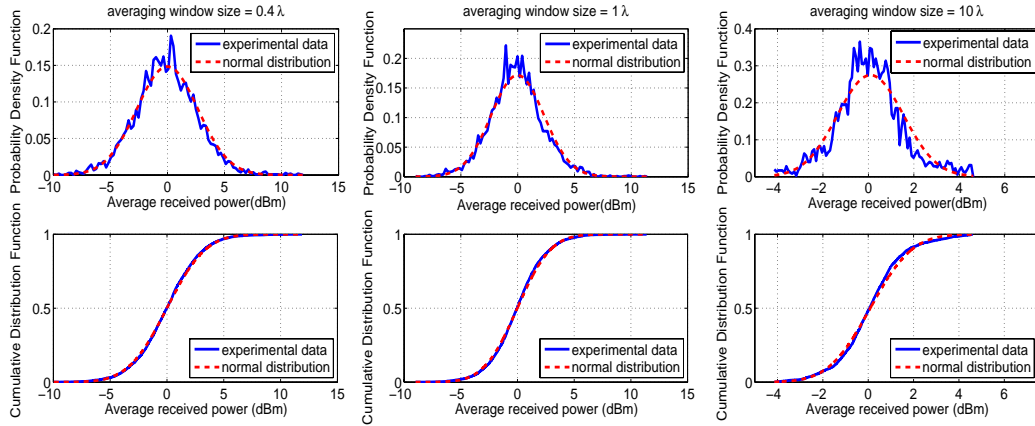
Figure 2.10: (top figures) pdf and (bottom figures) cdf of the log of shadow fading (after removing the distance-dependent path loss) and the normal distribution match for all the data gathered in the basement of our building. The three columns show the impact of the averaging window size on the match: (left column) window size of 0.4λ, (center column) window size of 1.0λ and (right column) window size of 10.0λ, with $\lambda = 0.125$ m denoting the wavelength of the transmitted signal.

traveled. For instance, for the data of Fig. 2.6, path loss component can be characterized as $-17.35 - 30\log_{10}(d)$. It should be noted that the parameters of path loss curve, such as exponent η, vary from route to route. They can even vary within a route if the route is considerably long.

In current networked robotics literature, it is common to use fixed-radius disc models to model wireless channels. It is noteworthy that this over-simplified model only considers path loss. It furthermore assumes the same path loss parameters everywhere in the environment. Therefore, it is only a very crude representation after considerable averaging is done.

2.2.4 Channel Spatial Correlation

Thus far we characterized the distribution of a wireless channel at a single position (or equivalently at a time instant). Another important parameter that characterizes a wireless

channel is its spatial correlation, i.e. how fast the small-scale and shadow fading components are changing spatially. Channel spatial correlation plays a critical role in the cooperative operation of autonomous agents. For instance, it impacts how well we can predict channel spatial variations [67–69] and embed the corresponding communication objectives in a motion-planning function [68, 69].

Spatial correlation of small-scale fading depends on the speed of the robots, frequency of operation and antenna beamwidth/gain, among several other factors. The least correlation is typically observed when there exists a rich scatterer/reflector environment that results in a uniform angle of arrival of the paths. In such cases, the power spectrum of small-scale fading will have a form that is referred to as Jakes spectrum [1] and channel decorrelates on the order of 0.4λ, with λ representing the wavelength (5 cm for 2.4 GHz WLAN transmission). If this is not the case, the spatial correlation function of small-scale fading can be mathematically derived for more general cases [1]. However, a general model that can fit several scenarios does not exist. For most scenarios, small-scale fading decorrelates considerably fast, as compared to the other dynamics.

For shadow fading, there is less mathematical characterization of spatial correlation. Gudmundson [70] characterizes an exponentially-decaying spatial covariance function for the log of the shadow-fading variations, based on outdoor empirical data, which is widely used:

$$
\begin{aligned}
A_{\text{cov}, \overline{P}_{z,\text{dB}}}\left(\|q_1 - q_2\|\right) &= \mathbb{E}\left[\left(\overline{P}_{z,\text{dB},1} - \mu_{\text{dB},1}\right)\left(\overline{P}_{z,\text{dB},2} - \mu_{\text{dB},2}\right)\right] \\
&= \sigma_{\text{dB}}^2 e^{-\frac{\|q_1 - q_2\|}{X_c}}, \quad q_1, q_2 \in \mathbb{R}^2
\end{aligned}
\tag{2.5}
$$

where $\overline{P}_{z,\text{dB},1}$ and $\overline{P}_{z,\text{dB},2}$ are the average power of the channel (averaged over small-scale fading) at positions q_1 and q_2 respectively, $\mu_{\text{dB},1}$ and $\mu_{\text{dB},2}$ are the corresponding path loss components, σ_{dB}^2 is the variance of the log of shadowing as defined in (2.4) and X_c is the decorrelation distance, which is defined as the distance at which the autocovariance

reaches $1/e$ of its maximum value. It has been shown that the decorrelation distance is on the order of the size of the blocking objects or clusters of objects [2].

We used our channel measurements and found the exponential to be a good match for the correlation of shadowing. Figure 2.11 shows the normalized autocovariance function for the data gathered in route 2 of Fig. 2.5 with the transmitter at location #1. It can be seen that the real autocovariance function matches the exponential model considerably well although this is an indoor measurement. We see similar matches across other routes of Fig. 2.5.
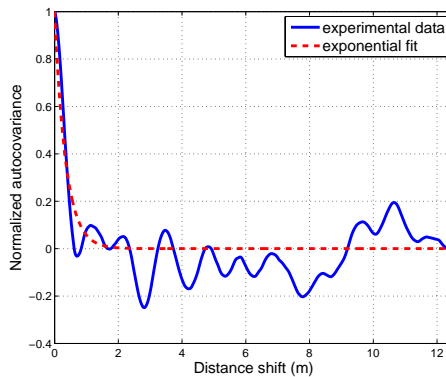
Figure 2.11: Exponential match for the normalized autocovariance of the log of shadowing variations. It can be seen that exponential provides a good match.

2.3 Impact of Antenna Angle

As seen in the previous sections, small-scale fading can result in the severe fluctuations of the received signal power, which can degrade the performance of a robotic network considerably. The main contributor to such fluctuations is the fact that different multipaths can be added constructively or destructively depending on their traveled routes. One possible way to mitigate the impact of multipath fading is to use adaptive directional antennas with a small beamwidth (angle). A smaller beamwidth can limit the number of multipaths that

reach the receiver, which will reduce the chance of the paths being added out of phase. This approach, however, would require alignment and adaption of the transmitting and receiving antennas in order to make sure that they face each other when communicating. As such, it does not work for non-robotic communication systems, such as cellular systems or Wireless Local Area Networks (WLAN), where control of angle is simply not possible. In a robotic network, however, the angle can be adapted. Each robot typically knows the position of another robot in the network, which can be used for on-line adaption and alignment of directional antennas.

As we showed in Section 2.1, we equipped our robots with adaptive directional antennas in order to see their impact on multipath fading. Fig. 2.12 (left), for instance, shows an operation using an adaptive and an omnidirectional antenna whereas in the right figure, both robots are using adaptive antennas. Fig. 2.13 shows the impact of small antenna beamwidth on small-scale fading. The figure shows the received signal power across route 2, marked on Fig. 2.5, and for the transmitting robot at location#2. In the omni-to-omni case, both the transmitter and receiver are omnidirectional. In the omni-to-dir case, the transmitter is omnidirectional while the receiver is directional. Finally, for the dir-to-dir case, both the transmitter and receiver are directional. Our directional antenna has a horizontal and vertical beamwidth of $21°$ and $17°$ respectively.

It can be seen that the dir-to-dir case results in the smallest amount of variations. To measure this, the standard deviations of the received signal power from the distance-dependent path loss are calculated to be 4.53, 2.44 and 1.89 for the omni-to-omni, omni-to-dir and dir-to-dir cases, respectively. Furthermore, it can be seen that the overall signal power increases as we use directional antennas. We saw similar behaviors across other routes in our building. This shows the potential of directional adaptive antennas for networked robotic applications. In the next sections, we extensively use such antennas to limit the impact of multipath fading on our proposed wireless-based obstacle mapping framework.

Figure 2.12: (left) Pioneer robots gathering data at the basement of our building with the transmitter using an omnidirectional antenna and the receiver using a directional one. (right) Pioneer robots using directional antennas for both transmission and reception.

2.4 Summary

In this chapter, we utilized the knowledge available in the wireless communication literature in order to provide a comprehensive overview of the key underlying dynamics of
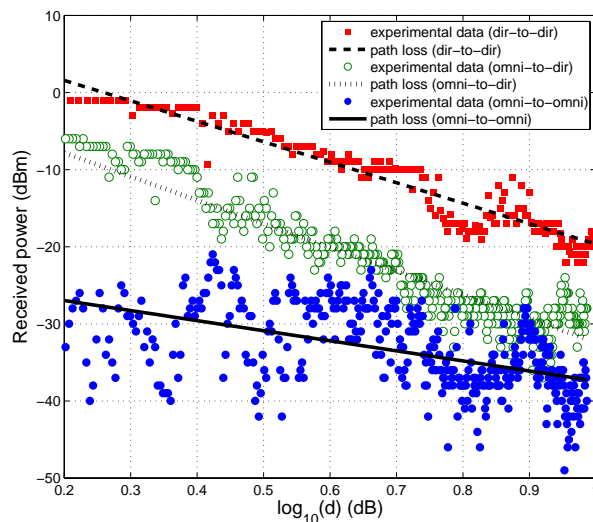
Figure 2.13: Impact of antenna angle in reducing small-scale fading. It can be seen that using an adaptive antenna with a small beamwidth can reduce the amount of multipath fading considerably and also increase the overall received signal power.

wireless channels: small-scale fading, shadowing and the distance-dependent path loss. We confirmed the characteristics of these dynamics experimentally by making an extensive number of channel measurements with our robotic testbed. In order to automate the channel measurement process, we developed a robotic testbed. We furthermore showed how adaptive directional antennas can effectively reduce the effects of multipath fading on the received signal strength. In the next chapter we will introduce our wireless-based obstacle mapping framework, which is based on the fact that the shadowing component of a wireless transmission contains implicit information on the objects located on the path between the transmitter and receiver.

Chapter 3

Wireless-Based Compressive Cooperative Obstacle Mapping

In this chapter, we consider the problem of cooperative mapping of obstacles based on wireless measurements. As previously mentioned, we are interested in mapping with see-through capabilities, i.e. an approach that allows a group of mobile agents to map occluded obstacles without having to sense them directly. This can be particularly useful in several scenarios such as search and rescue, surveillance, and threat detection. It can also save the overall obstacle mapping time and energy in any cooperative robotic scenario by eliminating the need for direct sensing of all the objects.

In general devising strategies for see-through mapping is considerably challenging since traditional sensing and mapping techniques can not be used. In [6–8], Mostofi proposed a framework for mapping of occluded obstacles based on wireless measurements and compressive sampling theory. In this chapter, we summarize that work as it is the line of work we will follow in this thesis. More specifically, we use wireless channel measurements between pairs of robots in order to extract information on the visited objects along the communication path. However, extracting this information from a wireless reception,

without making a prohibitive number of measurements, is very challenging due to several propagation phenomena such as multipath fading discussed in Chapter 2. Thus, we make use of the recent breakthroughs in the area of compressive sampling (CS), which will allow us to properly map obstacles with a small number of wireless measurements as shown in [6–8]. More specifically, we show how the sparse representation of an obstacle map in space, wavelet or spatial variations can be exploited in order to build a map with minimal sensing. We furthermore present three sampling approaches based on coordinated or random wireless measurements [6–8].

We start this chapter by providing a brief overview of CS theory as relevant to our obstacle/object mapping framework.[1] We then explain the details of our wireless-based mapping framework and show how a group of mobile nodes can build a map of obstacles (includes mapping completely blocked objects) by taking very few wireless measurements. We furthermore introduce our strategies for sampling, sparsity domains and reconstruction methods.

3.1 An Overview of Compressive Sampling Theory [3–5]

The new theory of compressive sampling (also known as compressive sensing or CS) is based on the fact that real-world signals typically have a sparse representation in a certain transformed domain. Exploiting sparsity has a rich history in different fields. For instance, it can result in reduced computational complexity (such as in matrix calculations) or better compression techniques (such as in JPEG2000). However, in such approaches, the signal of interest is first fully sampled, after which a transformation is applied and only the coefficients above a certain threshold are saved. This, however, is not efficient as it puts a heavy burden on sampling the entire signal when only a small percentage of the transformed coefficients are needed to represent it. The new theory of compressive

---

[1]The readers are referred to [3–5] and the references therein for a more general study of CS.

sampling, on the other hand, allows us to sense the signal in a compressed manner to begin with. Consider a scenario where we are interested in recovering a vector $x \in \mathbb{R}^N$. For 2D signals, vector x can represent the columns of the matrix of interest stacked up to form a vector. Let $y \in \mathbb{R}^K$ where $K \ll N$ represent the incomplete linear measurement of vector x obtained by the sensors. We will have

$$y = \Phi x, \tag{3.1}$$

where we refer to Φ as the observation matrix. Clearly, solving for x based on the observation set y is an ill-posed problem as the system is severely under-determined ($K \ll N$). However, suppose that x has a sparse representation in another domain, i.e. it can be represented as a linear combination of a small set of vectors:

$$x = \Gamma X, \tag{3.2}$$

where Γ is an invertible matrix and X is S-sparse, i.e. $|\mathrm{supp}(X)| = S \ll N$ where $\mathrm{supp}(X)$ refers to the set of indices of the non-zero elements of X and $|\cdot|$ denotes its cardinality. This means that the number of non-zero elements in X is considerably smaller than N. Then we will have

$$y = \Psi X, \tag{3.3}$$

where $\Psi = \Phi \times \Gamma$. If $S \leq K$ and we knew the positions of the non-zero coefficients of X, we could solve this problem with traditional techniques like least-squares. In general, however, we do not know anything about the structure of X except for the fact that it is sparse (which we can validate by analyzing similar data). The new theory of compressive sensing allows us to solve this problem.

Theorem 1 (see [3] for details and the proof): If $K \geq 2S$ and under specific conditions, the desired X is the solution to the following optimization problem:

$$\min ||X||_0, \text{ such that } y = \Psi X, \tag{3.4}$$

where $||X||_0 = |\text{supp}(X)|$ represents the zero norm of vector X.

Theorem 1 states that we only need $2 \times S$ measurements to recover X and therefore x fully. This theorem, however, requires solving a non-convex combinatorial problem, which is not practical. For over a decade, mathematicians have worked towards developing an almost perfect approximation to the ℓ_0 optimization problem of Theorem 1 [71, 72]. Recently, such efforts resulted in several breakthroughs.

More specifically, consider the following ℓ_1 relaxation of the aforementioned ℓ_0 optimization problem:

$$\min||X||_1, \text{ subject to } y = \Psi X. \tag{3.5}$$

Theorem 2: (see [3], [4]) Assume that X is S-sparse. The ℓ_1 relaxation can exactly recover X from measurement y if matrix Ψ satisfies the Restricted Isometry Condition for $(2S, \sqrt{2} - 1)$, as described below.

Restricted Isometry Condition (RIC) [5]: Matrix Ψ satisfies the RIC with parameters (Z, ϵ) for $\epsilon \in (0, 1)$ if

$$(1 - \epsilon)||c||_2 \leq ||\Psi c||_2 \leq (1 + \epsilon)||c||_2 \tag{3.6}$$

for all Z-sparse vector c. The RIC is mathematically related to the uncertainty principle of harmonic analysis [5]. However, it has a simple intuitive interpretation, i.e. it aims at making every set of Z columns of the matrix Ψ as orthogonal as possible. Other conditions and extensions of Theorem 2 have also been developed [73, 74]. While it is not possible to define all the classes of matrices Ψ that satisfy RIC, it is shown that random partial Fourier matrices [75] as well as random Gaussian [76]- [77] or Bernoulli matrices [78] satisfy RIC (a stronger version) with the probability $1 - O(N^{-M})$ if

$$K \geq B_M S \times \log^{O(1)} N, \tag{3.7}$$

where B_M is a constant, M is an accuracy parameter and O($\cdot$) is Big-O notation [3]. Eq. 3.7 shows that the number of required measurements could be considerably less than N.

While the recovery of sparse signals is important, in practice signals may rarely be sparse. Most signals, however, will be compressible, i.e. most of the energy of the signal is in very few coefficients. In practice, the observation vector y will also be corrupted by noise. The ℓ_1 relaxation and the corresponding required RIC condition can be easily extended to the case of noisy observations with compressible signals [79].

3.1.1 Reconstruction Approaches

Basis Pursuit (BP): Reconstruction Using ℓ_1 Relaxation

The ℓ_1 optimization problem of Eq. 3.5 can be posed as a linear programming problem [80]. The compressive sensing algorithms that reconstruct the signal based on ℓ_1 optimization are typically referred to as "Basis Pursuit" [4]. Reconstruction through ℓ_1 optimization has the strongest known recovery guarantees [5]. However, the computational complexity of such approaches can be high. The ℓ_1 magic toolbox [81] provides several optimization tools for solving the aforementioned ℓ_1 relaxation and its variations. The computational complexity, however, can be high, especially when dealing with real data. SPARSA [82], GPSR [83] and AC [84] are a few examples of the continuing attempts to reduce the computational complexity of the convex relaxation approach. Overall, we found SPARSA to be more computationally efficient yet effective in solving this problem and we will use it in the subsequent chapters.

Matching Pursuit (MP): Reconstruction using Successive Interference Cancellation [5, 85, 86]

While the ℓ_1 relaxation of the previous part can solve the compressive sampling problem with performance guarantees, its computational complexity can be high, as mentioned above. Alternatively, there are greedy approaches that can solve the compressive sampling

problem more efficiently, at the cost of a (possibly slight) loss of performance. Next, we summarize such approaches.

The Restricted Isometry Condition implies that the columns of matrix Ψ should have a certain near-orthogonality property. Let $\Psi = [\Psi_1 \Psi_2 \ldots \Psi_N]$, where Ψ_i represents the ith column of matrix Ψ. We will have $y = \sum_{j=1}^{N} \Psi_j X_j$, where X_j is the jth component of vector X. Consider recovering X_i:

$$\frac{\Psi_i^H y}{\Psi_i^H \Psi_i} = \underbrace{X_i}_{\text{desired term}} + \underbrace{\sum_{j=1, j \neq i}^{N} \frac{\Psi_i^H \Psi_j}{\Psi_i^H \Psi_i} X_j}_{\text{interference}}. \tag{3.8}$$

If the columns of Ψ were orthogonal, then Eq. 3.8 would have resulted in the recovery of X_i. For an under-determined system, however, this will not be the case. Then there are two factors affecting recovery quality based on Eq. 3.8. First, how orthogonal is the ith column to the rest of the columns and second how strong are the other components of X. In other words, it is desirable to first recover the strongest component of X, subtract its effect from y, recover the second strongest component and continue the process. Orthogonal Matching Pursuit (OMP) iteratively multiplies the measurement vector, y, by Ψ^H, recovers the strongest component, subtracts its effect and continue again [85]. Let I_{set} denote the set of indices of the non-zero coefficients of X that is estimated and updated in every iteration. Once the locations of the S nonzero components of X are found, we can solve directly for X by using a least squares solver: $\hat{X} = \underset{X \,:\, \text{supp}\,(X) = I_{\text{set}}}{\operatorname{argmin}} ||y - \Psi X||_2$. A variation of OMP, Regularized Orthogonal Matching Pursuit (ROMP), was later introduced by Needell et al. [5]. The main difference in ROMP as compared to OMP is that in each iterative step, a set of indices (locations of vector X with non-negligible components) are recovered at the same time instead of only one at a time, resulting in a faster recovery [5].

Reconstruction using Total Variation Minimization

In our case, we are interested in reconstructing an obstacle map. Thus, the spatial variations of the map (gradient) are also considerably sparse. In such cases, another related sparsity-based reconstruction approach is to use the sparsity in the gradient [3], [81], [87]. Let $f = [f_{i,j}]$ denote an $m \times m$ matrix that represents the spatial function of interest. Define the following operators: $D_{h,i,j}(f) = \begin{cases} f_{i+1,j} - f_{i,j} & i < m \\ 0 & i = m \end{cases}$ and

$D_{v,i,j}(f) = \begin{cases} f_{i,j+1} - f_{i,j} & j < m \\ 0 & j = m \end{cases}$. Then, the Total Variation (TV) function is defined as follows:

$$\text{TV}(f) = \sum_{ij} \|D_{i,j}(f)\|, \tag{3.9}$$

where $D_{i,j}(f) = [D_{h,i,j}(f) \; D_{v,i,j}(f)]$, and the $\|.\|$ operator can either represent the ℓ_1 norm, corresponding to the anisotropic discretization of TV, or the ℓ_2 norm, corresponding to the isotropic discretization of TV. TV minimization approaches then solve the following problem or a variation of it:

$$\min \text{TV}(f), \text{ subject to } y = \Psi_f \times X, \tag{3.10}$$

where X is a column vector that results from stacking up the columns of matrix f, and y is the observation vector, which is linearly related to X through matrix Ψ_f. In [88], the authors show that solving Eq. 3.10, based on both isotropic and anisotropic TV, results in a similar reconstruction. We have also observed that at the low sampling rates used in this dissertation, anisotropic and isotropic TV yield very similar results, in terms of speed of convergence and reconstruction quality. Consequently, unless we specifically indicate otherwise, the results of this dissertation are based on using anisotropic TV.

The concept of Total Variation was first introduced in [89] for image denoising. TV minimization is a variant of ℓ_1 relaxation that tends to give sharper results on certain types
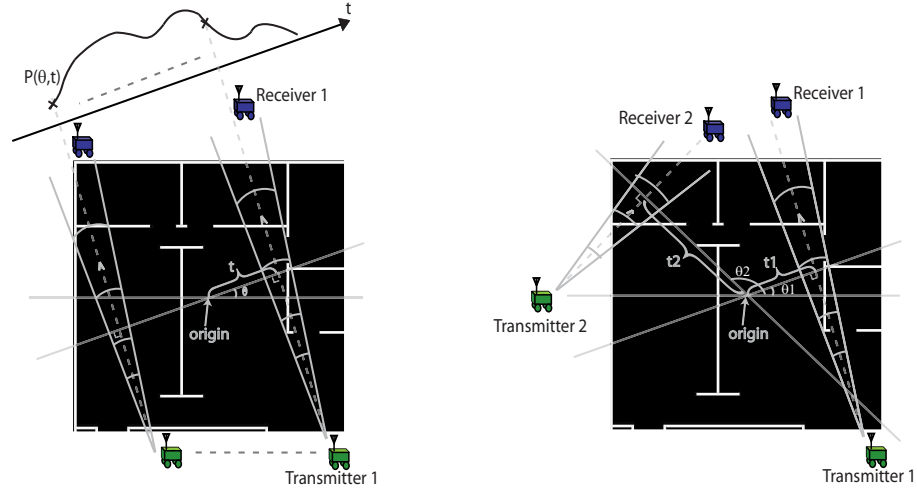
Figure 3.1: An indoor obstacle map with the obstacles marked in white and the illustration of the proposed compressive cooperative mapping using coordinated (left) and random (right) wireless measurements.

of signals [90], and is effective in restoring signals that have staircase characteristics [91]. Thus, it is especially appropriate for the recovery of obstacle maps since the borders, separating different objects, result in sharp discontinuities. Recently, TVAL3 (TV Minimization by Augmented Lagrangian and Alternating Direction Algorithms) is proposed for solving the TV minimization problem efficiently and robustly, which we will use extensively in this dissertation [87].

3.2 Compressive Wireless-based Obstacle Mapping [6–8]

Let an *obstacle map* refer to a 2D (or 3D) map of the environment, where we have zeros at locations where there is no obstacle and non-zero values at obstacle locations. Each non-zero value could be the decay rate of the wireless signal within the object at that location. Let $g(u, v)$ then represent a *binary obstacle map* at position (u, v) for $u, v \in \mathbb{R}$. We consider building a 2D map of the obstacles in this work. For instance, for real 3D structures, we reconstruct a horizontal cut of them, as shown in Section V. It should be

noted that our proposed approach can also be easily extended to 3D maps. Figure 3.1 (both left and right) shows a sample 2D map where a number of vehicles want to map the space before entering it. We will have

$$
g_n(u, v) = \begin{cases} 1 & \text{if } (u, v) \text{ is an obstacle} \\ 0 & \text{else} \end{cases}
$$

(3.11)

Consider communication from Transmitter 1 to Receiver 1, as marked in Fig. 3.1 (left). As we showed in Chapter 2, a wireless transmission can be degraded by several factors [1], namely path loss, shadowing and small-scale fading. Since shadowing is caused by blocking objects, each obstacle along the transmission path leaves its mark on the received signal by attenuating it to a certain degree characterized by its properties. A communication from Transmitter 1 to Receiver 1 in Fig. 3.1 (left), therefore, contains implicit information of the obstacles along the communication path. Consider the dashed ray (line) that corresponds to distance t and angle θ in Fig. 3.1 (left). This line is at distance t from the origin and is perpendicular to the line that is at angle θ with the x-axis. Let $P(\theta, t)$ represent the received signal power in the transmission along the ray that corresponds to distance t and angle θ, as shown in Fig. 3.1 (left). We will have [1, 92, 93],

$$
P(\theta, t) = P_s(\theta, t)\omega(\theta, t),
$$

(3.12)

where

$$
P_s(\theta, t) = \underbrace{\frac{\beta P_T}{\left(d(\theta, t)\right)^\eta}}_{\text{path loss}} \times \underbrace{e^{\sum_i r_{i,\text{obj}}(\theta,t)\alpha_{i,\text{obj}}(\theta,t)}}_{\text{shadowing due to obstacles}}
$$

(3.13)

represents the contribution of distance-dependent path loss and shadowing. For the path loss term, P_T represents the transmitted power, $d(\theta, t)$ is the distance between the transmitter and receiver across that ray, η is the degradation exponent and β is a constant that is a function of system parameters. For the shadowing (or shadow fading) term, $r_{i,\text{obj}}$ is the distance travelled across the ith object along the (θ, t) ray and $\alpha_{i,\text{obj}} < 0$ is the decay rate of the wireless signal within the ith object. Furthermore, the summation is over the objects

across that line. As can be seen, shadowing characterizes wireless signal attenuation as it goes through the obstacles along the transmission path and therefore contains information about the objects along that line. As we saw in Chapter 2, it is also common to characterize the shadowing term probabilistically, using a lognormal distribution [1]. However, the model of Eq. 3.13 is more suitable for our proposed obstacle mapping framework.

$\omega(\theta, t)$ of Eq. 3.12, on the other hand, is a positive random variable with unit average, which models the impact of multipath fading. As discussed in Chapter 2, Nakagami power distribution or its special cases such as Rician power or exponential are common models for the distribution of $\omega(\theta, t)$.[2] We can then model $\ln P(\theta, t)$ as follows

$$\ln P(\theta, t) = \underbrace{\ln P_T}_{\text{transmitted power in dB}} + \underbrace{\beta_{\text{dB}} - \eta \ln d(\theta, t)}_{\text{path loss } (\leq 0)}$$

$$+ \underbrace{\sum_i r_{i,\text{obj}}(\theta, t)\alpha_{i,\text{obj}}(\theta, t)}_{\text{shadowing effect due to blocking objects } (\leq 0)} + \underbrace{\omega_{\text{dB}}(\theta, t)}_{\text{multipath fading}}, \tag{3.14}$$

where $\beta_{\text{dB}} = \ln\beta$ and $\omega_{\text{dB}}(\theta, t) = \ln\omega(\theta, t)$. Then we have

$$h(\theta, t) \triangleq \ln P(\theta, t) - \ln P_T - \left(\beta_{\text{dB}} - \eta \ln d(\theta, t)\right)$$

$$= \underbrace{\sum_i r_{i,\text{obj}}(\theta, t)\alpha_{i,\text{obj}}(\theta, t)}_{\text{shadowing effect}} + \underbrace{\omega_{\text{dB}}(\theta, t)}_{\text{multipath fading}}. \tag{3.15}$$

Path loss and shadowing represent the signal degradation due to the distance travelled and obstacles respectively and $\omega_{\text{dB}}(\theta, t)$ represents the impact of multipath fading. By using an integration over the line that corresponds to θ and t, we can express Eq. 3.15 as follows:

$$h(\theta, t) = \int\int_{\text{line } (\theta, t)} g(u, v)dudv + \omega_{\text{dB}}(\theta, t), \tag{3.16}$$

---

[2] Rician is a possible distribution for $\sqrt{\omega(\theta, t)}$. Thus we use the term "Rician power" to refer to the corresponding distribution for $\omega(\theta, t)$.

where

$$g(u, v) = \begin{cases} \alpha(u, v) & \text{if } g_n(u, v) = 1 \\ 0 & \text{else} \end{cases}, \tag{3.17}$$

with $g_n(u, v)$ representing the binary map of the obstacles (indicated by Eq. 3.11) and $\alpha(u, v)$ denoting the decay rate of the signal inside the object position (u, v). $g(u, v)$ then denotes the true map of the obstacles including wireless decay rate information. As can be seen, $h(\theta, t)$, obtained through wireless measurements, contains implicit information on the obstacle map.[3] This is the foundation of our wireless-based obstacle mapping framework. More specifically, we show different ways of extracting the obstacle map from a small number of wireless measurements, as we shall see in the next section.

3.3 Different possibilities for compressive sampling and reconstruction

In this section, we further present the details of our framework for compressive obstacle mapping, using wireless measurements [6–8]. More specifically, we discuss different possibilities in terms of 1) sampling, 2) sparsity domain and 3) reconstruction technique. A summary of our proposed framework is shown in Fig. 3.2. Note that not all the combinations of the figure result in a proper problem formulation, as we shall discuss in this chapter.

---

[3]In practice, path loss component of Eq. 3.13 can be estimated by using a few Line Of Sight (LOS) transmissions in the same environment as we showed in Chapter 2. Therefore, its impact can be removed and the receiving robot can calculate $h(\theta, t)$.

Elements of Compressive Cooperative Obstacle Mapping
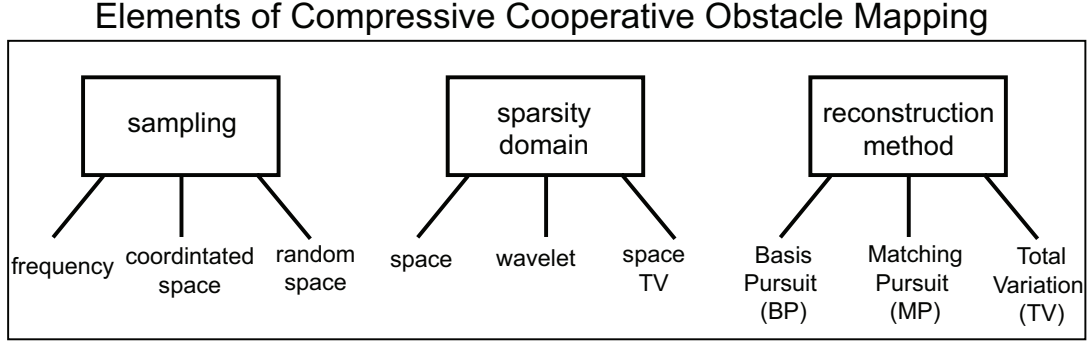
Figure 3.2: Elements of our proposed framework for compressive cooperative obstacle mapping.

3.3.1 Frequency Sampling using Coordinated Wireless Measurements

In this section, we present our obstacle mapping approach that is motivated by computed tomography approaches in medical imaging [94], geology [95], and computer graphics [96]. Consider Fig. 3.1 (left), where pairs of robots are making coordinated wireless measurements. Consider the illustrated line at angle θ that passes through the origin. Outside the structure, two robots can move parallel to this line, in a coordinated fashion, such that a number of wireless channel measurements are formed at different ts. By changing t at a specific θ, a *projection* is formed ($P(\theta, t)$ for a set of ts), i.e. a set of *ray integrals*, as is shown in Fig. 3.1 (left).

Let $G_f(\theta_f, f)$ represent the 2D Fourier transform of g, expressed in the polar coordinates, where θ_f is the angle from the x-axis and f is the distance from the origin. Let $H_t(\theta, f)$ denote the 1D Fourier transform of $h(\theta, t)$ with respect to t: $H_t(\theta, f) = \int h(\theta, t)e^{-j2\pi ft}dt$. The following theorem allows us to sample the frequency response of the 2D obstacle map, using a projection, i.e. based on the coordinated wireless measurements.

Fourier Slice Theorem: Consider the case where there is no multipath fading in Eq. 3.16, i.e. $\omega_{\mathrm{dB}} = 0$. Then $H_t(\theta, f)$, the Fourier transformation of $h(\theta, t)$ with respect to t, is equal to the samples of $G_f(\theta_f, f)$ across angle $\theta_f = \theta$.

Proof: See [94].

By making a number of measurements at different ts for a given θ, the Fourier Slice Theorem allows us to measure the samples of the Fourier transform of the map at angle θ. By changing θ, we can sample the Fourier transform of the obstacle map at different angles. We can then pose the problem in a compressive sampling framework. By measuring the received signal power across a number of rays, the vehicles can indirectly sample the Fourier transformation of the obstacle map. Then the sparsity in the space, space TV or wavelet domain could be used for reconstruction, as explained next.

Reconstruction using the Sparsity in Space or TV

Let V_{G_f} denote the vector representation of the discrete version of G_f (2D Fourier transform of the obstacle map), where the columns are stacked up to form a vector. Let y_f represent the very few samples of G_f acquired using the proposed framework, i.e. wireless channel measurements across a number of coordinated rays and applying the Fourier Slice Theorem.[4] We have,

$$y_f = \Phi_{\mathrm{pt}} V_{G_f} \text{ and } V_{G_f} = \Gamma_f V_{g_s} \Rightarrow y_f = \Psi_{f,s} V_{g_s}$$

$$\text{Fourier Sampling and space or TV sparsity,} \tag{3.18}$$

---

[4]We assume equally-spaced spatial samples across each angle θ.

where Φ_{pt} is a point sampling matrix:

$$\forall i\ 1 \leq i \leq K, \exists j\ 1 \leq j \leq N \text{ such that } \Phi_{\text{pt}}(i,j) = 1 \text{ and}$$
$$\forall i\ 1 \leq i \leq K, \forall\ j \neq j',\ 1 \leq j, j' \leq N,$$
$$\text{if } \Phi_{\text{pt}}(i,j) = 1 \rightarrow \Phi_{\text{pt}}(i,j') = 0, \tag{3.19}$$

with K and N denoting the sizes of y_f and V_{G_f} respectively. Matrix Φ_{pt} represents a matrix with only one 1 in every row. If there are redundant measurements, there may be more than one 1 in every column. Otherwise, there will be at most one 1 in every column. Let g_s represent the discrete obstacle map. Then, V_{g_s} denotes the vector representation of g_s and Γ_f is the Fourier transform matrix, such that when applied to a vector that is formed by stacking the columns of a 2D map, it results in the vector representation of the 2D Fourier transform of the map. Then $\Psi_{f,s} \triangleq \Phi_{\text{pt}} \times \Gamma_f$. Such matrices meet the RIC condition, as shown in [75]. Eq. 3.18 can then be solved by any of the compressive sensing approaches of the previous section (BP or MP). Alternatively, we can consider the sparsity in the Total Variation of V_{g_s}. In the next chapter, we show the underlying tradeoffs between these approaches.

Reconstruction using the Sparsity in the Wavelet Domain

Typically, an obstacle map is also considerably sparse in the wavelet domain, as we shall see later in this section. Let G_w represent the 2D wavelet transform matrix of the discrete obstacle map g_s. We have,

$$y_f = \Phi_{\text{pt}} V_{G_f} \text{ and } V_{G_f} = \Gamma_w V_{G_w} \Rightarrow y_f = \Psi_{f,w} V_{G_w}$$

Fourier sampling and wavelet sparsity, $\tag{3.20}$

where $\Gamma_w = \Gamma_f \times W^{-1}$ with W representing a 2D wavelet matrix such that when applied to a vector that is formed by stacking the columns of a 2D map, it results in the vector representation of the 2D wavelet transform of the map. We have $\Psi_{f,w} \triangleq \Phi_{\text{pt}} \times \Gamma_w$.

Impact of Non-ideal Frequency Sampling

So far, we discussed sampling in the frequency domain using Fourier Slice Theorem. However, this theorem is for the case where we have continuous signals. For the case of a sampled signal (which is the case with our obstacle mapping), the theorem becomes an approximation. The quality of the approximation will then depend on the resolution of the sampled 2D signal and projections. We use the term non-ideal frequency sampling to differentiate this realistic case from the case where the frequency samples are ideally available through Fourier Slice Theorem. Let $g(\theta, t)$, $G_f(\theta, f)$, $h(\theta, t)$ and $H_t(\theta, f)$ be the continuous signals, expressed in polar coordinates, as defined in the previous sections. Let $h_s(\theta, t)$ represent samples of $h(\theta, t)$, acquired through wireless measurements at step intervals of Δ: $h_s(\theta, t) = \sum_n h(\theta, t = n\Delta)\delta(t - n\Delta)$, where $\delta(.)$ is the impulse function. Let $\hat{H}_t(\theta, f)$ represent the Fourier transformation of this sampled signal. We have $\hat{H}_t(\theta, f) = \sum_n h(\theta, t = n\Delta)e^{-j2\pi fn\Delta} = \frac{1}{\Delta}\sum_n H_t(\theta, f - \frac{n}{\Delta})$. Thus, to prevent aliasing, we need $\Delta \leq \frac{1}{2\Omega_{f,\theta}}$, where $\Omega_{f,\theta}$ is the bandwidth of the corresponding continuous function at that angle ($h(\theta, t)$). Similarly, let g_s denote the sampled version of g, using a 2D impulse train. We have $\hat{G}_f(f_i, f_q) = \sum_n \sum_m g(i = n\Delta, q = m\Delta)e^{-j2\pi n\Delta f_i - j2\pi m\Delta f_q} = \frac{1}{\Delta^2}\sum_n \sum_m G_f(f_i - \frac{n}{\Delta}, f_q - \frac{m}{\Delta})$, where $\hat{G}_f(f_i, f_q)$ is the Fourier transformation of g_s, expressed in the Cartesian coordinates and $g(i = n\Delta, q = m\Delta)$ is the original map calculated at the inphase and quadrature components of $n\Delta$ and $m\Delta$ respectively. In order to prevent aliasing, we need $\Delta \leq \frac{1}{2\Omega}$, where Ω represents the bandwidth of the continuous 2D obstacle map.

Wireless measurements will result in measuring $\hat{H}_t(\theta, f)$. Then, that is related to the 2D Fourier of the sampled 2D map through approximation, using the Fourier Slice Theorem: $\hat{H}_t(\theta, f) \approx \hat{G}(\theta, f)$ for samples of $f \in \left[\frac{-1}{2\Delta}, \frac{1}{2\Delta}\right)$. Since the map (and any projection) is space-limited, it can not be bandlimited and as such, there will always be aliasing. Then, the smaller Δ is, the better the quality of this approximation will be. For instance, Eq. 3.18 is written under the assumption that aliasing is negligible. In the next chapter, we show

the impact of non-ideal frequency sampling on mapping quality.

3.3.2   Coordinated Wireless Measurements and Space Sampling

In Section 3.3.1, we used coordinated wireless measurements in order to sample the Fourier transform of the map. Another option is to use the coordinated measurements for direct space sampling. Let vector y_c denote the vector of the gathered samples of $h(\theta, t)$ of Eq. 3.15, using coordinated measurements. We have

$$y_c = \Psi_c X + e \quad \text{coordinated space sampling and TV sparsity,} \tag{3.21}$$

where e models the impact of multipath fading and measurement noise. In each row of Ψ_c, the non-zero elements correspond to the obstacle map pixels that the corresponding ray visited, with each non-zero value indicating the distance travelled in the corresponding pixel.[5] This matrix may not have good RIC properties, which can result in a poor performance if we use sparsity in the space domain (same is the case for the formulation in the wavelet domain). As such, a better way of solving for the obstacle map based on Eq. 3.21 is by using the sparsity in TV.

We know from the compressive sampling literature, especially in the context of ℓ_0 and ℓ_1 optimization problems, that a minimum number of measurements is needed to find the correct solution. For our TV-based coordinated obstacle mapping approach, we can easily see this with a counter example.

Definition 1 - Horizontal Wall Map: We define a *Horizontal Wall Map* as a discretized obstacle map f of size $m \times m$ pixels where a homogeneous horizontal wall of length p pixels, for $2 \leq p < m$, is placed along the kth row of f, with no obstacles anywhere else.

---

[5]We can also approximate the distance travelled in each pixel by the size of a side of a pixel as long as the designated resolution of the map is not too low. This can simplify our modeling and reconstruction, which is what we do in the next chapter.

Lemma 1: Consider the case where $e = 0$. The TV minimization of the spatial variations of the obstacle map based on the coordinated wireless measurements $y_c = \Psi_c \times X + e$, may not result in the correct solution if the number of gathered measurements is too low or the sampling motion angles are not chosen properly.

Proof. Consider the scenario where the Horizontal Wall Map is sampled with coordinated wireless channel measurements along $\theta = 90°$, such that one measurement is taken along each of the m rows of f. Without loss of generality, we assume that the decay rate of the wireless signal inside the obstacle structure is equal to 1, i.e. $\alpha = -1$ in Eq. 3.17 and $f_{i,j} \in \{0, 1\}\ \forall i, j \in \mathbb{Z}, 1 \leq i, j \leq m$. Let X be the vector representation of the discrete obstacle map f. Also let Ψ_{90} denote the corresponding measurement matrix and y_{90} represent the resulting measurement vector. We have the following minimization problem:

$$\min \text{TV}(f), \text{ subject to } y_{90} = \Psi_{90} \times X. \tag{3.22}$$

Let $[y_{90}]_i$ be the ith component of y_{90}. Note that $[y_{90}]_i = 0\ \forall i \neq k$, and $[y_{90}]_k = p$. Thus, the feasible solutions are such that $f_{i,j} = 0\ \forall (i, j), i \neq k$. The TV of the recovered map can then be characterized as follows where $f_{i,j}$ is the value of the pixel at the ith row and j^{th} column of f:

$$\begin{aligned} TV(f) &= 2(f_{k,1} + f_{k,2} + \ldots + f_{k,m}) \\ &\quad + |f_{k,1} - f_{k,2}| + |f_{k,2} - f_{k,3}| + \ldots + |f_{k,m} - f_{k,1}| \\ &= 2p + |f_{k,1} - f_{k,2}| + |f_{k,2} - f_{k,3}| + \ldots + |f_{k,m} - f_{k,1}|. \end{aligned} \tag{3.23}$$

It can be seen that for this case, $TV(f)$ is minimized if and only if $f_{k,1} = f_{k,2} = \ldots = f_{k,m} = \frac{p}{m}$. However, it does not correspond to the original map f where the kth row has $p < m$ pixels equal to 1 and $m - p$ pixels equal to 0. $\square$

3.3.3   Random Wireless Measurements and Space Sampling

Due to the environmental constraints, it may not always be possible to make coordinated measurements. For instance, the path where the robots need to move for making coordinated measurements may be partially blocked. In such cases, the robots can make measurements at different θ and t pairs that are chosen randomly, without trying to maintain a specific pattern. Consider Fig. 3.1 (right), where pairs of robots are making wireless measurements. In this case, we do not assume that the robots are attempting to have a specific pattern, i.e. the θ and t can be chosen randomly. Similar to the coordinated case, we have,

$$y_r = \Psi_r X + e \quad \text{random space sampling and TV sparsity,} \tag{3.24}$$

where vector y_r denotes the gathered samples of $h(\theta, t)$ of Eq. 3.15, using random measurements and Ψ_r is similar to Ψ_c, except that in this case it does not have the coordinated structure. Similar to the previous case, we use the sparsity in the spatial variations (TV) for map reconstruction.

3.4   Summary

In this chapter, we considered a mobile network that is tasked with building a map of obstacles/objects in an environment, including mapping occluded obstacles. We summarized our framework for mapping obstacles including occluded ones, based on wireless measurements. In order to limit the number of needed measurements, we made use of compressive sampling theory. Specifically, we showed how the sparsity of the map in space, wavelet or spatial variations can be exploited in order to build the map with minimal sensing. Furthermore, we presented two sampling strategies based on random or coordinated wireless measurements, the latter of which can be used for direct space sampling or sampling of the Fourier transform of the obstacle map. On the other hand, random wireless measurements are suitable for cases where making coordinated measurements is not possible, such

as scenarios with environmental constraints. We also discussed different reconstruction approaches based on Basis Pursuit, Matching Pursuit and Total Variation minimization. In the next chapter, we will analyze the performance and show the underlying tradeoffs of these sparsity, sampling and reconstruction approaches. We also show the good performance of our framework with both simulations and experiments on our robotic platforms.

Chapter 4

Tradeoffs of Wireless-Based Obstacle Mapping

In this chapter, we study the performance of our wireless-based compressive obstacle mapping framework and show the underlying tradeoffs of different sampling and reconstruction techniques. We start by discussing the case of ideal sampling in the frequency domain, using the Fourier Slice Theorem introduced in the previous chapter, and show the tradeoffs of different reconstruction techniques and sparsity domains. We also compare this sampling strategy with coordinated space and random space sampling. We show that, under certain conditions, the coordinated approach may perform better than the random case. We validate our findings analytically, as well as through simulations. Furthermore, using our experimental robotic platform, we show how to successfully map real obstacles (including completely occluded structures) with see-through capabilities, based on only wireless channel measurements.

We also develop a better understanding of the tradeoffs between the coordinated and random sampling approaches. It is one of our goals to study whether the coordinated approach always outperforms the random one and to what extend. We show that the right

47

approach for comparing these sampling techniques is to look at this problem from the perspective of optimizing the number/choice of the angular motion directions. In particular, random sampling can be considered as an asymptotic case where the total number of given wireless measurements are randomly distributed over an infinite number of angles. We then establish that the total number of available channel measurements should be distributed over a small number of angles, that are bigger than or equal to the number of jump angles of the structure, with a preference given to the angles of jumps. This suggests that the coordinated approach does not necessarily have a better performance than the random case unless the jump angles are chosen. We also validate these findings with our experimental setup that can involve environmental constraints.

4.1 Underlying Tradeoffs of different sampling and reconstruction techniques

In this section, we show the performance of our framework for compressive obstacle mapping in a simulation environment. We see the underlying tradeoffs of different sparsity domains, sampling and reconstruction techniques. As mentioned earlier, an obstacle map is typically considerably sparse in both space and wavelet domains. Furthermore, its spatial variations, measured by its Total Variation (TV), are also considerably sparse. To see this, Fig. 4.1 (left) shows a T-shaped obstacle map. This is a horizontal cut of a real obstacle (see Fig. 4.7, first row) which we will later use to show the performance of our mapping framework in reconstructing real obstacles. Fig. 4.1 (center) shows the 2D wavelet transform of the obstacle map, using Haar wavelets. As can be seen, the map is sparse in both domains, i.e. it can be represented by only a small percentage of the coefficients. More specifically, in the wavelet domain, this map can be represented with only 1.82% of the coefficients as compared to 7.52% in the space domain. While it is hard to mathematically prove the higher sparsity of the wavelet domain for a general obstacle map, our analysis

of several other obstacle maps consistently asserted this hypothesis.

Alternatively, an obstacle map is also considerably sparse in its spatial variations. For instance, consider non-zero changes in both x and y directions as Fig. 4.1 (right) shows for the T-shaped obstacle. Definitely, the number of changes is less than the direct number of non-zero values in the space domain. It is hard, however, to establish any general comparison with the sparsity in the wavelet domain. Our analysis of several maps, however, shows that utilizing the sparsity in spatial variations results in efficient obstacle mapping, as we shall explore in this chapter.

Original obstacle map   Wavelet transform   Spatial Variations
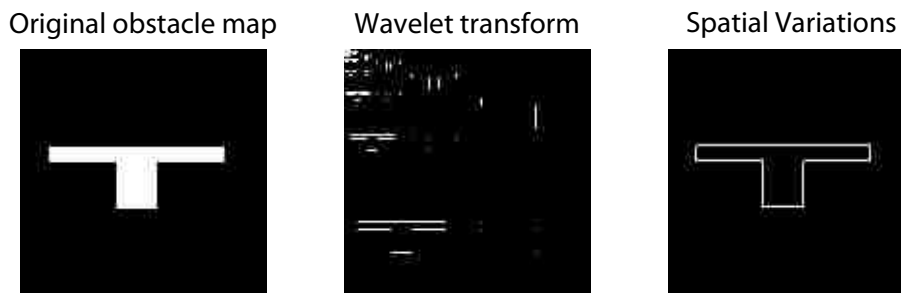
Figure 4.1: A T-shaped obstacle map with the obstacle areas denoted in white, where 100% of the energy is in 7.52% of the space samples (left), its transformed representation in wavelet domain, where 100% of energy is in less than 1.82% of the coefficients (center), and its spatial variations (right).

We start by comparing the case of ideal sampling in the frequency domain, using the Fourier Slice Theorem discussed in the previous chapter. Fig. 4.2 compares the performance of different reconstruction techniques (SPARSA, OMP and ROMP) for the case of frequency sampling when using the sparsity in the space domain. The figure shows the Normalized Mean Square Error (NMSE) of the reconstruction of the T-shape of Fig. 4.1 (left) as a function of the percentage of the measurements collected in the frequency domain. Alternatively, the x-axis could be represented in terms of the number of angle measurements collected.[1] For instance, case of one angle indicates that two robots moved

---

[1]Throughout the dissertation, we may represent the performance as a function of the sampling

parallel to each other for only one given angle (θ of Fig. 3.1) and made wireless measurements at different ts along that angle. As a reference point, the case of 12 angles results in sampling only 9.09% of the Fourier transformation of this map. As such, without the compressive sensing framework, proper reconstruction would require prohibitive number of measurements. As can be seen from the figure, the MP approaches perform considerably worse than the BP approach using SPARSA. This is expected as MP approaches are simpler alternatives (but at the cost of a possible loss of performance) to the original ℓ_1 relaxation method. In between MP approaches, OMP performs worse than ROMP as it is aimed at catching only one non-zero coefficient in every iteration (see Section 3.1.1). In terms of computational complexity, OMP also takes considerably longer than the other two approaches, and as such is not a suitable compressive reconstruction technique for obstacle mapping. While the BP approaches are typically computationally more complex than ROMP, the recently-proposed SPARSA is very efficient with a computational complexity comparable to ROMP. As such, it is a possible efficient technique for compressive reconstruction of an obstacle map.

Next, we consider frequency sampling and reconstruction using the sparsity in the wavelet domain (see Eq. 3.20). We expect to gain a considerable performance improvement as the sparsity in the wavelet domain is noticeably higher than the space domain (see Fig. 4.1). The solid and dashed curves of Fig. 4.3 compare the performance of SPARSA reconstruction based on using the sparsity in the space and wavelet domains, respectively. As can be seen, the performance improves drastically when considering the sparsity in the wavelet domain. This, however, comes at the cost of a non-negligible increase in computational complexity as the corresponding function handles have to deal with wavelet transformation.

The last possibility for the case of frequency sampling is to use the sparsity in the spatial variations for reconstruction. The solid-circle curve of Fig. 4.3 shows the performance

---

rate or the number of utilized angles, depending on the context.
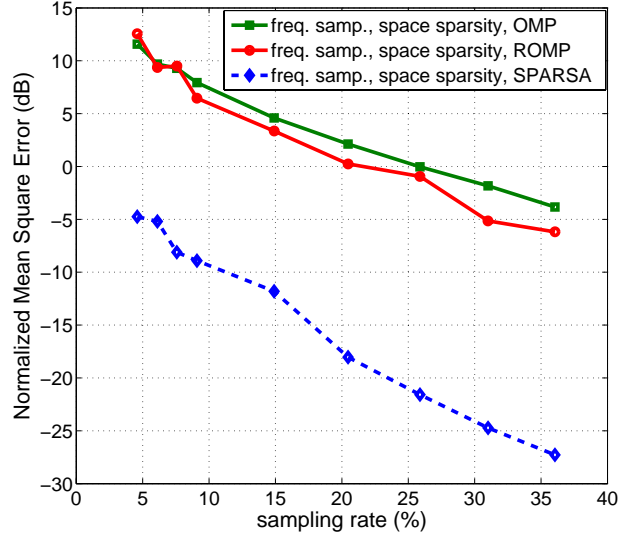
Figure 4.2: Performance of different reconstruction techniques using the proposed Fourier sampling and space sparsity approach. As can be seen SPARSA outperforms the MP approaches considerably. It also has a much less computational complexity as compared to OMP and a comparable complexity to ROMP.

of this case using TVAL solver. As can be seen, this approach results in further performance improvement. Only at considerably high sampling rates, wavelet sparsity approach outperforms this case. Furthermore, with the newly-proposed TVAL, the computational complexity of this approach is considerably less than both SPARSA wavelet and space approaches. We consistently see the aforementioned observations with several other obstacle maps. As such, we find frequency sampling and reconstruction based on spatial variations a viable candidate for compressive obstacle mapping. Using the sparsity in the wavelet domain is also another possibility, specially if the computational complexity is not a concern. Fig. 4.4 compares the reconstructed map for the aforementioned techniques, for the case where only 9.09% of the 2D Fourier function is sampled using Fourier Slice Theorem. As can be seen, the TV approach performs the best. This is followed by wavelet approaches, in particular BP reconstruction with SPARSA. ROMP approach and wavelet

sparsity can also produce a recognizable map. The ROMP-based space approach, on the other hand, results in a pointy map as it attempts to directly capture the non-zero space values.
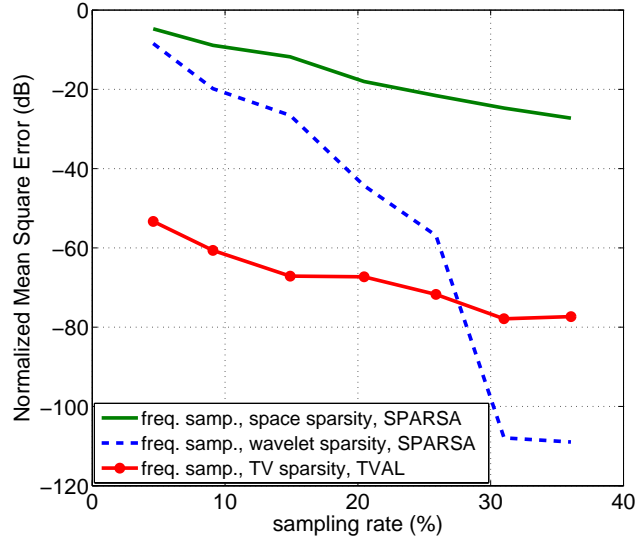
Figure 4.3: Performance of different reconstruction techniques using the proposed Fourier sampling approach. The figure compares the performance of reconstruction based on the sparsity in space, wavelet and total variation. As can be seen, using the sparsity in the spatial variations provides the best performance for most part. This is then followed by using the sparsity in the wavelet domain.

So far, we considered the performance of different reconstruction techniques and sparsity approaches for the case of Fourier sampling. Next, we compare the performance of different sampling techniques, i.e. Fourier, coordinated-space and random-space approaches. The solid and dashed lines of Fig. 4.5 show the performance of coordinated and random space sampling approaches respectively, for the obstacle map of Fig. 4.1 (left). For the coordinated space case, the x-axis can be thought of similar to the frequency sampling case, i.e. coordinated measurements along a number of angles are collected. The total number of coordinated transmissions/receptions along these angles then results in an
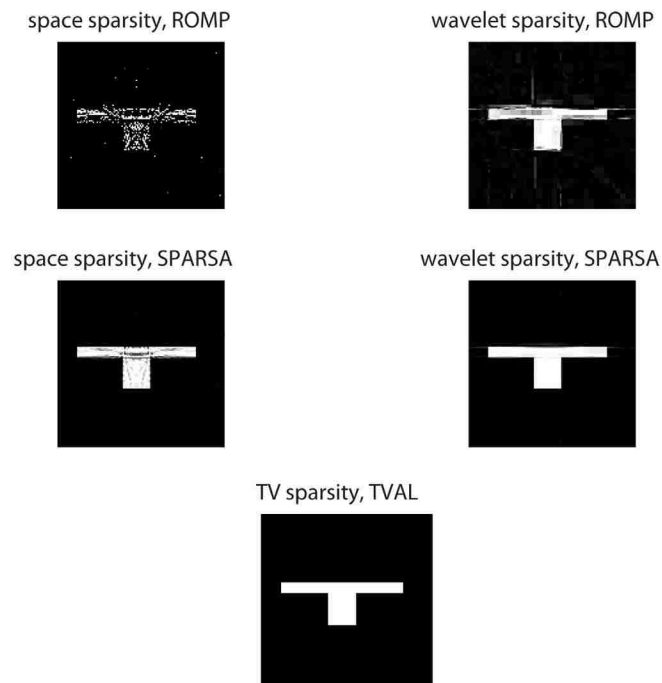
Figure 4.4: The reconstructed obstacle map for the case of frequency sampling when only 9.09% of the Fourier function is sampled. The figure compares the performance of different sparsity/reconstruction techniques.

equivalent percentage of the overall map size in pixels (the quoted sampling rate). Then, for the random space case, the same number of transmissions/receptions is randomly gathered. This number can also be thought of as an equivalent number of frequency samples for comparison. As can be seen, the coordinated approach outperforms the random one considerably for the range of demonstrated sampling rates.

Figure 4.5 also shows the performance with ideal frequency sampling. As can be seen, if the frequency samples can be selected perfectly, the performance is considerably better than the space approaches. In reality, however, this will not be the case as we discussed in Section 3.3.1. In the next section, we show the impact of non-ideal frequency sampling when dealing with real data. As we shall see, the performance of the frequency sampling

case becomes comparable to the coordinated space approach for real data.
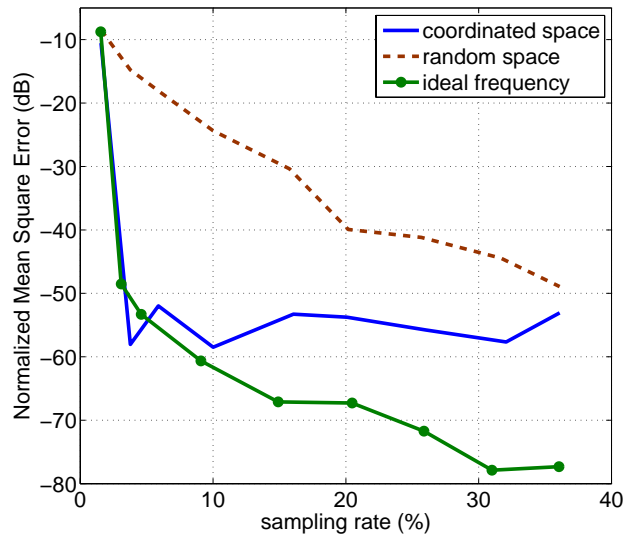
Figure 4.5: A comparison of different proposed sampling techniques. All the reconstructions are with TVAL.

4.2 Cooperative Mapping of Real Obstacles using our Proposed Framework

In the previous section, we showed the performance of our framework in a simulation environment. Next, we show its performance in constructing real obstacles, based on very few wireless measurements. Specifically, we will see that it is indeed possible to map real obstacles and have see-through capabilities using our framework.

In our experiment, we utilize the robotic testbed described in Section 2.1. There are two key enabling factors that contribute to the success of our experimental setup: 1) use of robotic units, which enables automated positioning for collecting wireless measurements

and 2) use of adaptive directional narrow-beam antennas. The latter is crucial in limiting the impact of multipath fading, as we showed in Section 2.3. As can be seen from Eq. 3.15, the proposed mapping framework is based on following the shadowing component. More specifically, the shadowing component carries information on the obstacles, which we have utilized in our framework. As such, multipath fading appears as additional noise and can ruin the mapping quality. Therefore, we use adaptive directional antennas with narrow beamwidth for cooperative obstacle mapping.

We tested our framework outside, where two of our robots made a small number of wireless measurements cooperatively, in order to build a 2D map of a number of obstacles. Fig. 4.6 shows our robots making wireless measurements in order to see through the walls and reconstruct the obstacle. Since our mathematical modeling of a wireless transmission can not embrace all the propagation phenomena, we do not expect a perfect recovery with a very small number of wireless measurements in a real environment. However, as long as the reconstruction is informative, for the cooperative operation of the robots, it could be considerably valuable.

Figure 4.6: (left) Two pioneer 3-AT robots equipped with our servo control mechanism/fixture and an adaptive narrow-beam directional antenna in action, making wireless measurements in order to map the obstacle.

In this section, we show the mapping performance for the reconstruction of the three

obstacles of Fig. 4.7 (left column). Horizontal cuts (2D maps) of these obstacles are shown in the right column of Fig. 4.7. Our robots then aim at reconstructing these structures, based on only wireless channel measurements. In this dissertation, we consider reconstruction in a horizontal plane, i.e. the goal is for the robots to map the horizontal cuts of Fig. 4.7 (right column).

Figure 4.8 shows the mapping quality as a function of the number of utilized angles. In this figure, all the reconstructions are based on coordinated space sampling, i.e. two robots move along a number of angles in parallel, as shown in Fig. 3.1 (left). As we observed from the previous section, coordinated space or frequency sampling and TV sparsity provided the best overall performance and computational complexity for most cases. As such, we used coordinated space sampling, sparsity in the spatial variations (TV) and TVAL for reconstruction in this figure. Later in this chapter, we discuss the underlying tradeoffs with other sampling and reconstruction techniques for real data.

The first row of Fig. 4.8 shows the reconstruction of the T-shape structure for different total number of utilized angles. For each total angle number, uniformly-distributed angles are chosen. For instance, the first case of four total angles means that the robots made coordinated wireless measurements, by moving along 4 pairs of parallel lines. These lines have the angles of 0, 90, 45 and 135 degrees with respect to the x-axis in Fig. 3.1 (left). For comparison with the previous results, where we discussed the performance as a function of the percentage of the sampled points, the case of 4 angles is equivalent to the sampling rate of 3.03%, which is considerably low. As can be seen, by making more coordinated measurements at 6 angles, the performance improves considerably. The improvement is slightly less from 6 to 12 angles, as expected. Adding more measurements at a low sampling rate can typically result in a more drastic improvement. Overall, the reconstructions are noisy as expected, due to several propagation phenomena that our modeling did not include. However, the T-shape structure, with all its details, can be easily seen. The second row shows the mapping performance for the column structure of Fig. 4.7. In this case, if
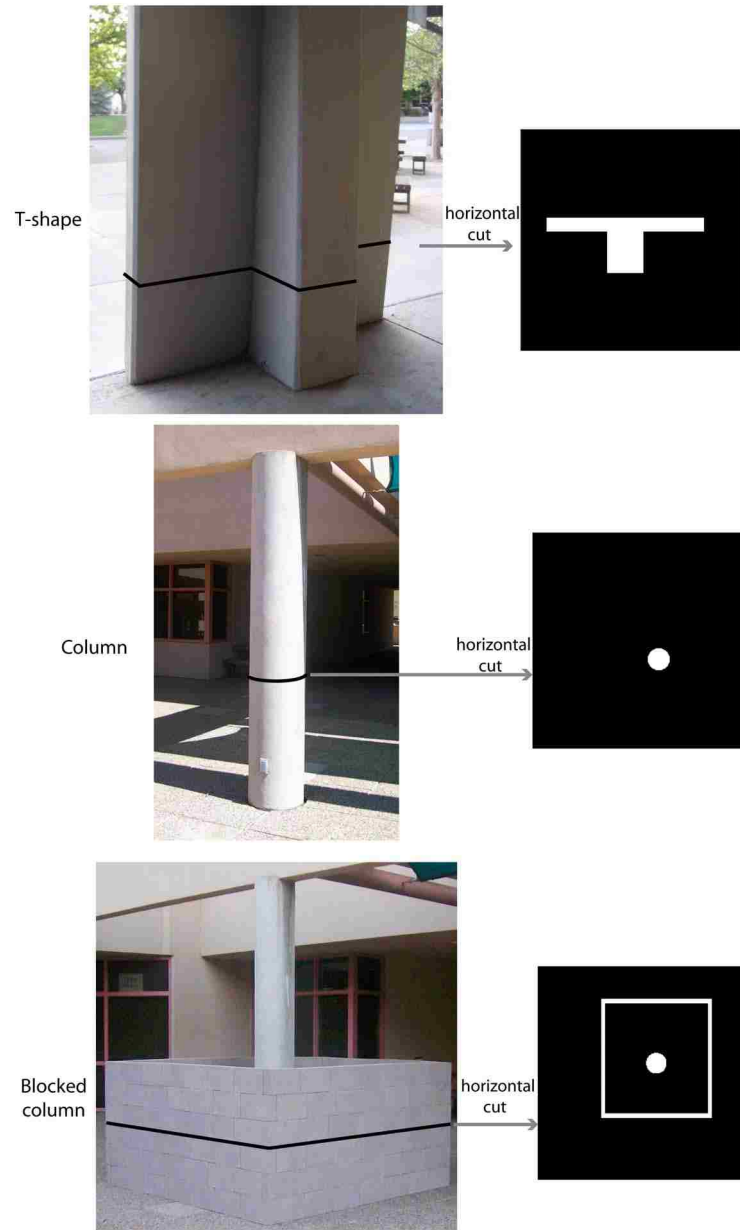
Figure 4.7: The figures show a T-shaped column, a circular column and a blocked column. A horizontal cut of these structures are also shown. Our robots aim to reconstruct the horizontal cut, using our proposed framework.

only two angles are used, this object will not be fully observable, even if the wireless measurements were perfect with no multipath fading/noise. By not fully-observable, we mean that some details of the object will not be detectable even in the perfect sampling scenario. For instance, in the case of 2 angles, this obstacle will be reconstructed as a square in the best case. For the case of real measurements, as can be seen, our proposed framework tries to reconstruct a square for the case of two angles. As we increase the number of angles to 4, then the reconstruction attempts to map the curvatures as well. Similar to the previous case, 4 angles only results in 3.03% sampling rate, which is considerably low. Still, the structure can be correctly identified in the right location, even with such small number of measurements. Depending on the application, the robots may not have time to make several wireless measurements. As such, the capability to identify and map structures with such small sampling rates is very promising.

Finally, the last row shows the performance in mapping the blocked-column structure of Fig. 4.7, for 4 and 8 angles. As can be seen, the reconstruction is noisy with 4 angles while increasing the angles to 8 can considerably improve the mapping quality. It is important to note how the robots can see through the walls and correctly map the column inside for this case. Fig. 4.9 shows the case where a threshold is applied to three of the reconstructed maps of Fig. 4.7, such that any value that is 10dB below the maximum is zeroed. This was done because we noticed that there could be scenarios where reconstructed pixels with very small values get magnified by some printers or monitors with certain gamma settings. A simple thresholding can avoid such cases.

So far, we showed the performance of coordinated space sampling in mapping real obstacles. Next, we consider the performance of the proposed frequency sampling approach. As we saw from Fig. 4.5, if the frequency samples could be chosen perfectly, then the frequency approach outperforms any space approach considerably. However, in reality, there will be a loss of performance due to the fact that Fourier Slice Theorem, while fully holding for continuous functions or proper sampling of bandlimited signals,
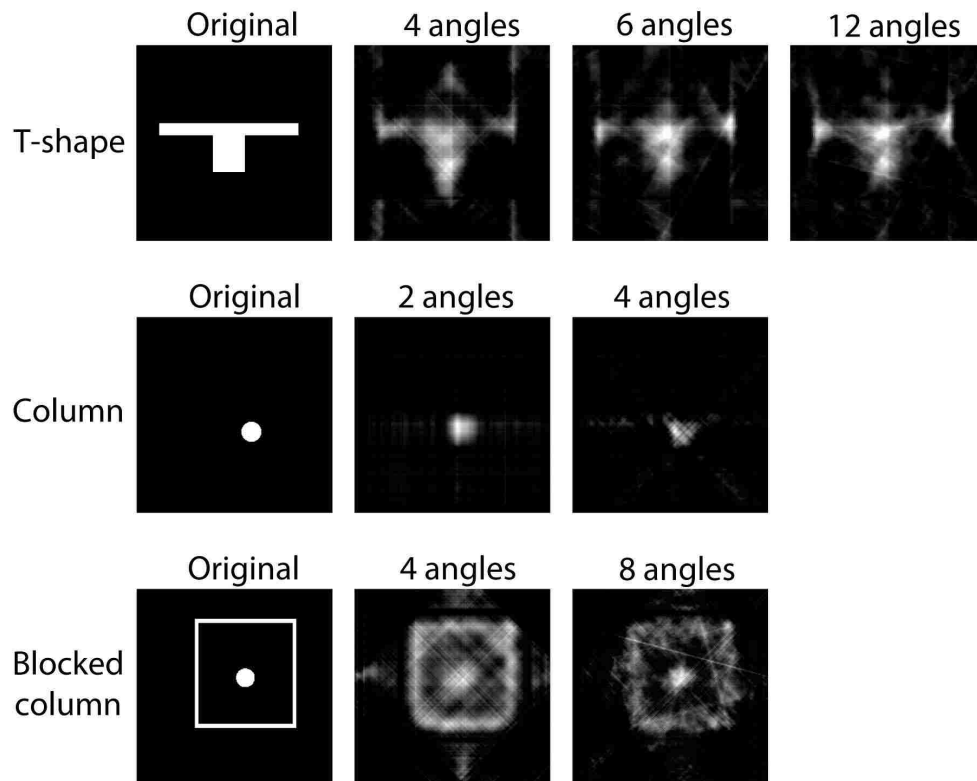
Figure 4.8: Performance of our proposed framework in mapping three real structures. The three structures and their horizontal cuts are shown in Fig. 4.7. As can be seen, the original structures and their details can clearly be seen in our reconstruction although very few wireless measurements were taken.

becomes an approximation when sampling space-limited signals, as discussed in Section 3.3.1. The quality of this approximation depends on the sampling resolution and the frequency response of the original map. Fig. 4.10 shows the mapping quality of the frequency approach for two of the structures of Fig. 4.7. As can be seen, the reconstruction quality is almost the same as that of Fig. 4.8 with coordinated space measurements (we note that it is not exactly the same). In general, we observed that frequency sampling results in a reconstruction very similar to the coordinated space approach.

reconstructed maps with no thresholding

reconstructed maps after thresholding

12 angles

12 angles

4 angles

4 angles

8 angles

8 angles
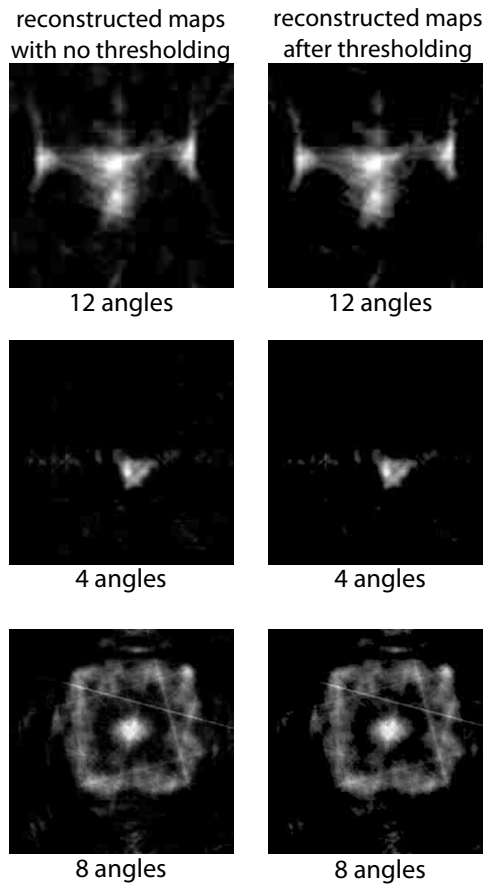
Figure 4.9: Mapping quality after a threshold of 10dB is applied to three of the reconstructed maps of figure 4.8. The threshold is applied such that any value that is 10dB below the maximum is zeroed.

4.3 Coordinated or Random Wireless Measurements?

In previous sections, our results suggested that the coordinated sampling approach may perform better than the random case. It is the goal of this section to thoroughly understand and compare the performance of these two approaches and 1) better understand if and to what extent this is correct and 2) validate our findings through experiments with our experimental robotic setup.

12 angles   8 angles
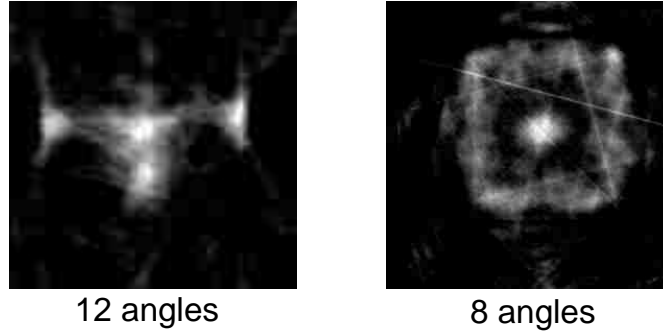
Figure 4.10: Performance of the proposed frequency sampling approach. As can be seen, the reconstruction quality is very similar to that of Fig. 4.8, where coordinated measurements and space sampling were used.

In order to motivate our discussion, we recall the results of Fig. 4.5 for the reconstruction of the T-shape obstacle of Fig. 4.1 (left) using TV minimization. It can be seen that the coordinated space outperforms the random space strategy for the demonstrated sampling rates. However, at extremely low sampling rates (for instance one angle only), the random approach may outperform the coordinated one depending on the sampling angles. To see this more clearly, Fig. 4.11 shows the reconstruction of the aforementioned T-shaped obstacle map, for two different sampling rates. The top row shows the reconstruction for the case where only 0.77% measurements are taken whereas the bottom row shows the reconstruction quality for the case with 4.6% measurements. For the coordinated case of the top left figure, all the measurements are made periodically along one angle ($\theta = 0°$ with the x-axis in this case) while the right figure corresponds to the case of random measurements, i.e. the measurements are randomly distributed over a very high number of angles.[2] It can be seen that for the top row, the random projection can provide a recognizable reconstruction while the coordinated one can not provide any useful information. This makes sense

---

[2]Note that for the random case it is not necessary for each angle to have at least one measurement.

as the coordinated approach makes measurements at only one angle in this case. The random approach, on the other hand, samples the map from possibly different views even at a considerably small sampling rate. If the sampling rate is not extremely small, however, the coordinated approach can outperform the random one considerably. This can be seen from Fig. 4.5 as well as from Fig. 4.11 (bottom row), where the coordinated approach can provide an almost perfect reconstruction with only 4.6 % measurements.

random with 0.77%
measurements

coordinated with 0.77%
measurements

random with 4.60%
measurements

coordinated with 4.60%
measurements
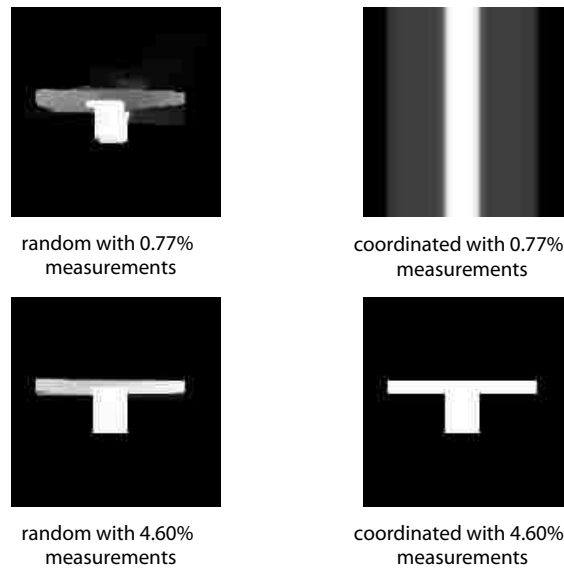
Figure 4.11: Comparison of our mapping framework in the reconstruction of the T-shaped structure of Fig. 4.14 at an extremely small (top row) and small (bottom row) sampling rates in the reconstruction of a T-shaped obstacle, with (left column) random sampling and (right column) coordinated samples.

To see this in mapping a real obstacle, Fig. 4.12 shows the performance of the random and coordinated approaches in mapping the T-shape structure of Fig. 4.7, for the case of one angle for the coordinated sampling (0.77 % sampling rate), as well as for the random case, with the same percentage of gathered measurements chosen from the pool of available coordinated measurements for the case of 12 angles for this structure. As can be seen, for the case of random sampling, the structure is still visible, albeit very noisy, whereas with coordinated measurements, the structure is simply not observable at this low

rate. However, once the structure is sampled from more angles, the coordinated approach can outperform the random one. It is our goal to better understand and compare the performance of random and coordinated wireless measurement approaches in the rest of this chapter.
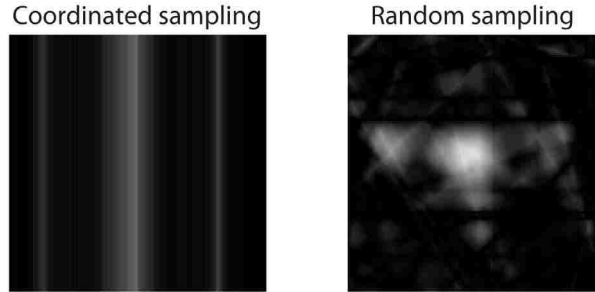
Figure 4.12: Comparison of coordinated and random space sampling approaches in mapping a real obstacle at extremely low sampling rates. Both attempt to build the T-shape structure of Fig. 4.7 with only 0.77% measurements (only one angle for the coordinated case).

Then, we have the following question: given a total number of possible pair-wise wireless measurements, what is the optimum number of angles (optimum in terms of reconstruction quality) to distribute the measurements over? If the optimum number of angles becomes very large, then a more randomized strategy becomes appropriate. Before we can answer this question, however, we need to address the choice of optimum angles.

Optimum strategy for the distribution of the measurements

Consider the case where a pair of robots are making coordinated measurements. For a given angle θ_i, we define a set of ordered ts where measurements are taken, as follows: $T_i = \{t_1(\theta_i), t_2(\theta_i), \ldots, t_{N_i}(\theta_i)\}$, where N_i denotes the total number of gathered measurements at angle θ_i. In this dissertation, we only consider periodic coordinated measure-

ments with respect to t.[3] In other words, we consider the case where the measurements are such that for all i, the distance $\Delta t_j(\theta_i) = t_{j+1}(\theta_i) - t_j(\theta_i)$, for $1 \leq j \leq N_i - 1$, is a constant denoted by Δt. Without loss of generality, we assume that $t_{j+1}(\theta_i) > t_j(\theta_i)$.

By incorporating a random offset in the range $[0, \Delta t)$ to the start position of the first measurement sample along each angle, the case of random sampling can indeed be considered as a special case of coordinated, when the total number of available measurements are randomly distributed among an infinite number of angles.

Consider a structure whose layout corresponds to Fig. 4.13 (left), which has walls laid out along seven different angles. Consider the case where two robots are making coordinated measurements, along a given number of angles in this environment. If the robots can freely choose the angles across which to make wireless measurements, then it is intuitive that the angles that correspond to the directions of the most changes (jumps) should be sampled first. Fig. 4.13, for instance, shows the case where the robots can make a given number of wireless measurements across a given number of angles. The figure shows the impact of choosing some (or all) of the measurement angles to be along the directions of jumps. It can be seen that as the robots make more coordinated measurements along the directions of jumps, the performance improves considerably. While proving this mathematically for a general map is beyond the scope of this dissertation, we provide a simple proof for the case of Horizontal Wall Map defined previously.

Lemma 2: Consider the Horizontal Wall Map of Definition 1 and the case where $e = 0$. Then, sampling along the angle where the majority of the jumps occur ($\theta = 90°$) provides a better reconstruction quality than sampling along $\theta = 0°$. Furthermore, if a binary constraint is enforced in the reconstruction, the samples at $\theta = 90°$ provide more information.

Proof. Similar to the proof of Lemma 1 and without loss of generality, we assume that

---

[3]The observations are also equally applicable to the case of non-periodic coordinated sampling.
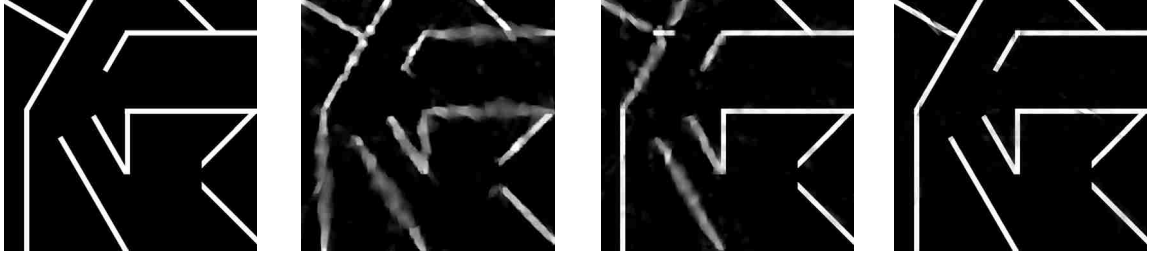
Figure 4.13: (left) An obstacle map with discontinuities occurring at seven angles, (middle-left) reconstruction with no measurements along the jump angles, (middle-right) reconstruction with some measurements along the jump angles and (right) reconstruction with all the measurements along the jump angles.

the decay rate of the wireless signal inside the obstacle structure is equal to 1, i.e. $n = -1$ in Eq. 3.17. Consider the scenario of Lemma 1, where the Horizontal Wall Map is sampled with coordinated wireless channel measurements along $\theta = 90°$, such that one measurement is taken along each of the m rows of f. Let Ψ_{90} and y_{90} be as defined in Lemma 1 for this case. By using the result of Lemma 1, we can calculate the reconstruction error variance when sampling along $\theta = 90°$ as follows:

$$E_{90} = \left(\frac{p}{m} - 1\right)^2 p + \frac{p^2}{m^2}(m - p) = p - \frac{p^2}{m}. \tag{4.1}$$

Next, consider the case where coordinated wireless channel measurements are made along $\theta = 0°$, such that one measurement is taken along each column of f. After a few lines of derivations, we can confirm that we have the following error variance for this case:

$$E_0 = \left(\frac{1}{m} - 1\right)^2 p + \frac{1}{m^2}(mp - p) = p - \frac{p}{m}. \tag{4.2}$$

Clearly, $E_{90} < E_0$.

If we further place a constraint on the TV minimization problem that forces the solution to be binary for each pixel (this would be the case if we knew n a priori), then the

solution may not be unique for the aforementioned two cases. In this case, we can further analyze the amount of information that each of the sampling patterns provides as follows. Consider a binary map f^{bin} with 0.5 probability of having an obstacle at each of the 2^{m^2} pixels. Let $X_{f^{\mathrm{bin}}}$ represent the random vector of the stacked columns of the map and also let $X_{f^{\mathrm{bin}},\theta}$ represent the random vector of the map conditioned on the gathered wireless measurements along angle θ. We can easily confirm that,

$$I(X_{f^{\mathrm{bin}}}, X_{f^{\mathrm{bin}},\theta=90^\circ}) = H(X_{f^{\mathrm{bin}}}) - H(X_{f^{\mathrm{bin}}}|X_{f^{\mathrm{bin}},\theta=90^\circ}) = m^2 - \log_2 \binom{m}{p}, \quad (4.3)$$

where I and H are the mutual information and the entropy respectively. On the other hand, if the samples are such that $\theta = 0^\circ$, then,

$$I(X_{f^{\mathrm{bin}}}, X_{f^{\mathrm{bin}},\theta=0^\circ}) = m^2 - p\log_2(m). \quad (4.4)$$

Since $\binom{m}{p} \leq \frac{m^p}{p!} \leq m^p$, we conclude that $I(X_{f^{\mathrm{bin}}}, X_{f^{\mathrm{bin}},\theta=90^\circ}) \geq I(X_{f^{\mathrm{bin}}}, X_{f^{\mathrm{bin}},\theta=0^\circ})$.

$\square$

This observation is important, especially in mapping indoor environments, since there are typically a small number of jump angles (mainly perpendicular walls). Thus, if the environmental constraints allow it, then the directions with more jumps should be sampled first, for the case of coordinated mapping.

Consider the case where the robots can make a given number of coordinated wireless measurements. We next discuss the optimum number of angles, over which the given measurements should be distributed. In this way, we also compare the random and coordinated cases. In all these reconstructions, first the angles that correspond to the directions

of jumps are chosen. The rest of the angles are then chosen so as to make the angle distribution as uniform as possible, while keeping the previously-chosen angles. Fig. 4.15 shows the mapping performance for the three structures of Fig. 4.14, where a total number of given measurements are distributed along a variable number of angles. As the number of angles increases, the randomness of mapping increases as well. As can be seen, for each structure, there is an optimum number of angles where the coordinated measurements should be distributed. For instance, for the middle and right structures of Fig. 4.14, the optimum number of angles is 4 whereas it is 10 for the left one.[4] The results suggest that the case of random measurements (equivalent to a very high number of angles) does not typically provide the best performance. Furthermore, the optimum number of angles is typically equal to or more than the number of jump angles of the structure. As the structure becomes more complicated (the left structure of Fig. 4.14), the given samples should be distributed along more angles. We have consistently observed these behaviors with other structures.
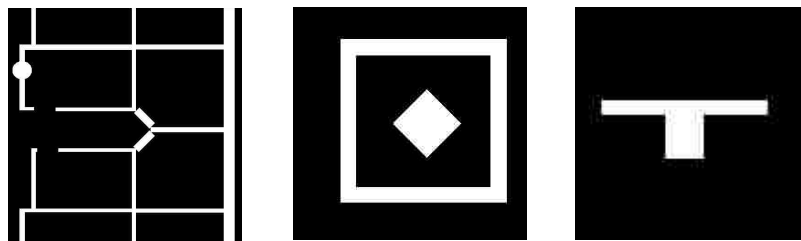
Figure 4.14: Obstacle maps corresponding to (left) a section of the basement of our building, (center) a blocked diamond-shaped column and (right) a T-shaped column.

---

[4]Note that this is independent of the existence of the column in the left figure, since its contribution to the overall structure is small.
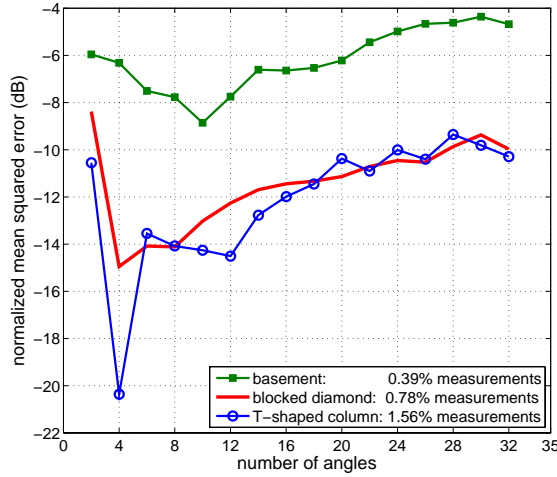
Figure 4.15: Error curves for the reconstruction quality of the obstacle maps of Fig. 4.14, using our coordinated approach. As the number of angles increases, the randomness of mapping increases.

4.3.1 Comparison of the Mapping and See-Through Capabilities of the Coordinated and Random Cases - An Experimental Test

We next show the performance and see-through capabilities of the two approaches in mapping an obstacle structure (that includes an occluded part). Figure 4.16 (left) shows a structure, with its horizontal cut shown in the center figure. For the coordinated case, two robots make coordinated movements and periodic measurements along lines with angles $0°$, $90°$ (marked on the center figure), $45°$ and $135°$. On the other hand, for the random case, the transmitting and receiving robots make wireless measurements at random positions along the dashed lines of Fig. 4.16 (right), while avoiding the cases where both the transmitting and receiving robots are on the same side of the structure. For the random case, we consider two scenarios of *unconstrained* and *constrained* mapping. In the former, the robots are free to position themselves anywhere outside of the structure and make measurements at any position along the dashed lines of Fig. 4.16 (right). In the latter, however, there are environmental constraints (marked in the right figure) that prevent the

robots from moving along certain segments of the lines. In order to have a fair comparison, all the three approaches make the same number of wireless measurements.
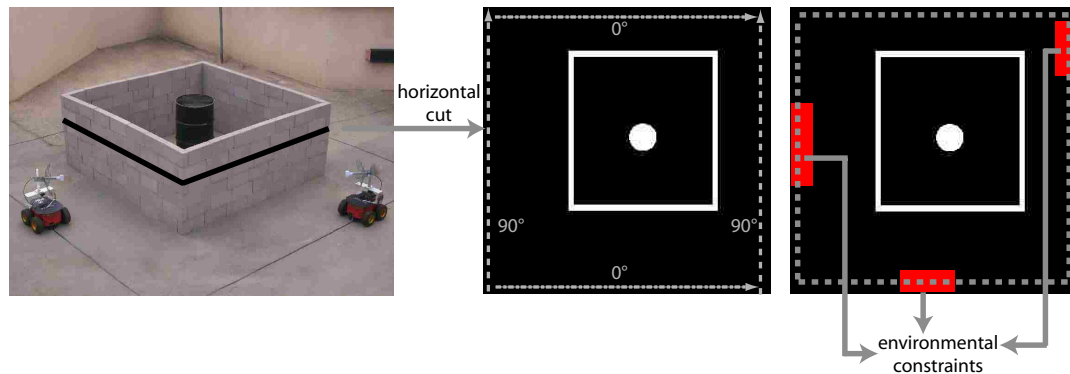
Figure 4.16: (left) An obstacle structure, (center) its horizontal cut and (right) illustration of the physical constraints that limit the positioning of the robots for the constrained case. Our robots aim to reconstruct the structure, based on only making a few wireless transmissions from outside.

Figure 4.17 shows the reconstruction performance for different sampling rates.[5] Each sampling rate denotes the total number of wireless transmissions divided by the size of the 2D map in pixels, as discussed before. The top and bottom rows show the performance for the two cases of 0.76% and 1.83% sampling rates respectively. The three columns show the mapping quality for the cases of coordinated, random unconstrained and random constrained measurements from left to right. As can be seen, the coordinated case, with measurements along four angles, performs considerably better than the random ones, as expected from the previous discussions of the dissertation. Even at a very low sampling rate of 0.76%, the occluded column can be clearly seen, in terms of its position and dimension. Furthermore, the random unconstrained case outperforms the constrained one, as expected. As the number of measurements increases, the reconstruction performance improves for all the cases. As mentioned earlier, we use anisotropic TV minimization approach and TVAL3 solver [87] for all these reconstructions. Fig. 4.18 compares the

---

[5]A threshold is applied to the reconstructed figures such that any value that is 10dB below the maximum is zeroed.

sampling rate needed in order for the random (unconstrained) approach to have a similar reconstruction quality (same MSE) to the coordinated one. As can be seen, 6.98% more samples (3.81 times more) need to be gathered for the random case.
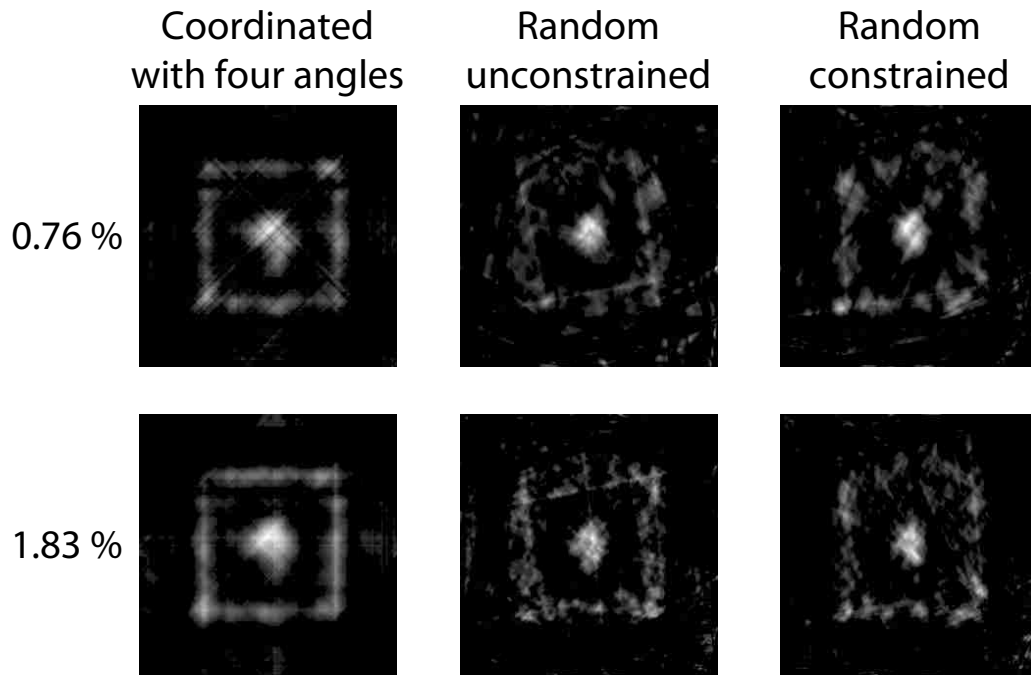
Figure 4.17: Comparison of the mapping and see-through capabilities of the coordinated and random approaches in mapping the structure of Fig. 4.16, using our experimental robotic platform. The top and bottom rows show the performance for the two cases of 0.76% and 1.83% sampling rates respectively. The three columns show the mapping quality for the cases of coordinated (along four angles), random unconstrained and random constrained measurements from left to right. It can be seen that the mapping performance improves considerably from right to left.

Finally, Fig. 4.19 compares the performance of the coordinated and random approaches as a function of the sampling rate. The coordinated measurements are made along $0°$, $90°$, $45°$ and $135°$, whereas the random cases make measurements at positions along the dashed lines of Fig. 4.16 (right), as explained before. As can be seen, the coordinated case outperforms the random ones.

As we discussed earlier, the performance of the coordinated case depends heavily on

Coordinated
with four angles

Random
unconstrained

1.83%　　　　　　　6.98 %
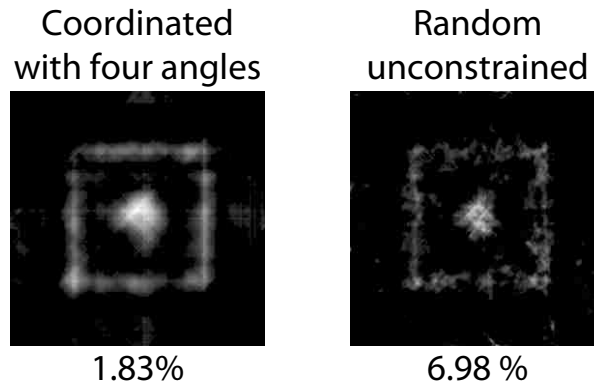
Figure 4.18: Reconstruction of the structure of Fig. 4.16, with (left) coordinated sampling with 1.83% measurements along four angles and (right) random unconstrained sampling with 6.98% measurements. Both reconstructions result in the same Mean Squared Error (MSE).

the choice of the sampling angles. In Fig. 4.17, four angles including the jump ones were sampled, which resulted in the coordinated case performing better than the random one. However, the random case can perform better if the coordinated case is not sampled along the jump angles. The next experiment shows this in mapping the structure of Fig.
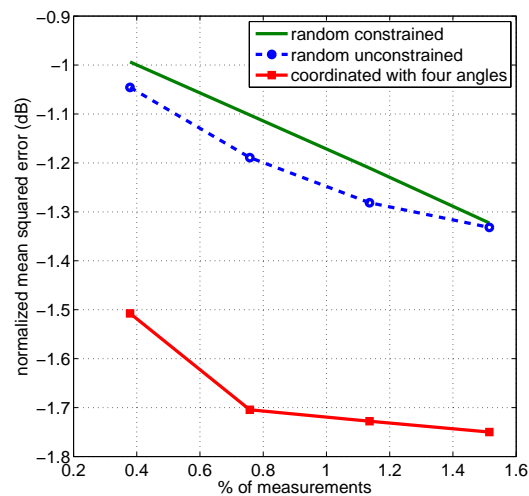
Figure 4.19: Error curves for the reconstruction quality of the obstacle map of Fig. 4.16, using our coordinated approach along four angles and our random approaches. Even at very low sampling rates, the coordinated approach outperforms the random ones.

4.16. For the first set of measurements, the robots make measurements along the jump angles of the outer wall i.e. at $0°$ and $90°$, while for the second set the measurements are made along $45°$ and $135°$. As can be seen in Fig. 4.20 (center), making coordinated measurements along the angles that do not correspond to the jump angles does not result in a useful reconstruction as neither the outer walls nor the occluded obstacle can be correctly mapped. In contrast, if the jump angles are used, the location of the outer walls can be correctly detected, as seen in Fig. 4.20 (left). On the other hand, Fig. 4.20 (right) shows the reconstruction using unconstrained random wireless measurements at the same low sampling rate used for the coordinated cases (0.76%). As can be seen, the reconstruction is considerably better than the case of coordinated along $45°$ and $135°$ in Fig. 4.20 (center).

Coordinated along 0° and 90°   Coordinated along 45° and 135°   Random unconstrained
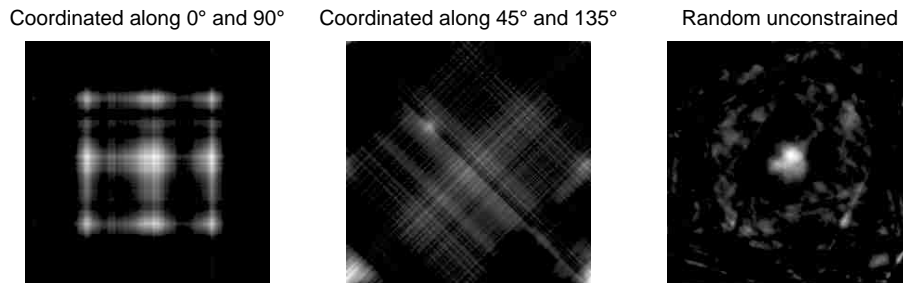
Figure 4.20: Reconstruction of the structure of Fig. 4.16 with 0.76% measurements, with (left) coordinated sampling along the jump angles of the outer walls ($0°$ and $90°$), (center) coordinated sampling along $45°$ and $135°$ and (right) random unconstrained sampling. It can be seen that random sampling can be more informative than coordinated if the structure is not sampled along the jump angles in the coordinated case.

Practical Issues of Wireless-Based Obstacle Mapping

So far, we established that coordinated sampling, along a small number of angles, provides a better reconstruction quality and see-through capability, as compared to the random case. Furthermore, the total number of available channel measurements should be distributed along a small number of angles (bigger than or equal to the number of jump angles), with

a preference given to the angles of jumps. This comparison, however, assumes that there are no environmental, computational or hardware constraints in implementing both approaches. In case of environmental constraints, the random case has a clear advantage. In such cases, partial coordinated measurements can be taken, within the limits of environmental constraints, in addition to random measurements. Both the random and coordinated cases require communication of position information for antenna alignment. Furthermore, they need narrow beamwidth antennas, to limit multipath fading. The random case, however, also requires a constant control and adaptation of the antenna angles to maintain the alignment. Thus, it needs a more advanced hardware. The coordinated case, on the other hand, requires coordinated movement of the robots. Finally, the computational complexity of solving for the map is lower, using the coordinated approach. In summary, we envision that both approaches will be used in practice, depending on the operation environment and the available hardware/software resources.

4.4   Summary

In this chapter, we discussed the underlying tradeoffs of all the possible sampling, sparsity and reconstruction techniques of our obstacle mapping framework. We validated the feasibility and good performance of our framework through simulations as well as through experimental results, where we used our experimental robotic platform to map real obstacles with very few wireless measurements. Our results indicated that the coordinated space sampling or frequency sampling approaches, along with utilizing the sparsity in total variations or wavelet result in a good mapping performance. We also showed a thorough analysis of the performance of the coordinated and random sampling approaches. One of our goals was to understand and compare the performance of both techniques, using both simulation and experimental results. We showed that the right way for comparing the performance of these two sampling patterns is to consider the relationship between the

reconstruction quality and the angular directions where the map is sampled. More specifically, we established that the total number of available channel measurements should be distributed over a small number of angles (bigger than or equal to the number of jump angles of the structure), with a preference given to the angles of jumps. These findings were also validated by mapping an occluded structure using our robotic testbed.

Chapter 5

Integrated Wireless and Grid-Based Obstacle Mapping Framework

So far, we have discussed the underlying tradeoffs of different sampling, sparsity domains and reconstruction techniques of our wireless-based mapping, and showed its performance in reconstructing simple occluded structures. In general, however, obstacle mapping of more complicated structures, solely based on wireless measurements, is extremely challenging due to all the propagation phenomena. Obstacle mapping based on laser scanner data, on the other hand, can typically detect the visible objects with a good accuracy but has no see-through capability. The first goal of this chapter is then to develop an integrated framework that keeps the benefits of both laser-based (or sonar-based) and wireless-based mapping approaches for the reconstruction of occluded structures. Our proposed approach integrates occupancy grid mapping (with known or unknown poses) with compressive sensing (CS) to fuse the laser and wireless channel measurements. More specifically, laser measurements are used to map the parts of the environment that can be sensed directly by the laser scanners of the robots. Based on the partial map built using the laser measurements, we then identify the parts of the environment that can not be mapped efficiently using the laser scanners (e.g., the occluded parts). These parts are then mapped based on

75

our wireless-based mapping framework. Our goal is to enable mapping of occluded structures that can not be mapped with only laser scanner data or a small number of wireless measurements.

In previous chapters, we discussed compressive sensing methods based on ℓ_1 or TV minimization. Recently, the compressive sensing problem has been considered from a Bayesian perspective [97–99]. The goal of Bayesian Compressive Sensing (BCS) is to reconstruct the signal by using an a prior probability distribution that preserves the sparsity [100]. A valuable property of the BCS approach is that it also provides a posterior belief of the signal of interest (an estimated variance). Therefore, it is possible to calculate a measure of uncertainty for the estimation of each cell, which is not possible using traditional CS methods. This property of BCS makes it a potential candidate for probabilistic obstacle mapping as it allows for online adaptive data collection. However, the applicability of BCS approach for see-through mapping of real obstacles, based on wireless measurements, has not been studied before. Therefore, the second goal of this chapter is to develop an integrated grid mapping and BCS approach for mapping of occluded structures. Along this line, we compare the performance of our BCS-based and TV-based integrated approaches, using both simulated and real data, and shed light on the underlying tradeoffs. We then show how the estimated variance of the BCS approach can be utilized to devise adaptive online data collection strategies that guide the robots to make wireless measurements at positions that minimize the uncertainty of the estimated map. In general, the BCS-based mapping approach relies on an initial estimation of the underlying model parameters, which requires some form of a priori measurements and can be prone to error propagation. On the other hand, the estimated variance can be informative for adaptive path planning. Thus, it is worth studying both integrated approaches since a given scenario may favor one over the other.

5.1 System model

Consider the case that a workspace $\mathcal{W} \subset \mathbb{R}^2$ needs to be mapped by a team of M mobile robots.[1] We discretize $\mathcal{W}$ into n small non-overlapping cells. The map of the workspace then refers to a binary vector $x = [x_1, \cdots, x_n]^\mathrm{T}$, where $x_k = 1$ if there is an obstacle in the kth cell in the workspace, and $x_k = 0$ otherwise.

As in previous chapters, each mobile node collects wireless channel measurements by using a wireless communication device (e.g. a IEEE 802.11 WLAN card) along with adaptive directional antennas. Additionally, each robot is also equipped with laser scanners in order to collects laser measurements. A schematic of the mapping scenario considered in this chapter is shown in Fig. 5.1.
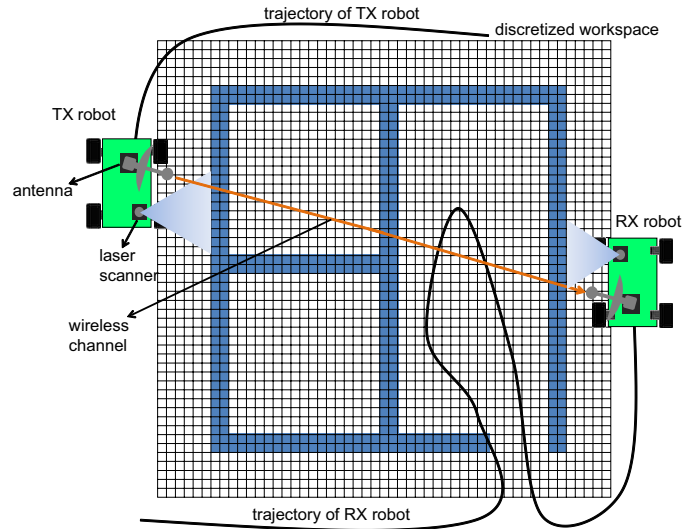
Figure 5.1: Schematic of the proposed integrated mapping scenario using laser and wireless channel measurements.

---

[1]Although for our experiments we use only two mobile robots, the proposed mapping framework of this chapter is applicable to more than two robots. We, therefore, introduce our framework for a team of M robots that cooperate to map the workspace. However, we assume that measurement collection is coordinated (or is done serially) such that different transmissions are not interfering with each other.

Note that the trajectories of the robots when taking the laser measurements may not be the same as their trajectories when taking the wireless channel measurements. In other words, the laser and wireless channel measurements could be available from two different sets of trajectories for the robots.

5.1.1   Laser Measurement Model

Let $z_{i,t}$ denote the laser measurement of the ith mobile robot at time step t.[2] Furthermore, let $q_{i,t} = (\xi_{i,t}, \theta_{i,t})$, for $\xi_{i,t} \in \mathcal{W}$ and $\theta_{i,t} \in (-\pi, \pi]$, represent the position and orientation of the ith mobile robot at time step t when taking the laser measurement. We show by z_t and q_t the stacked vectors of $z_{i,t}$ and $q_{i,t}$ of all the robots at time t, respectively. The stacked vectors of z_t and q_t from time step 1 to time step t are also shown by $z_{1:t}$ and $q_{1:t}$, respectively.

By the laser measurement model, we mean the probabilistic model that relates $z_{i,t}$, $q_{i,t}$ to the map x at any time t. In the robotics literature, this model is generally found empirically and is given in two different ways. The *forward* measurement model for laser scanners gives $p(z_{i,t}|x, q_{i,t})$, i.e., the probability density function (pdf) of $z_{i,t}$ conditioned on x and $q_{i,t}$ [23]. The *reverse* measurement model, on the other hand, gives $p(x_k|z_{i,t}, q_{i,t})$, i.e., the probability of the presence or absence of an obstacle in the kth cell conditioned on $z_{i,t}$ and $q_{i,t}$ [23]. The probability $p(x|z_{i,t}, q_{i,t})$ is then calculated assuming independent x_k: $p(x|z_{i,t}, q_{i,t}) = \prod_{k=1}^{n} p(x_k|z_{i,t}, q_{i,t})$.

In Section 5.2, we summarize how the forward or reverse measurement models can be used to calculate the map posterior probability, i.e., the posterior probability of having an obstacle in each cell, at any time t. The map posterior can then be used to find the cells that have not been scanned efficiently by the onboard laser scanners of the robots

---

[2]For a typical laser scanner (e.g. SICK LMS laser range finders), $z_{i,t}$ is a vector of a fixed number of scalar range measurements.

up to time t. After using all the collected laser measurements of the robots, x_k for such cells are estimated based on the wireless channel measurements in our proposed integrated framework. In this framework, we integrate occupancy grid mapping with Bayesian compressive sensing (BCS) and TV minimization to map the parts of the map that could not be seen by the laser scanners of the robots. These two methods are explained in Sections 5.3 and 5.4, respectively.

5.1.2   Wireless Channel Measurement Model

In addition to the laser measurements, the robots also take a set of wireless channel measurements. These measurements can be collected while the robots take the laser measurements or after taking the laser measurements along a different set of trajectories. Let $y_{i,j,t}$ denote the received signal strength indicator (RSSI) measurement between the ith robot as the transmitter (TX) and the jth one as the receiver (RX) at time t.[3] In Eq. 3.14 we showed an expression for the received signal strength between a wireless transmitter and a receiver. Here we summarize that discussion. As in Chapter 2, we have the following expression for $y_{i,j,t}$, in the dB domain, where we instead use log in base ten [93, 101]:

$$y_{i,j,t} = \underbrace{\beta_{\text{dB},i,j} - \eta_{i,j} \log_{10}\left(\|\xi_{i,t} - \xi_{j,t}\|\right)}_{\text{path loss}} - \underbrace{\psi^{\text{T}}(\xi_{i,t}, \xi_{j,t})\alpha}_{\text{shadowing}} + \underbrace{\omega_{\text{dB},i,j,t}}_{\text{multipath fading}} , \qquad (5.1)$$

where $\beta_{\text{dB},i,j}$ is the path loss constant and $\eta_{i,j}$ is the path loss exponent for the channel between robots i and j. For the shadowing term, the vector α contains the exponential decay coefficients of the wireless signal at each cell, i.e. for each cell k, we have $\alpha_k = 0$ if $x_k = 0$, and $\alpha_k > 0$ otherwise. Note that in Chapters 3 and 4, we used $\alpha(u, v)$ to only denote the decay rate at position (u, v) of the map if there was an obstacle (see Eq. 3.17). We then let V_{g_s} denote the vector representation of the whole discrete map by using α and adding zeros for the places where there is no obstacle. For the sake of simplicity

---

[3]Note that the wireless channel measurements may not be available for every pair (i, j). In other words, only a subset of robots are typically used for channel measurements.

of notation, in this chapter, we simply use α to represent V_{g_s} by assuming that $\alpha = 0$ when there is no obstacle. The kth element of vector $\psi(\xi_{i,t}, \xi_{j,t})$ is the distance that the line segment between $\xi_{i,t}$ and $\xi_{j,t}$ travels across the kth cell multiplied by $\log_{10} e$. Finally, the term corresponding to multipath fading, $\omega_{\text{dB}i,j,t}$, can be modeled as a zero-mean random variable, which is what we will assume henceforth in this chapter.

By subtracting the path loss terms from $y_{i,j,t}$ in (5.1), stacking up all the centered (unbiased) wireless measurements with an arbitrary order, and flipping the sign, we get the following:

$$\tilde{y} = \Psi\alpha + \omega_{\text{dB}}, \tag{5.2}$$

where $\tilde{y}$ is the stacked vector of the centered RSSI values, Ψ is a matrix with its rows given by $\psi^{\text{T}}(\xi_{i,t}, \xi_{j,t})$ in the same order as the elements of $\tilde{y}$, and ω_{dB} is the vector of zero-mean random variables $\omega_{\text{dB},i,j,t}$. In order to use the BCS method for estimating the decay coefficients in Section 5.3, we furthermore assume that the elements of ω_{dB} are uncorrelated Gaussian random variables with the variance of σ_0^2. This implies that the pdf of $\tilde{y}$ conditioned on α, i.e., $p(\tilde{y}|\alpha)$, can be characterized by a multi-variate zero-mean Gaussian pdf with covariance matrix $\sigma_0^2 I_{n_w}$, for I_{n_w} denoting the n_w-dimensional identity matrix and n_w representing the number of total wireless channel measurements. In Chapter 2 we used a stationary chunk of our experimental data to show that distributions such as Nakagami or Rayleigh may better characterize ω_{dB} in non-dB domain [101]. We also saw that a Gaussian distribution (in the dB domain) can also provide a good enough fit [64]. In this chapter we assert this with our channel measurements in Fig. 5.2. In this experiment, we take the RSSI values of the wireless channel measurements between two robots (in the setup of Fig. 5.1) and subtract the ideal measurements (in dB) to obtain the noise component as follows: $\omega_{\text{dB}} = \tilde{y} - \Psi\alpha$. Fig. 5.2 then shows the distribution of this noise, which confirms that a Gaussian distribution can provide a good enough fit. The mean and standard deviation of this best fit are $\hat{\mu} = 0.22$ and $\hat{\sigma}_0 = 10.25$, respectively.

Note that vector α is related to the binary vector x. It is, however, a real vector as op-
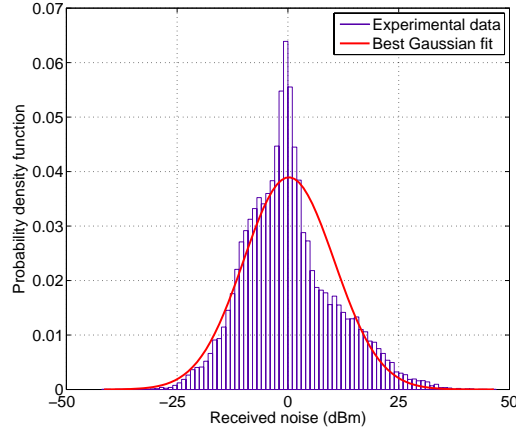
Figure 5.2: The distribution of the noise (ω_{dB}) of Eq. 5.2 from our experimental data and the corresponding best Gaussian fit ($\hat{\mu} = 0.22$ and $\hat{\sigma}_0 = 10.25$).

posed to a binary one, as it shows the decay coefficients of the cells that contain obstacles. In Sections 5.3 and 5.4, we show how to estimate α, using BCS and TV minimization methods. Since the final goal is to estimate the binary vector x, the estimated α is then passed through a hard-limiter, as we further elaborate in Sections 5.3 and 5.4.

5.2   A Brief Overview of Occupancy Grid Mapping using Laser Measurements

In the occupancy grid mapping, the goal is to calculate the map posterior probability, i.e., the probability of having an obstacle (or not) in any cell, conditioned on the laser and pose/odometry measurements. Depending on whether $q_{1:t}$ is available, the map posterior is found using two approaches: *mapping with known poses* and *mapping with unknown poses using SLAM*. Next we briefly explain these two approaches. More detailed explanations can be found in [23, 25, 26].

5.2.1 Mapping with Known Poses

Assume that x_k, for $k = 1, \cdots, n$, are probabilistically independent. Also, assume no prior knowledge on the existence of an obstacle in each cell, i.e., $p(x_k = 1) = p(x_k = 0) = \frac{1}{2}$. In mapping with known poses, the map posterior of interest is $p(x_k|z_{1:t}, q_{1:t})$, which can be written as follows:

$$p(x_k|z_{1:t}, q_{1:t}) = \frac{p(z_t|x_k, q_t)p(x_k|z_{1:t-1}, q_{1:t-1})}{p(z_t|z_{1:t-1}, q_{1:t})},$$

$$p(z_t|x_k, q_t) = \prod_{i=1}^{M} p(z_{i,t}|x_k, q_{i,t}) = \prod_{i=1}^{M} \frac{p(x_k|z_{i,t}, q_{i,t})p(z_{i,t}|q_{i,t})}{p(x_k)}, \tag{5.3}$$

which results in

$$p(x_k|z_{1:t}, q_{1:t}) = \frac{\prod_{i=1}^{M} p(x_k|z_{i,t}, q_{i,t}) \prod_{i=1}^{M} p(z_{i,t}|q_{i,t})}{p(z_t|z_{1:t-1}, q_{1:t}) \prod_{i=1}^{M} p(x_k)} p(x_k|z_{1:t-1}, q_{1:t-1}). \tag{5.4}$$

Let us define $\vartheta_{k,t} \triangleq \log\left(\frac{p(x_k=1|z_{1:t}, q_{1:t})}{p(x_k=0|z_{1:t}, q_{1:t})}\right)$. Using (5.4), we obtain the following recursion:

$$\vartheta_{k,t} = \vartheta_{k,t-1} + \sum_{i=1}^{M} \log\left(\frac{p(x_k = 1|z_{i,t}, q_{i,t})}{p(x_k = 0|z_{i,t}, q_{i,t})}\right) - M \log\left(\frac{p(x_k = 1)}{p(x_k = 0)}\right), \tag{5.5}$$

with the property that $\vartheta_{k,0} = \log\left(\frac{p(x_k=1)}{p(x_k=0)}\right)$. Since $p(x_k = 1) = p(x_k = 0) = \frac{1}{2}$, we have $\log\left(\frac{p(x_k=1)}{p(x_k=0)}\right) = 0$. Therefore,

$$\vartheta_{k,t} = \sum_{\tau=1}^{t} \sum_{i=1}^{M} \log\left(\frac{p(x_k = 1|z_{i,\tau}, q_{i,\tau})}{p(x_k = 0|z_{i,\tau}, q_{i,\tau})}\right), \tag{5.6}$$

where $p(x_k = 1|z_{i,t}, q_{i,t}) = 1 - p(x_k = 0|z_{i,t}, q_{i,t})$ is given by the reverse measurement model for the laser scanner. In case only the forward measurement models are available, (5.6) is calculated by marginalizing the pdf $p(z_{i,t}|x, q_{i,t})$ as follows:

$$\vartheta_{k,t} = \sum_{\tau=1}^{t} \sum_{i=1}^{M} \log\left(\frac{\sum_{x_{-k}} p(z_{i,\tau}|q_{i,\tau}, x_{-k}, x_k = 1)}{\sum_{x_{-k}} p(z_{i,\tau}|q_{i,\tau}, x_{-k}, x_k = 0)}\right), \tag{5.7}$$

where x_{-k} denotes all the elements of x except x_k. Note that the measurement $z_{i,t}$ is only a function of the cells that fall inside the footprint of the ith laser scanner at time t.

Therefore, if a cell x_k falls outside the footprint of the laser scanner at time t, we have $\frac{p(x_k=1|z_{i,t},q_{i,t})}{p(x_k=0|z_{i,t},q_{i,t})} = \frac{\sum_{x_{-k}} p(z_{i,\tau}|q_{i,\tau},x_{-k},x_k=1)}{\sum_{x_{-k}} p(z_{i,\tau}|q_{i,\tau},x_{-k},x_k=0)} = 1$. Finally, the probability of having an obstacle in each cell k is calculated as follows based on $\vartheta_{k,t}$: $p(x_k = 1|z_{1:t}, q_{1:t}) = \frac{1}{e^{-\vartheta_{k,t}+1}}$.

5.2.2   Mapping with Unknown Poses using SLAM

In case the positions and orientation of the mobile robots are not given, the map posterior is found using the SLAM algorithm. Given only the laser measurements and the odometry inputs of the robots, the map posterior of interest is $p(x|z_{1:t}, u_{1:t-1})$ in this case, where $u_{1:t-1}$ is the stacked vector of the odometry inputs of the robots up to time $t-1$. We next briefly summarize how $p(x|z_{1:t}, u_{1:t-1})$ can be estimated using the well-known Rao-Blackwell particle filter (RBPF) for SLAM [25]. The RBPF for SLAM works based on the following factorization:

$$p(x|z_{1:t}, u_{1:t-1}) = \int \underbrace{p(x|z_{1:t}, q_{1:t})}_{\text{mapping with known poses}} \underbrace{p(q_{1:t}|z_{1:t}, u_{1:t-1})}_{\text{localization}} \, \mathrm{d}q_{1:t}. \tag{5.8}$$

This integral is then approximated by the weighted sum of $p(x|z_{1:t}, q_{1:t})$ for a number of potential trajectories of the robots. Based on the Markovian property for the dynamical model of the robots, the pdf $p(q_{1:t}|z_{1:t}, u_{1:t-1})$ can be written as follows:

$$\begin{aligned} p(q_{1:t}|z_{1:t}, u_{1:t-1}) &= p(q_t|q_{1:t-1}, z_{1:t}, u_{t-1})p(q_{1:t-1}|z_{1:t-1}, u_{1:t-2}) \\ &= \frac{p(z_t|q_{1:t}, z_{1:t-1})p(q_t|q_{t-1}, u_{t-1})}{p(z_t|z_{1:t-1}, u_{1:t-1})} p(q_{1:t-1}|z_{1:t-1}, u_{1:t-2}) \end{aligned} \tag{5.9}$$

In RBPF for SLAM, the potential trajectories of the robots are represented by a number of particles. For each particle, an individual map posterior is built sequentially based on the new observations and the pose posterior estimates from the localization part. Assume L particles are used. Let $q_t^{[\ell]}$ denote the potential position and orientation of the robots at time t generated by the ℓth particle. The general form of the RBPF for SLAM is described by the following four steps [35]:

1. A proposal distribution $\pi(q_t|q_{1:t-1}^{[\ell]}, z_{1:t}, u_{t-1})$ is calculated for each particle ℓ. Then $q_t^{[\ell]}$ is found by sampling from this proposal distribution:
$q_t^{[\ell]} \sim \pi(q_t|q_{1:t-1}^{[\ell]}, z_{1:t}, u_{t-1})$.

2. The weights of the particles are calculated as follows: $w_t^{[\ell]} = \frac{p(q_{1:t}^{[\ell]}|z_{1:t}, u_{1:t-1})}{\pi(q_{1:t}^{[\ell]}|z_{1:t}, u_{1:t-1})}$, which results in the following recursion for updating the weights based on (5.9):

$$w_t^{[\ell]} \propto \frac{p(z_t|q_{1:t}^{[\ell]}, z_{1:t-1})p(q_t^{[\ell]}|q_{t-1}^{[\ell]}, u_{t-1})}{\pi(q_t|q_{1:t-1}^{[\ell]}, z_{1:t}, u_{t-1})} w_{t-1}^{[\ell]}, \tag{5.10}$$

for $p(z_t|q_{1:t}^{[\ell]}, z_{1:t-1})$ given as follows:

$$p(z_t|q_{1:t}^{[\ell]}, z_{1:t-1}) = \sum_x p(z_t|x, q_t^{[\ell]})p(x|z_{1:t-1}, q_{1:t-1}^{[\ell]}). \tag{5.11}$$

The updated weights are normalized such that $\sum_{\ell=1}^{L} w_t^{[\ell]} = 1$.

3. The effective number of particles is calculated as $L_{\text{eff},t} = \left[\sum_{\ell=1}^{L} \left(w_t^{[\ell]}\right)^2\right]^{-1}$. If $L_{\text{eff},t} < L_{\text{th}}$, for a given threshold L_{th}, then resampling is performed. This is done by selecting L particles, with replacement, from the set of all the particles up to time t, with probability of selection proportional to $w_t^{[\ell]}$. The selected particles are given uniform weights of $\frac{1}{L}$.

4. For each particle, $p(x|z_{1:t}, q_{1:t}^{[\ell]})$ is found using mapping with known pose methods of the previous section. The final map posterior that is reported is then
$\sum_{i=1}^{L} w_t^{[\ell]} p(x|z_{1:t}, q_{1:t}^{[\ell]})$.

Several proposal distributions have been utilized in the literature. For instance, the landmark-based FastSLAM 1.0 algorithm uses the motion model as the proposal: $\pi(q_t|q_{1:t-1}^{[\ell]}, z_{1:t}, u_{t-1}) = p(q_t|q_{t-1}^{[\ell]}, u_{t-1})$ [32]. The more updated FastSLAM 2.0 algorithm uses $\pi(q_t|q_{1:t-1}^{[\ell]}, z_{1:t}, u_{t-1}) = p(q_t|q_{1:t-1}^{[\ell]}, z_{1:t}, u_{t-1})$ [33]. An improved RBPF algorithm for grids called *gmapping* uses a Gaussian approximation of the observation likelihood as the proposal distribution [35].

Note that similar to mapping with known poses, we define the quantity $\vartheta_{k,t}$ as follows in this case: $\vartheta_{k,t} \triangleq \log\left(\frac{p(x_k=1|z_{1:t},u_{1:t-1})}{p(x_k=0|z_{1:t},u_{1:t-1})}\right)$. This way, $\vartheta_{k,t}$ represents a measure of certainty for any cell k at time t, independent of how the map posterior is calculated.

5.3 Integration of Occupancy Grid Mapping and Bayesian Compressive Sensing (BCS) for Mapping with See-Through Capabilities

In this section, we explain how the BCS approach can be used to map the portion of the workspace that cannot be seen by the onboard laser scanners of the robots. BCS uses the fact that the vector α is sparse in the spatial domain. By applying Baysian filtering methods and using a prior distribution for α that preserves its sparsity, BCS can effectively estimate α in places that cannot be seen by the laser scanners. Next we explain this method in more details.

Consider the partial map found using the laser measurements up to time t (in the middle or at the end of laser mapping operation). Define the following sets of indices: $\mathcal{I}_f \triangleq \big\{1 \leq k \leq n \big| \vartheta_{k,t} \leq -\vartheta_{\text{th}}\big\}, \mathcal{I}_o \triangleq \big\{1 \leq k \leq n \big| \vartheta_{k,t} \geq \vartheta_{\text{th}}\big\}$ and $\mathcal{I}_u \triangleq \big\{1 \leq k \leq n \big| |\vartheta_{k,t}| < \vartheta_{\text{th}}\big\}$, where $\vartheta_{\text{th}} > 0$ denotes a threshold. The sets $\mathcal{I}_f$ and $\mathcal{I}_o$ correspond to the indices of the cells that are estimated to be free-of-obstacle or occupied-by-obstacle, respectively. In other words, we have $\hat{x}_k = 0$ for $k \in \mathcal{I}_f$, and $\hat{x}_k = 1$ for $k \in \mathcal{I}_o$, where $\hat{x}_k$ denotes the estimate of x_k. The cells whose indices are in $\mathcal{I}_u$ are the unknown cells which could not be seen by the laser scanners. Note that laser scanners can typically provide a good mapping quality and, therefore, every cell k that has been seen by the laser scanner of one of the robots belongs to either $\mathcal{I}_f$ or $\mathcal{I}_o$ with a high probability.

Let us rearrange the elements of x as follows: $x = \begin{bmatrix} x_f^{\text{T}} & x_o^{\text{T}} & x_u^{\text{T}} \end{bmatrix}^{\text{T}}$, where x_f, x_o and

x_u denote the stacked vectors of the elements of x whose indices are in $\mathcal{I}_f$, $\mathcal{I}_o$ and $\mathcal{I}_u$, respectively. Also let $\hat{x}_f$, $\hat{x}_o$ and $\hat{x}_u$ denote the vectors with the estimates of the elements of x corresponding to $\mathcal{I}_f$, $\mathcal{I}_o$ and $\mathcal{I}_u$, respectively. Since x_f and x_o are already estimated well using laser scanners, i.e., the all the elements of $\hat{x}_f$ are set to zero and all the elements of $\hat{x}_o$ set to one, the goal is then to estimate x_u using wireless channel measurements. Our strategy consists of two steps:

1. We first estimate the corresponding decay coefficients of the cells in $\mathcal{I}_o$ and $\mathcal{I}_u$ jointly, based on wireless channel measurements and assuming that decay coefficients of the cells in $\mathcal{I}_f$ are zero.

2. Using the estimated decay coefficients of the cells in $\mathcal{I}_u$, we set $\hat{x}_k = 1$, for $k \in \mathcal{I}_u$, if the estimated decay coefficient of the kth cell is larger than a threshold α_{th}, and $\hat{x}_k = 0$ otherwise.

Note that based on only laser measurements, the decay coefficients of the cells in $\mathcal{I}_o$ are not known beforehand. We, therefore, need to estimate their decay coefficients together with the decay coefficients of the cells in $\mathcal{I}_u$ in the first step. However, since these cells are already estimated to be occupied, we do not use their decay coefficients to detect their occupancy in the second step, i.e. we impose the decision generated by the laser scanner for these cells.

Similar to vector x, let us also rearrange the elements of the decay coefficient vector α as $\alpha = \begin{bmatrix} \alpha_f^{\text{T}} & \alpha_o^{\text{T}} & \alpha_u^{\text{T}} \end{bmatrix}^{\text{T}}$. We next show how to estimate $\alpha_{o,u} = \begin{bmatrix} \alpha_o^{\text{T}} & \alpha_u^{\text{T}} \end{bmatrix}^{\text{T}}$ using wireless channel measurements and Bayesian Compressive Sensing (BCS). Consider the stacked vector of the centered RSSI values $\tilde{y}$ in Section 5.1.2. Using the rearranged vector α, we get

$$\tilde{y} = \begin{bmatrix} \Psi_f & \Psi_{o,u} \end{bmatrix} \begin{bmatrix} \alpha_f \\ \alpha_{o,u} \end{bmatrix} + \omega_{\text{dB}} \approx \Psi_{o,u} \alpha_{o,u} + \omega_{\text{dB}}, \tag{5.12}$$

where Ψ_f and $\Psi_{o,u}$ are the parts of Ψ corresponding to the elements of α_f and $\alpha_{o,u}$. Note that we set $\alpha_f \approx 0$ in (5.12). BCS works based on the assumption that $\alpha_{o,u}$ is sparse, which is the case for our obstacle mapping. The vector $\alpha_{o,u}$ is then estimated using a maximum *a posteriori* (MAP) estimator and by using a prior distribution that preserves the sparsity of $\alpha_{o,u}$. Several prior distributions have been proposed in the literature [97–99]. In this chapter, we assume a zero-mean Gaussian prior for $\alpha_{o,u}$. Such a prior is very simple to use and has been shown to achieve a sparse MAP estimate [99]. Conditioned on the channel measurements $\tilde{y}$ and assuming uncorrelated Gaussian ω_{dB} in (5.12), we have

$$p(\alpha_{o,u}|\tilde{y}) = \frac{p(\tilde{y}|\alpha_{o,u})p(\alpha_{o,u})}{\int p(\tilde{y}|\alpha_{o,u})p(\alpha_{o,u})\mathrm{d}\alpha_{o,u}}, \tag{5.13}$$

where $p(\tilde{y}|\alpha_{o,u}) = \frac{1}{(2\pi)^{\frac{n_w}{2}}\sigma_0^{n_w}} \exp\left(-\frac{\|\tilde{y}-\Psi_{o,u}\alpha_{o,u}\|^2}{2\sigma_0^2}\right)$,
$p(\alpha_{o,u}) = \frac{1}{(2\pi)^{\frac{n_{o,u}}{2}}|R_{o,u}|^{\frac{1}{2}}} \exp\left(-\frac{1}{2}\alpha_{o,u}^{\mathrm{T}}R_{o,u}^{-1}\alpha_{o,u}\right)$, $n_{o,u}$ is the number of elements of $\alpha_{o,u}$ and $R_{o,u}$ is its covariance matrix. It can be easily shown that the posterior distribution $p(\alpha_{o,u}|\tilde{y})$ is also Gaussian in this case, i.e.,

$$p(\alpha_{o,u}|\tilde{y}) = \frac{1}{(2\pi)^{\frac{n_{o,u}}{2}}|\Sigma_{o,u}|^{\frac{1}{2}}} \exp\left(-\frac{1}{2}(\alpha_{o,u} - \hat{\alpha}_{o,u})^{\mathrm{T}}\Sigma_{o,u}^{-1}(\alpha_{o,u} - \hat{\alpha}_{o,u})\right), \tag{5.14}$$

where

$$\hat{\alpha}_{o,u} = \frac{1}{\sigma_0^2}\Sigma_{o,u}\Psi_{o,u}^{\mathrm{T}}\tilde{y}, \qquad \Sigma_{o,u} = \left(\frac{1}{\sigma_0^2}\Psi_{o,u}^{\mathrm{T}}\Psi_{o,u} + R_{o,u}^{-1}\right)^{-1}. \tag{5.15}$$

The vector $\hat{\alpha}_{o,u}$ is the MAP estimate of $\alpha_{o,u}$, which can be similarly partitioned as $\hat{\alpha}_{o,u} = \begin{bmatrix}\hat{\alpha}_o^{\mathrm{T}} & \hat{\alpha}_u^{\mathrm{T}}\end{bmatrix}^{\mathrm{T}}$. Here, $\hat{\alpha}_o$ and $\hat{\alpha}_u$ are the estimated decay coefficients of the cells in $\mathcal{I}_o$ and $\mathcal{I}_u$, respectively. Then, for every $k \in \mathcal{I}_u$ we have $\hat{x}_k = 1$ if $\hat{\alpha}_k > \alpha_{\text{th}}$, and $\hat{x}_k = 0$ otherwise.

Note that estimates of σ_0 and $R_{o,u}$ are needed to find the MAP estimate of $\alpha_{o,u}$ in (5.15) Next, we show how to estimate σ_0 and $R_{o,u}$ based on the channel measurements. The estimation of σ_0 is based on Expectation Maximization as is utilized in the BCS literature. As for $R_{o,u}$, an uncorrelated vector is assumed in the BCS literature. In our case of wireless-based obstacle mapping, if the spatial correlation is not considered, the sparsest map may not be the right one. In other words, it is important to consider the spatial

correlation of the map when reconstructing based on sparse wireless measurements. We thus next show how we can have an estimate of the spatial correlation of the map.

5.3.1   Estimation of the Hyperparameters

Without loss of generality, we assume that indices of the elements of $\alpha_{o,u}$ are $1, \cdots, n_{o,u}$. To account for the correlation of the cells, we assume the following form for $R_{o,u}$: $R_{o,u} = \left(\sigma_{o,u}\sigma_{o,u}^{\mathrm{T}}\right) \otimes S_{o,u}$, where $\sigma_{o,u} = [\sigma_1, \cdots, \sigma_{n_{o,u}}]^{\mathrm{T}}$ is the vector of the standard deviations of the elements of $\alpha_{o,u}$ and $S_{o,u}$ is their correlation matrix. In general, finding a good model for the spatial correlation of the map is challenging due to its sparse structure. Based on our experience with several maps, an exponential correlation matrix results in a good reconstruction quality. Thus, we consider the following function in this chapter: $[S_{o,u}]_{k_1,k_2} = \exp\left(-\frac{\|\xi_{\mathrm{cm},k_1} - \xi_{\mathrm{cm},k_2}\|}{\zeta}\right)$, for $1 \leq k_1, k_2 \leq n_{o,u}$. Here, $\xi_{\mathrm{cm},k}$ denotes the position of the center of the mass of the kth cell. The correlation parameter ζ determines how correlated the elements of $\alpha_{o,u}$ are.

Note that due to the high quality of laser measurements, the uncorrelated assumption in laser mapping approach of Section 5.2 does not degrade the map reconstruction performance. However, considering the correlation of the cells is important when mapping the see-through parts of the workspace using the BCS method, as we indicated before.

Based on the proposed model, the hyperparameters to estimate are $\sigma_0, \cdots, \sigma_{n_{o,u}}$ and ζ. Our proposed approach for estimating these hyperparameters is summarized into two steps:

1. Estimate the ζ a priori using a number of sample maps.

2. Estimate $\sigma_0, \cdots, \sigma_{n_{o,u}}$ using expectation maximization (EM) and based on the estimated ζ from the previous step.

Next, we explain these two steps in more details.

Estimation of the Correlation Parameter ζ

In general, coming up with an estimate of the spatial correlation of an obstacle map is a challenging task. In this chapter, we use a set of available obstacle maps to estimate ζ a priori. This estimate is then utilized in our obstacle mapping with real measurements. Consider a set $\mathcal{X}$ which contains a number of binary maps. For every $x \in \mathcal{X}$, define the set $\mathcal{B}(x, d) \triangleq \left\{ (k_1, k_2) \mid \left| \|\xi_{\mathrm{cm},k_1} - \xi_{\mathrm{cm},k_2}\| - d \right| \leq \epsilon \right\}$, for a small ϵ. The estimation of correlation at distance d is then given as follows:

$$\gamma(d) = \frac{\sum_{x \in \mathcal{X}} \sum_{(k_1, k_2) \in \mathcal{B}(x,d)} \neg (x_{k_1} \oplus x_{k_2})}{\sum_{x \in \mathcal{X}} |\mathcal{B}(x, d)|}, \tag{5.16}$$

where $\oplus$ and $\neg$ denote bitwise exclusive-or and negation. The estimate $\hat{\zeta}$ of ζ is then calculated by finding the best exponential fit to $\gamma(d)$ for a given vector of distances $D = [d_1, \cdots, d_M]^{\mathrm{T}}$. It can be easily confirmed that $\hat{\zeta} = -\frac{D^{\mathrm{T}}\Gamma}{D^{\mathrm{T}}D}$, where $\Gamma = \left[\log(\gamma(d_1)), \cdots, \log(\gamma(d_M)) \right]^{\mathrm{T}}$.

Estimation of $\sigma_0, \cdots, \sigma_{n_{o,u}}$ **using Expectation Maximization (EM)**

The EM approach provides an iterative method for estimating $\sigma_0, \cdots, \sigma_{n_{o,u}}$ and has been used in the BCS literature. Let us define $\rho \triangleq (\sigma_0, \cdots, \sigma_{n_{o,u}})$. Also, let $\hat{\rho}^\tau = (\hat{\sigma}_0^\tau, \cdots, \hat{\sigma}_{n_{o,u}}^\tau)$ represent the estimates of ρ at iteration τ. We then have,

$$\text{E step: } \Theta(\rho|\hat{\rho}^\tau) = \mathbb{E}_{\alpha_{o,u}|\tilde{y},\hat{\rho}^\tau} \left\{ \log \left[p(\tilde{y}|\alpha_{o,u}) p(\alpha_{o,u}) \right] \right\},$$
$$\text{M step: } \hat{\rho}^{\tau+1} = \operatorname{argmax}_\rho \Theta(\rho|\hat{\rho}^\tau). \tag{5.17}$$

Let $\hat{\alpha}_{o,u}^{\tau}$ and $\hat{\Sigma}_{o,u}^{\tau}$ denote $\hat{\alpha}_{o,u}$ and $\Sigma_{o,u}$ in (5.15) when $\sigma_0, \cdots, \sigma_{n_{o,u}}$ are replaced with $\hat{\sigma}_0^{\tau}, \cdots, \hat{\sigma}_{n_{o,u}}^{\tau}$. After some straightforward calculations, we then have the following:[4]

$$
\begin{aligned}
\Theta(\rho|\hat{\rho}^{\tau}) = &-n_w \log(\sigma_0) - \frac{1}{2}\log\left(|R_{o,u}|\right) - \frac{1}{2\sigma_0^2}\|\tilde{y} - \Psi_{o,u}\hat{\alpha}_{o,u}^{\tau}\|^2 \\
&- \frac{1}{2}(\hat{\alpha}_{o,u}^{\tau})^{\mathrm{T}}R_{o,u}^{-1}\hat{\alpha}_{o,u}^{\tau} - \frac{1}{2\sigma_0^2}\mathrm{tr}\left(\Psi_{o,u}^{\mathrm{T}}\Psi_{o,u}\hat{\Sigma}_{o,u}^{\tau}\right) - \frac{1}{2}\mathrm{tr}\left(R_{o,u}^{-1}\hat{\Sigma}_{o,u}^{\tau}\right) + \mathrm{const.}
\end{aligned}
$$

$$(5.18)$$

Maximizing $\Theta(\rho|\hat{\rho}^{\tau})$ as a function of ρ is not straightforward for $\zeta > 0$. At this step, we sub-optimally assume that ζ is small.[5] We can show that for $\zeta \to 0$, $R_{o,u}$ will be diagonal which results in the following update rules for ρ [99]:

$$
\begin{aligned}
\sigma_0^{\tau+1} &= \left[\frac{1}{n_w}\left(\mathrm{tr}\left(\Psi_{o,u}^{\mathrm{T}}\Psi_{o,u}\hat{\Sigma}_{o,u}^{\tau}\right) + \|\tilde{y} - \Psi_{o,u}\hat{\alpha}_{o,u}^{\tau}\|^2\right)\right]^{1/2}, \\
\sigma_k^{\tau+1} &= \left[\left[\hat{\Sigma}_{o,u}^{\tau}\right]_{k,k} + \left[\hat{\alpha}_{o,u}^{\tau}\right]_k^2\right]^{1/2}, \qquad k = 1, \cdots, n_{o,u}.
\end{aligned}
$$

$$(5.19)$$

Note that although (5.19) is the true EM update rule, some authors suggested suboptimal update rules that have a faster convergence rate in the general context of BCS [99]. Algorithm 1 shows the steps involved in estimating the map using our integrated occupancy grid and BCS method.

5.4 Integration of Occupancy Grid Mapping and Total Variation (TV) Minimization for Mapping with See-Through Capabilities

So far we have discussed an integrated BCS and occupancy grid mapping approach for wireless-based obstacle mapping of hidden objects. In the previous chapters, we have

---

[4]Here we have used the fact that for a Gaussian α, with mean $\hat{\alpha}$ and covariance Σ, we have $\mathbb{E}\{R\alpha\} = R\hat{\alpha}$ and $\mathbb{E}\{\alpha^{\mathrm{T}}R\alpha\} = \hat{\alpha}^{\mathrm{T}}R\hat{\alpha} + \mathrm{tr}(R\Sigma)$, for any positive definite R.

[5]Although we assume an uncorrelated map for the sake of estimating $\sigma_0, \cdots, \sigma_{n_{o,u}}$, the estimate of ζ of Eq. 5.16 is used when calculating $\hat{\alpha}_{o,u}^{\tau}$ and $\hat{\Sigma}_{o,u}^{\tau}$.

Algorithm 1: Integrated Occupancy Grid Mapping and BCS for See-Through Mapping

---

Input: $z_{1:t}$, $q_{1:t}$ (if poses are known) or $u_{1:t-1}$ (if poses are unknown), $\tilde{y}$, Ψ, α_{th}, ϑ_{th}, τ_{max}, $\sigma_{\mathrm{init,comm}}$, $\sigma_{\mathrm{init,cell}}$, tol, $\mathcal{X}$, ϵ

Output: Estimate of the binary map $\hat{x} = \begin{bmatrix} \hat{x}_f^{\mathrm{T}} & \hat{x}_o^{\mathrm{T}} & \hat{x}_u^{\mathrm{T}} \end{bmatrix}^{\mathrm{T}}$

Using $z_{1:t}$ and $q_{1:t}$ (or $u_{1:t-1}$), calculate $\vartheta_{k,t}$, for all k, using the occupancy grid approach of Section 5.2;

Calculate the set of indices $\mathcal{I}_f$, $\mathcal{I}_o$ and $\mathcal{I}_u$ and rearrange the elements of x and α accordingly as $x = \begin{bmatrix} x_f^{\mathrm{T}} & x_o^{\mathrm{T}} & x_u^{\mathrm{T}} \end{bmatrix}^{\mathrm{T}}$ and $\alpha = \begin{bmatrix} \alpha_f^{\mathrm{T}} & \alpha_o^{\mathrm{T}} & \alpha_u^{\mathrm{T}} \end{bmatrix}^{\mathrm{T}}$;

Set elements of $\hat{x}_f$ to zero and elements of $\hat{x}_o$ to one;

Using a set of maps $\mathcal{X}$, calculate $\hat{\zeta}$ using the approach of Section 5.3.1;

Set $\hat{\sigma}_0^0 = \sigma_{\mathrm{init,comm}}$ and $\hat{\sigma}_k^0 = \sigma_{\mathrm{init,cell}}$, for $k \in 1, \cdots, n_{o,u}$, assuming that the indices of the elements of $\alpha_{o,u} = \begin{bmatrix} \alpha_o^{\mathrm{T}} & \alpha_u^{\mathrm{T}} \end{bmatrix}^{\mathrm{T}}$ are $1, \cdots, n_{o,u}$;

for $\tau \leftarrow 0$ **to** τ_{max} **do**

    Calculate $\hat{\alpha}_{o,u}^\tau$ and $\hat{\Sigma}^\tau$ by substituting $\hat{\sigma}_0^\tau, \cdots, \hat{\sigma}_{n_{o,u}}^\tau$ and $\hat{\zeta}$ in (5.15);

    Calculate $\hat{\sigma}_0^{\tau+1}, \cdots, \hat{\sigma}_{n_{o,u}}^{\tau+1}$ using (5.19) or the suboptimal update rule of [99] with a better convergence rate;

    If $\max_{1 \le k \le n_{o,u}} \left| \log \frac{\hat{\sigma}_k^{\tau+1}}{\hat{\sigma}_k^\tau} \right| <$ tol break;

end

From the most updated $\hat{\alpha}_{o,u}^\tau$, use $\hat{\alpha}_u^\tau$ and set $\hat{x}_u = U(\hat{\alpha}_u^\tau > \alpha_{\mathrm{th}})$, where $U(.)$ is the vector indicator function;

---

considered a Total Variation framework for wireless-based mapping of hidden objects. In this section, we discuss how to integrate it with occupancy grid mapping. In the subsequent sections, we then compare the performance of the integrated occupancy grid/BCS-based and occupancy grid/TV-based approaches and discuss the underlying tradeoffs. As we previously discussed, the TV-based approach does not depend on estimating any underlying model parameters or assuming a specific model, which is an advantage over the BCS approach. However, the estimated variances of the BCS approach can provide a base for

guiding the robots to the places better for collecting wireless measurements, as we propose later in Section 5.6. Thus, in this chapter we consider integration based on both approaches and bring an understanding to the underlying tradeoffs.

We next explain how TV minimization can be used for mapping the portion of the workspace that cannot be seen by the onboard laser scanners of the robots. Without loss of generality, assume that the obstacle map of interest is a rectangular map and α is the vectorized version of the 2D signal that represents the wireless decay coefficients of the cells on the grid. Using (3.10), we then propose the following integrated approach for estimating the parts of the map that have not been seen by the laser scanners of the robots:

1. The sets $\mathcal{I}_f$, $\mathcal{I}_o$ and $\mathcal{I}_u$ are found using the laser measurements and following the same approach of Section 5.3. We then set $\hat{x}_k = 0$ for $k \in \mathcal{I}_f$, and $\hat{x}_k = 1$ for $k \in \mathcal{I}_o$.

2. The laser measurement matrix Ψ_{las} is formed. Each row of Ψ_{las} has n elements and corresponds to a cell $k \in \mathcal{I}_f$, with its kth element equal to $\log_{10} e$ and the rest of its $n - 1$ elements equal to zero.

3. The estimate $\hat{\alpha}$ of α is then found by solving the following TV minimization problem using the TVAL3 algorithm:

$$\min_{\alpha}\ \mathrm{TV}(\alpha),\ \text{subject to}\ \begin{bmatrix} \tilde{y} \\ 0 \end{bmatrix} = \begin{bmatrix} \Psi \\ \Psi_{\mathrm{las}} \end{bmatrix} \alpha. \tag{5.20}$$

4. For each $k \in \mathcal{I}_u$, we then set $\hat{x}_k = 1$ if $\hat{\alpha}_k > \alpha_{\mathrm{th}}$, and $\hat{x}_k = 0$ otherwise.

Algorithm 2: Integrated Occupancy Grid Mapping and TV minimization for See-Through Mapping

---

Input: $z_{1:t}$, $q_{1:t}$ (if poses are known) or $u_{1:t-1}$ (if poses are unknown), $\tilde{y}$, Ψ, α_{th} and ϑ_{th}

Output: Estimate of the binary map $\hat{x} = \begin{bmatrix} \hat{x}_f^{\text{T}} & \hat{x}_o^{\text{T}} & \hat{x}_u^{\text{T}} \end{bmatrix}^{\text{T}}$

Using $z_{1:t}$ and $q_{1:t}$ (or $u_{1:t-1}$), calculate $\vartheta_{k,t}$, for all k, using the occupancy grid approach of Section 5.2;

Calculate the set of indices $\mathcal{I}_f$, $\mathcal{I}_o$ and $\mathcal{I}_u$ and rearrange the elements of x and α accordingly as $x = \begin{bmatrix} x_f^{\text{T}} & x_o^{\text{T}} & x_u^{\text{T}} \end{bmatrix}^{\text{T}}$ and $\alpha = \begin{bmatrix} \alpha_f^{\text{T}} & \alpha_o^{\text{T}} & \alpha_u^{\text{T}} \end{bmatrix}^{\text{T}}$;

Set elements of $\hat{x}_f$ to zero and $\hat{x}_o$ to one;

Form the laser measurement matrix Ψ_{las};

Solve the TV minimization problem of (5.20) using a set of initial values for the Lagrange multipliers and α (the initial guess for α is usually the least square (LS) solution

$$\alpha^0 = \begin{bmatrix} \Psi^{\text{T}} & \Psi_{\text{las}}^{\text{T}} \end{bmatrix} \begin{bmatrix} \Psi\Psi^{\text{T}} & \Psi_{\text{las}}\Psi^{\text{T}} \\ \Psi_{\text{las}}\Psi^{\text{T}} & \Psi_{\text{las}}\Psi_{\text{las}}^{\text{T}} \end{bmatrix}^{-1} \begin{bmatrix} \tilde{y} \\ 0 \end{bmatrix});$$

From the estimated $\hat{\alpha}$ pick $\hat{\alpha}_u$ and set $\hat{x}_u = U(\hat{\alpha}_u > \alpha_{\text{th}})$, where $U(.)$ is the vector indicator function;

5.5 Coordinated vs. Random Wireless Channel Measurements

The quality of our wireless-based sampling depends heavily on the positions from which the map is sampled. In the previous chapters, we proposed two motion sampling strategies for wireless-based cooperative mapping based on TV minimization, namely *coordinated* and *random* approaches, which we will extensively use for our integrated approaches. Figure 5.3 summarizes both approaches. The left figure shows the robots making coordinated wireless measurements at $0°$. The trajectories indicated by the arrows in Fig. 5.3 (left), are examples of routes where coordinated measurements at angles $0°$ and $90°$ can be taken. Similar coordinated measurements can be made across any other angle.

As discussed in Chapter 4, having the robots move in a coordinated way may not always be possible due to environmental constraints. As such, we also consider a *random* measurement case, where the robots make wireless measurements at randomly-chosen TX-RX positions. Fig. 5.3 (right) shows an example of such a case.
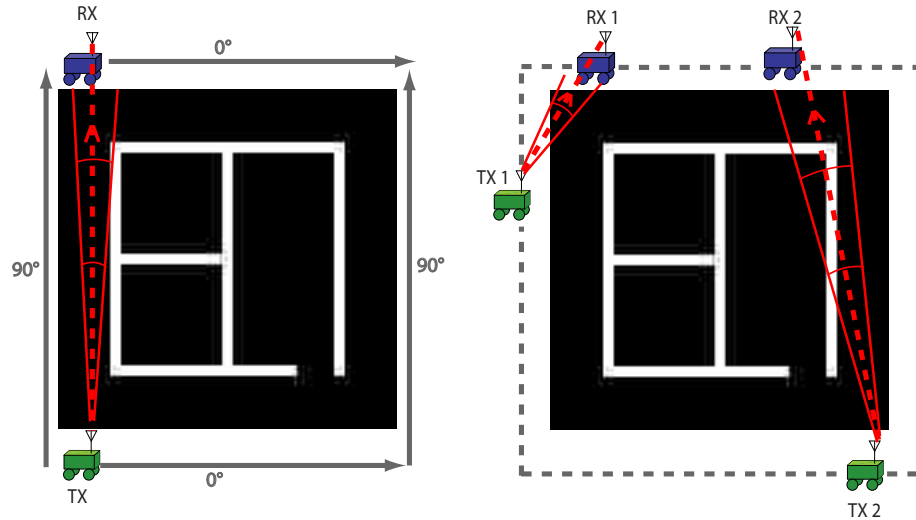
Figure 5.3: An illustration of wireless-based obstacle mapping with (left) coordinated wireless measurements and (right) random wireless measurements.

In Chapter 4, we established that in general TV minimization with coordinated measurements provides a better reconstruction quality and see-through capability, as compared to TV minimization with random measurements, as long as jump angles are sampled. It now becomes pertinent to understand how BCS compares to TV minimization in the context of both random and coordinated measurements. We start by comparing the performance of our integrated BCS-based and TV-based approaches in a simulation environment where we can test more scenarios. We then present our experimental results in Section 5.7.

Suppose that a pair of robots are trying to map the structure in Fig. 5.4. For the coordinated case, the robots move periodically along routes outside of the structure. Figure 5.3 (left) shows the routes where the robots move to make measurements along $0°$ and $90°$

routes. As the number of measurements increases, the robots make measurements along more angles, which are chosen so as to make the angle distribution as uniform as possible, while keeping the previously-chosen angles. For the random case, the robots make measurements at random positions along the dashed lines of Fig. 5.3 (right) without following a specific pattern.

Figure 5.4: An obstacle map with the obstacle areas denoted in white.

In order to motivate our discussion, we start by comparing the performance of these approaches for a noiseless case, i.e. when $\omega_{\mathrm{dB},i,j,t}$ of Eq. 5.1 is equal to zero. In this example, we assume that the positions of the robots are known at any time and that the reconstruction is based only on wireless measurements, i.e. no probabilistic grid mapping is used. We show the results as a function of the wireless sampling rate, where, as before, each sampling rate denotes the total number of wireless transmissions divided by the size of the 2D map in pixels. In this example, the size of the map is 64 by 64 pixels and the following underlying parameters are used: $\alpha_{\mathrm{th}} = 0.2$, $\sigma_{\mathrm{init,comm}} = 0$, $\sigma_{\mathrm{init,cell}} = 1$, $\hat{\zeta} = 0.2$ m, $\tau_{\mathrm{max}} = 150$ and $\mathrm{tol} = 0.001$ (see Algorithm 1 for more on tol). We discuss how we estimate the initial values of the underlying parameters for the BCS approach when we present our experimental results in Section 5.7.

Figure 5.5 shows the reconstruction using only 10% of measurements. As can be seen, TV minimization with coordinated measurements results in a perfect reconstruction. Furthermore, similar to TV minimization, BCS coordinated also has a smaller Normalized

Mean Squared Error (NMSE) than BCS random. As Fig. 5.6 shows, by increasing the number of measurements to 15%, a significant increase in the reconstruction quality of BCS coordinated is observed. For both cases (BCS and TV minimization), the coordinated approaches outperform the random ones. Furthermore, *for the random strategy, BCS has a better reconstruction quality than TV minimization.* Fig. 5.7 confirms the same trend in the noiseless case, for a range of percentage measurements.

BCS coordinated (NMSE = −5.57093 dB)   BCS random (NMSE = −2.45513 dB)

TV coordinated (NMSE = −Inf dB)   TV random (NMSE = −0.523881 dB)
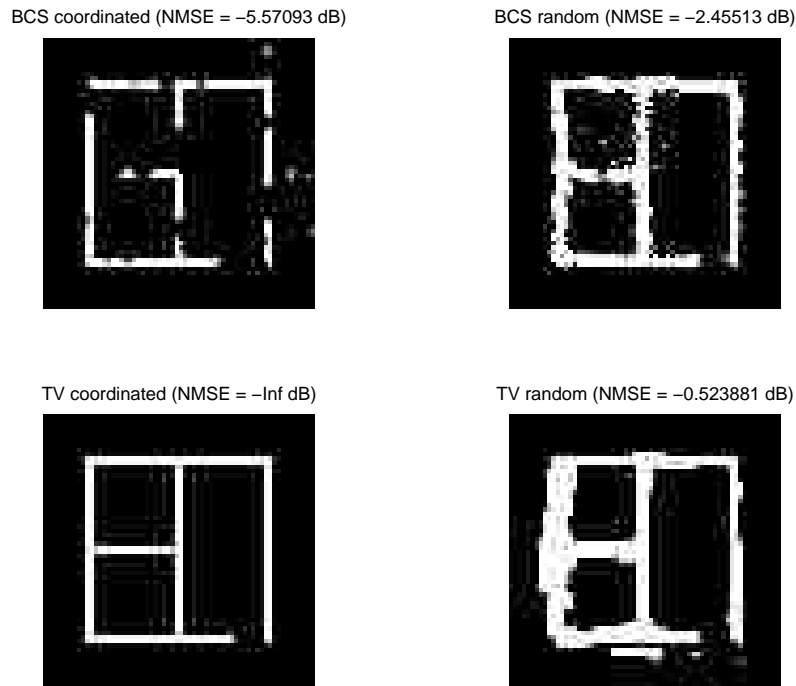
Figure 5.5: The reconstruction of the obstacle of Fig. 5.4 using 10% noiseless simulated measurements.

Next, we consider the impact of noise. As we indicated in the wireless channel measurement model of Eq. 5.12, the elements of ω_{dB} are taken to be uncorrelated Gaussian random variables with the variance σ_0^2. We furthermore showed that this assumption does indeed provide a good match with the data obtained using our experimental robotic platform. We next show the effect of such noise in a simulation environment with the same parameters as before except for: $\tau_{max} = 500$ and $\sigma_{init,comm} = \sigma_0$.
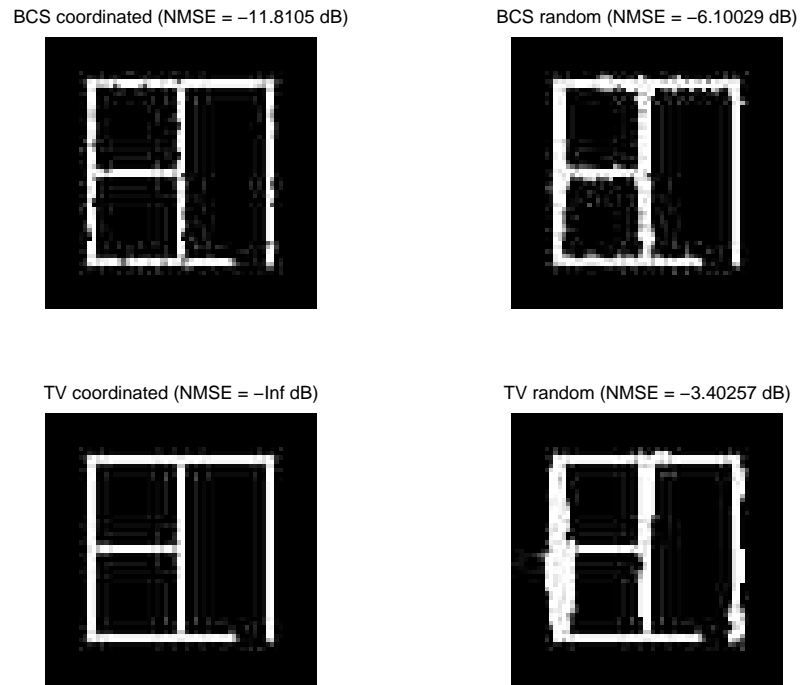
Figure 5.6: The reconstruction of the obstacle of Fig. 5.4 using 15% noiseless simulated measurements.
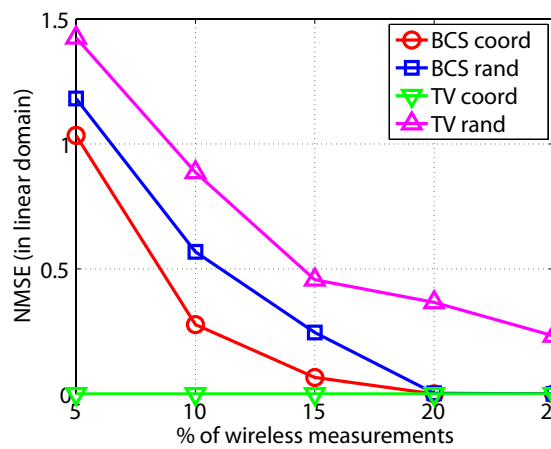
Figure 5.7: NMSE versus the percentage of wireless measurements in the noiseless case for the reconstruction of the obstacle of Fig. 5.4.

Figures 5.8 and 5.9 show the mapping performance using 15% noisy measurements with $\sigma_0 = 0.1$ and $\sigma_0 = 0.2$ respectively. As can be seen, similar to the noiseless case, the coordinated approaches provide a better reconstruction quality than the random ones. Furthermore, TV minimization with random measurements has the worse performance for these two sample noise variances. Fig. 5.10 then shows the NMSE as a function σ_0. It can be seen that similar trends hold in this figure except at very low values of σ_0 where the random TV starts outperforming the random BCS. However, the reconstruction quality at such high level of noise may not be acceptable anymore.

BCS coordinated (NMSE = −6.52227 dB) BCS random (NMSE = −1.15823 dB)

TV coordinated (NMSE = −6.7497 dB) TV random (NMSE = 0.992725 dB)
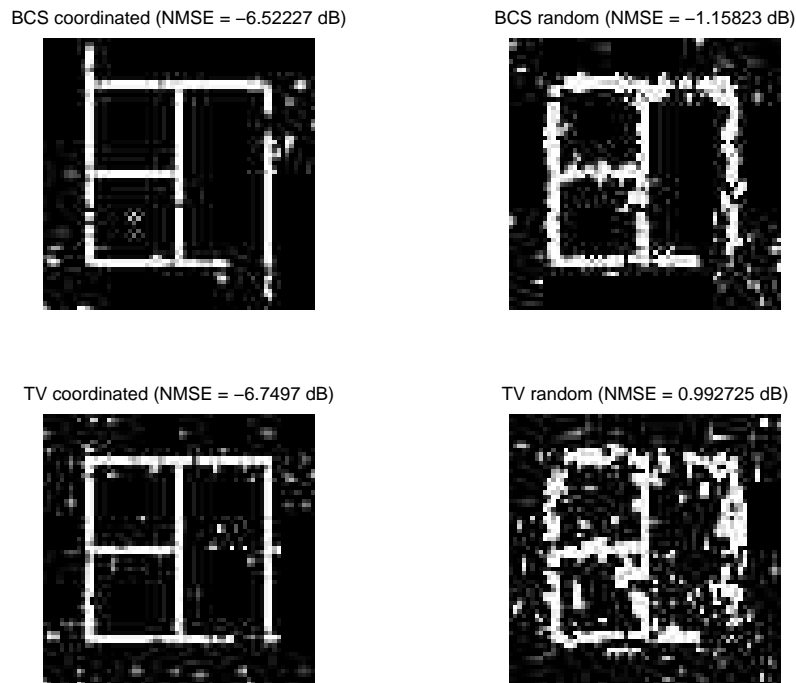
Figure 5.8: The reconstruction of the obstacle of Fig. 5.4 using 15% noisy simulated wireless measurements ($\sigma_0 = 0.1$).
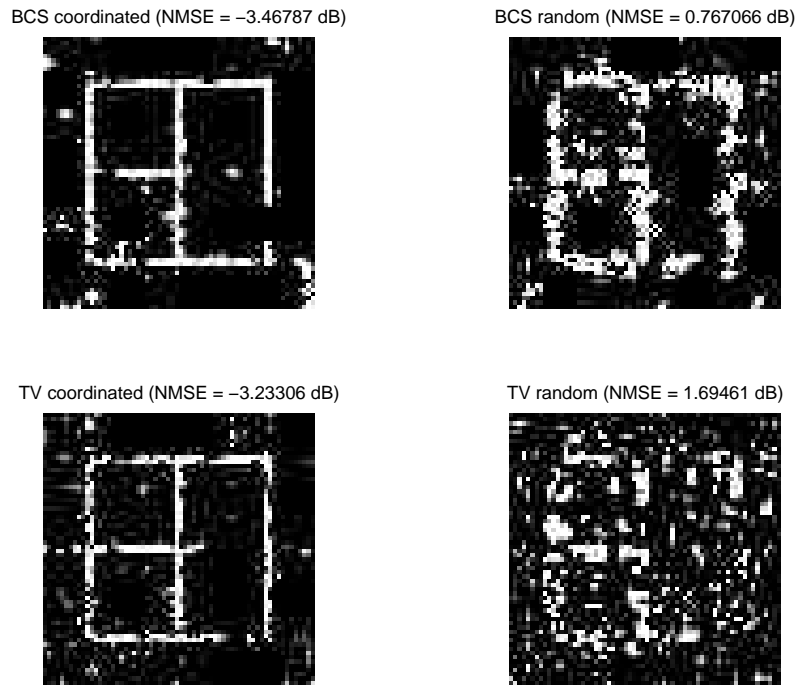
Figure 5.9: The reconstruction of the obstacle of Fig. 5.4 using 15% noisy simulated wireless measurements ($\sigma_0 = 0.2$).

5.6 An Adaptive Data Collection Strategy for Integrated Obstacle Mapping

So far, we have assumed that the laser and wireless channel measurements are collected through either random or coordinated motion patterns, without an online optimization of the data collection process. The trajectories can further be adapted online to better collect laser or wireless channel measurements based on a feedback from the current mapping quality. Online motion optimization for occupancy grid mapping, using laser measurements, has been extensively studied in the robotics literature. Examples include next-best-view (NBF) [102] and frontier-based [103, 104] algorithms. However, online motion adaption based on a feedback from the current mapping quality for wireless-based see-through mapping has not been studied before. In this section, we propose an adaptive strategy for
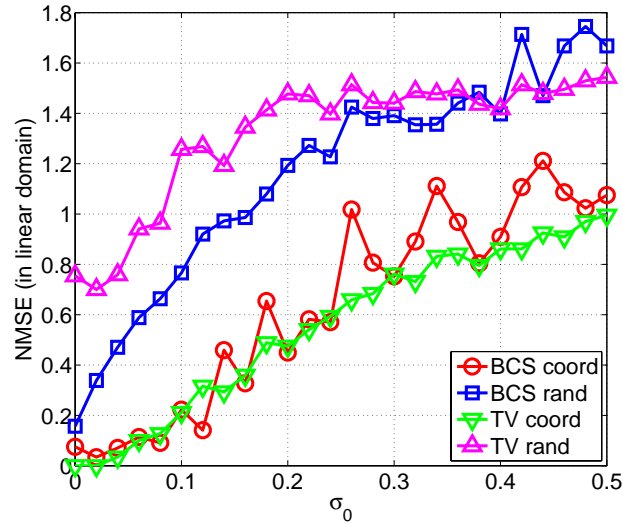
Figure 5.10: NMSE versus σ_0 for the reconstruction of the obstacle of Fig. 5.4 with 15% simulated wireless measurements.

collecting wireless channel measurements that aims to improve the see-through performance of either BCS or TV minimization methods.

Consider the obstacle-free part of the workspace $\mathcal{W}_f \subset \mathcal{W}$, estimated using the occupancy grid approach of Section 5.2. Without loss of generality, assume that there exists only one pair of TX and RX robots. Let $\mathcal{P} \subset \mathcal{W}_f$ denote the set of possible positions where the robots can be. For instance, $\mathcal{P}$ could be the set of positions along the rectangle that surrounds the workspace (see the dashed line of Fig. 5.3 (right) for an example). Consider the wireless channel measurements available to the robots at time t. These channel measurements include the channel measurements collected by the robots along their trajectories up to time t, and possibly a set of *a priori* channel measurements available at the beginning of the operation. The idea is to choose the next best positions of the robots such that the new channel measurement at time $t + 1$ is the most informative, given the past measurements.

We specifically propose two adaptive approaches: *ad-hoc* and *variance-based*. The

ad-hoc approach can be used to adaptively collect wireless measurements in both BCS and TV minimization methods. The variance-based approach, on the other hand, uses the estimated variance of the BCS case and is therefore only applicable to the BCS method.

Let Ψ_t denote the measurement matrix found based on the available wireless channel measurements up to time step t. Also let $\Psi_{o,u,t}$ denote the part of Ψ_t that corresponds to the occupied and unknown cells whose indices are in the set $\mathcal{I}_{o,u}$, which is given at the end of the occupancy grid mapping operation. Additionally, let $\hat{\Sigma}_{o,u,t}$ represent the estimated covariance matrix $\Sigma_{o,u}$ in the BCS method, calculated based on the available wireless channel measurements up to time t. The column vector of the diagonal elements of $\hat{\Sigma}_{o,u,t}$ is then shown by $\mathrm{diag}\big(\hat{\Sigma}_{o,u,t}\big)$. At any time t, the set of admissible pairs of positions for the RX and TX robots is a subset of $\mathcal{P} \times \mathcal{P}$ defined as follows:

$$\mathcal{F}_t \triangleq \Big\{ (p_1, p_2) \in \mathcal{P} \times \mathcal{P} \,\Big|\, \|\xi_{i,t} - p_i\| \leq d_{\max}, \; i = 1, 2,$$
$$\text{dir. antennas can be aligned along } \mathcal{L}(p_1, p_2) \Big\}, \tag{5.21}$$

where $d_{\max}$ is the maximum step size of the robots and $\mathcal{L}(p_1, p_2)$ denote the line segment between p_1 and p_2. Note that due to possible constraints on the rotation of the onboard antennas of the robots, some of the points may not be feasible and need to be excluded from the set of admissible points. For any pair of positions $(p_1, p_2) \in \mathcal{F}_t$ we then propose the following ad-hoc and variance-based next position optimization problem:

- Ad-hoc:

$$(\xi_{1,t+1}, \xi_{2,t+1}) = \operatorname*{argmax}_{(p_1,p_2)\in\mathcal{F}_t} \psi_{o,u}^{\mathrm{T}}(p_1, p_2) \exp\big(- \Psi_{o,u,t}^{\mathrm{T}} 1 \big), \tag{5.22}$$

- Variance-based:

$$(\xi_{1,t+1}, \xi_{2,t+1}) = \operatorname*{argmax}_{(p_1,p_2)\in\mathcal{F}_t} \psi_{o,u}^{\mathrm{T}}(p_1, p_2) \mathrm{diag}\big(\hat{\Sigma}_{o,u,t}\big), \tag{5.23}$$

where $\Psi_{o,u,t}^{\mathrm{T}} 1$ denotes the column vector of the column-sum of matrix $\Psi_{o,u,t}$ and $\psi_{o,u}(p_1, p_2)$ denotes the column vector corresponding to the parts of $\psi(p_1, p_2)$ that are in $\mathcal{I}_{o,u}$. The intuition behind the ad-hoc strategy is that the new measurement vector $(\psi^{\mathrm{T}}(\xi_{1,t+1}, \xi_{2,t+1}))$ should have a small correlation with the existing measurement vectors, i.e. rows of Ψ_t. This will increase the probability that the new wireless measurement (the line segments between the TX and RX robots) hits the cells that are not yet visited. We have further found that amplifying the impact of the unvisited cells by using the exponential function can improve the performance. The ad-hoc strategy (5.22) then chooses the pair whose connecting line segment passes through the cells that have previously been visited the least. This strategy can be used with both BCS and TV. The variance-based optimization function of (5.23), on the other hand, is based on the summation of the variances of the cells that the new wireless measurement line hits. Thus, the new measurement line is chosen such that the cells with high variances (high uncertainty) are selected. As expected, the variance-based approach can be more informative for adaptation, which is an advantage of using BCS over TV.

Algorithm 3 summarizes our adaptive strategy for collecting wireless channel measurements.

We next show the performance of our online adaption integrated mapping framework in a simulation environment. Consider the case where the robots are trying to reconstruct the obstacle map of Fig. 5.4 based on only noiseless wireless measurements. We will show the performance of the non-ideal case when we discuss our experimental results in the next section.

Assume that no occupancy grid mapping is performed, i.e. $\Psi_t = \Psi_{o,u,t}$ for all t. For this example, we let $\mathcal{P}$ correspond to a set of discrete positions along the square dashed line that surrounds the map of interest (see Fig. 5.3 (right)). The size of the map is 64×64 pixels. Thus, we let the admissible positions be evenly distributed along the dashed line such that $\mathrm{card}(\mathcal{P}) = 256$. We also set $\mathcal{F}_t \triangleq \left\{ (p_1, p_2) \in \mathcal{P} \times \mathcal{P} \right\}$.

Algorithm 3: Adaptive Path Planning for our Integrated Obstacle Mapping

---

Input: t_{oper}, $\mathcal{P}$, $\mathcal{I}_f$, $\mathcal{I}_o$, $\mathcal{I}_u$, $\tilde{y}_0$, Ψ_0 (*a priori* wireless channel measurements)

Output: The trajectory of the TX and RX robots as well as an extra set of wireless channel
        measurements

for $t \leftarrow 0$ **to** t_{oper} **do**

    Estimate the $\alpha_{o,u}$ based on the available wireless channel measurements $\tilde{y}_t$ and Ψ_t;

    Calculate the admissible set $\mathcal{F}_t$ using the current positions of the robots;

    Calculate $(\xi_{1,t+1}, \xi_{2,t+1})$ using either (5.22) or (5.23). The variance-based strategy of
    (5.23) uses the current estimate of covariance matrix, $\hat{\Sigma}_{o,u,t}$;

    Navigate the robots to $\xi_{1,t+1}$ and $\xi_{2,t+1}$;

    Collect the new wireless channel measurement and add it to $\tilde{y}_t$ to form $\tilde{y}_{t+1}$. Also, set

$$\Psi_{t+1} = \begin{bmatrix} \Psi_t \\ \psi^{\mathrm{T}}(\xi_{1,t+1}, \xi_{2,t+1}) \end{bmatrix}$$

end

At the beginning of the operation, the robots make a very small number of random wireless measurements, corresponding to 3% of the map. The reconstruction of BCS and TV minimization using these initial measurements is shown in Fig. 5.11. For BCS, the same parameters of the example of Fig. 5.7 is used. The robots then proceed to make additional wireless measurements based on our online adaptive approach, choosing the next best positions out of $\mathcal{F}_t$. We assume that d_{max} is infinite and that any pair of positions can be selected from $\mathcal{F}_t$. Fig. 5.12 shows the quality of adaptive mapping after 15% measurements are adaptively collected. As can be seen, the mapping quality has improved considerably. It can furthermore be seen that, while the ad-hoc methods result in an acceptable reconstruction quality, the variance-based approach outperforms the adhoc strategies as expected. Figure 5.13 shows the mapping performance curves as a function of the percentage of the additional wireless measurements. As can be seen, BCS approaches perform better than TV and the variance-based approach outperforms the adhoc one. These results highlight an advantage of mapping based on BCS by using the estimated variances.

However, due to the same reason, BCS also requires an initial estimation of the underlying model parameters, which can make it prone to error propagation.

Original   BCS (NMSE = 1.65 dB)   TV minimization (NMSE = 2.00 dB)
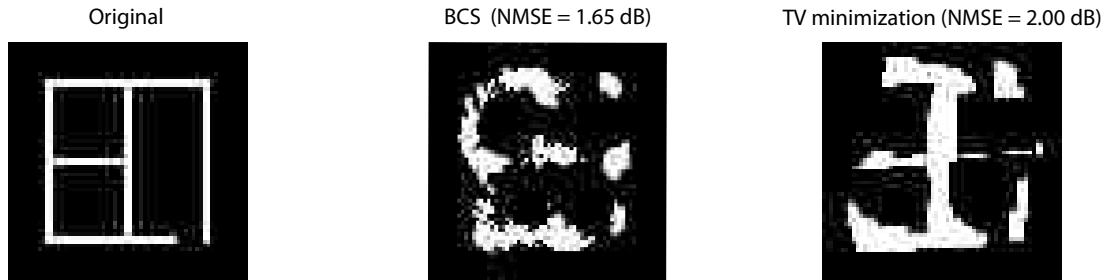
Figure 5.11: Initial reconstruction of the obstacle of Fig. 5.4 based on 3% noiseless simulated wireless measurements.

5.7 Experimental Results

So far we have proposed two approaches for integrating occupancy grid mapping (using laser measurements) with CS mapping (using wireless channel measurements). In this section, we show the performance of our two approaches in the reconstruction of a real structure that includes an occluded part. We start by describing the additions we made to our experimental robotic setup in order to enable our proposed integrated approach.

5.7.1 Summary of the Experimental Setup to Enable our Proposed Integrated Approach

In Chapter 2, we described our experimental setup, which consisted of Pioneer P3-AT robots equipped with directional narrow-beam antennas and the corresponding servo mechanisms for antenna rotation. In order to test our proposed integrated approach, we equipped each robot with a Hokuyo URG laser scanner which has a maximum range of

Original   BCS variance−based (NMSE = −Inf dB)

TV ad-hoc (NMSE = −3.38 dB)   BCS ad-hoc (NMSE = −6.84 dB)
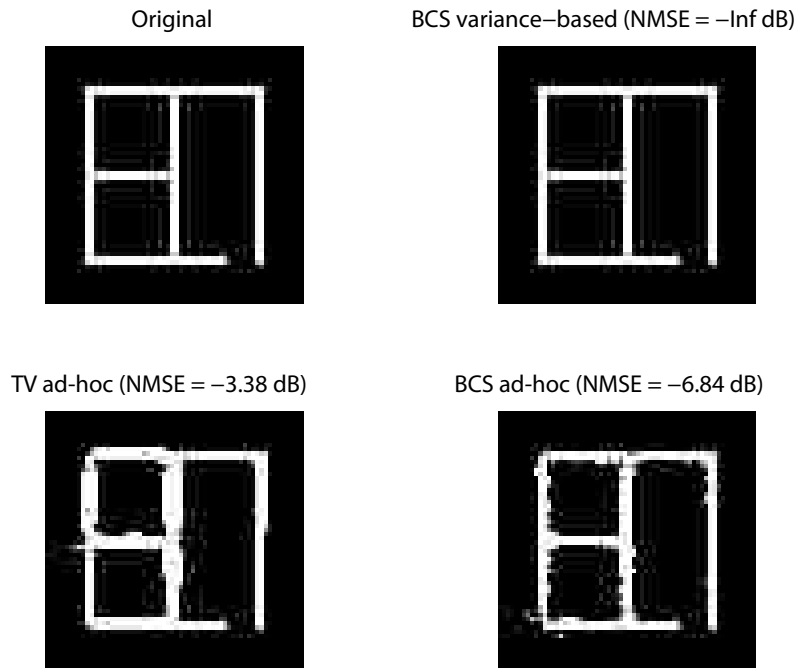
Figure 5.12: The reconstruction of the obstacle of Fig. 5.4 after 15% additional adaptive wireless measurements are collected.

5.6 m and a scanning angle of $240°$. Figure 5.14 (left) shows the resulting platform with the laser scanner and the directional antenna. Figure 5.14 (right) shows the robots making wireless measurements in order to see through the walls and reconstruct the obstacle inside while the onboard laser scanners are used to map the portions of the workspace that can be directly seen by the laser scanners.

In addition to the software package that we developed in order to collect RSSI measurements between the two robots (see Chapter 2 for the details), we have developed an additional software package for motion planning and occupancy grid mapping using laser scanners. This second software package is developed in C++ under Linux and makes use of the Robot Operating System (ROS) [105] for controlling the Pioneer P3-AT platform
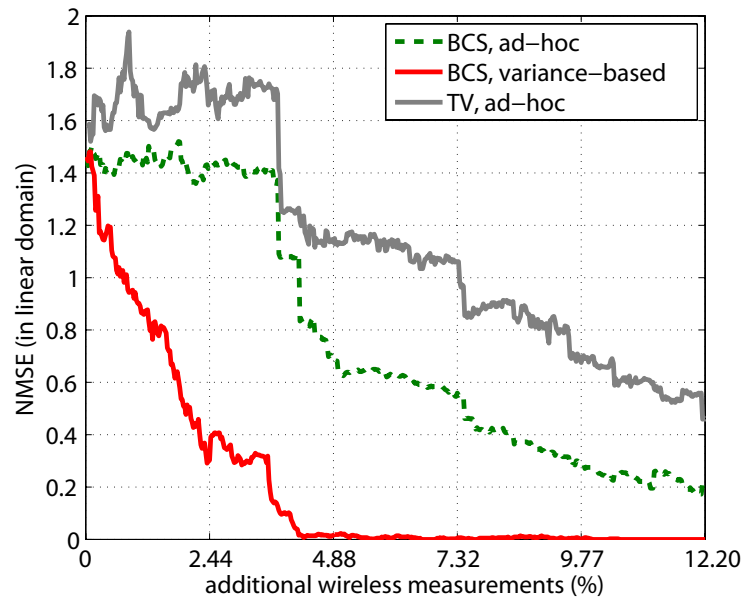
Figure 5.13: MSE as a function of the percentage of the additional wireless measurements for our adaptive path planning strategy, in reconstructing the whole map of Fig. 5.4 (3% initial random measurements were used)

.

(using p2os stack), operating the Hokuyo URG laser scanner (using hokuyo_node laser driver) and implementing SLAM (using the gmapping stack). The main application of this package runs as a ROS node itself and is in charge of controlling the robot, preprocessing the map built by the SLAM algorithm and logging it into a log file in real-time for postprocessing in MATLAB.

We then implement our integrated framework in MATLAB by using the RSSI data collected by the robots and the occupancy grid map that is given by the SLAM algorithm to build the entire map of the structure.

Figure 5.14: (left) A Pioneer P3-AT robot equipped with our servo control mechanism /fixture, adaptive narrow-beam directional antenna and Hokuyo laser scanner; (right) two robots using laser scanners and wireless measurements in order to map an obstacle structure that includes occluded parts.

5.7.2 Experimental Results for Mapping a Structure with Occluded Parts

We next show the performance and see-through capabilities of our proposed integrated approach in mapping an obstacle structure that has occluded parts. Figure 5.15 (left) shows a structure with its horizontal cut shown in the right figure. First, consider the case where a robot only uses its laser scanner outside of the structure as far as it can get using the entrance on the lower right side. In order to avoid the laser scanner falsely detecting the antenna as an obstacle, we set the gmapping algorithm to discard any laser reading beyond the range $-60°$ to $60°$ (with respect to the robot frame). Fig. 5.16 (b) shows the resulting generated map. As can be seen, the existence, position and dimensions of the occluded parts can not be determined by the laser scanner, as expected. Thus, we let the robots do a few random wireless measurements along the dashed trajectories of Fig. 5.15 (right) and apply our proposed integrated approach.[6] The following parameters are used for the BCS

---

[6]Note that the robots make wireless measurements when positioned on the dashed line of Fig. 5.15 (right) in our experiment. If one robot transmits from inside the structure (using the entrance

case: $\alpha_{\text{th}} = 7$, $\sigma_{\text{init,comm}} = 10.34$. The rest of the parameters are the same as in Section 5.5. As pointed out before, we estimated ζ by using several existing real maps a priori and applying Eq. 5.16. We consistently found that BCS is not as sensitive to the initialization of $\sigma_{\text{init,cell}}$ and therefore we have fixed it to a small value of one. As for $\sigma_{\text{init,comm}}$, we have used a priori wireless measurements with other structures that we have constructed in the past and estimated ω_{dB} by subtracting the impact of the structure to measure samples of the noise as illustrated in Fig. 5.2. We then calculated the standard deviation of this noise.

Subfigures (e) and (f) of Fig. 5.16 show the performance of our proposed integrated approach with BCS and TV minimization respectively. As can be seen, even at the very low sampling rate of 18% of the unknown part, corresponding to 6% of the overall map, the occluded wall can be clearly seen. The unknown part refers to the area where the laser scanner can not see the obstacles as marked in Fig. 5.16 (b). 18% wireless measurements is then the percentage of the wireless measurements as compared to the total number of pixels of the unknown part. This percentage translates to 6% of the overall map, which is fairly small. It can be seen that the robots can map the structure with our integrated approach. Furthermore, it can be observed that random BCS performs better than random TV as we expected from the simulation results of the previous section. For the sake of comparison, Fig. 5.16 (c) and (d) show the reconstruction if we only use the collected wireless measurements (6% wireless measurements), without integration with the laser scanner data. As can be seen, it is hard to map this structure based on only 6% wireless measurements that are collected from the dashed line of Fig. 5.15 (right), which motivates the use of the integrated approach.

We next show the performance of our proposed adaptive exploration strategy of Section 5.6 in an experimental setup. In the previous section we showed through simulations that an adaptive strategy can improve the wireless-based mapping performance. In addition to doing SLAM, which yields the reconstruction previously shown in Fig. 5.16 (b), we

---

on the lower-right corner), better reconstructions can be achieved.

Figure 5.15: (left) The obstacle structure of interest and (right) its horizontal cut. The paths where the robots can make random wireless measurements are marked with dashed lines in the right figure.

let the robots take a very small number of random wireless measurements of 2.7% of the unknown part, along the dashed trajectories of Fig. 5.15 (right). As can be seen in Fig. 5.17, this does not yield a good enough reconstruction quality, with neither the BCS nor the TV minimization approaches. The variance of this reconstruction is shown in Fig. 5.18 for the integrated BCS approach. For the BCS case, we use $\sigma_{\text{init,comm}} = 10.25$ and $\hat{\zeta} = 0.1$ m. The rest of the parameters are the same as the ones used for Fig. 5.16. Our proposed variance-based approach then aims at making additional wireless measurements such that the wireless ray crosses as many cells with high variances as possible. By utilizing our adaptive strategy, the reconstruction quality is significantly improved, as Fig. 5.19 shows. Furthermore, we can observe that with the same number of measurements, the variance-based approach has the best performance (measured by the NMSE), followed by the ad-hoc based approaches with BCS and TV. Fig. 5.20 shows the variance of the reconstruction after utilizing the variance-based strategy, which is considerably smaller than that of Fig. 5.18, as expected. Finally, Fig. 5.21 shows the performance of the adaptive approaches as a function of the percentage of the additional wireless measurements. It can be seen that the variance-based approach outperforms the ad-hoc ones after a few steps. In this adaptive experiment, the new pair of TX/RX positions is selected from an existing pool of available wireless measurements that were made along the dashed trajectories of Fig.
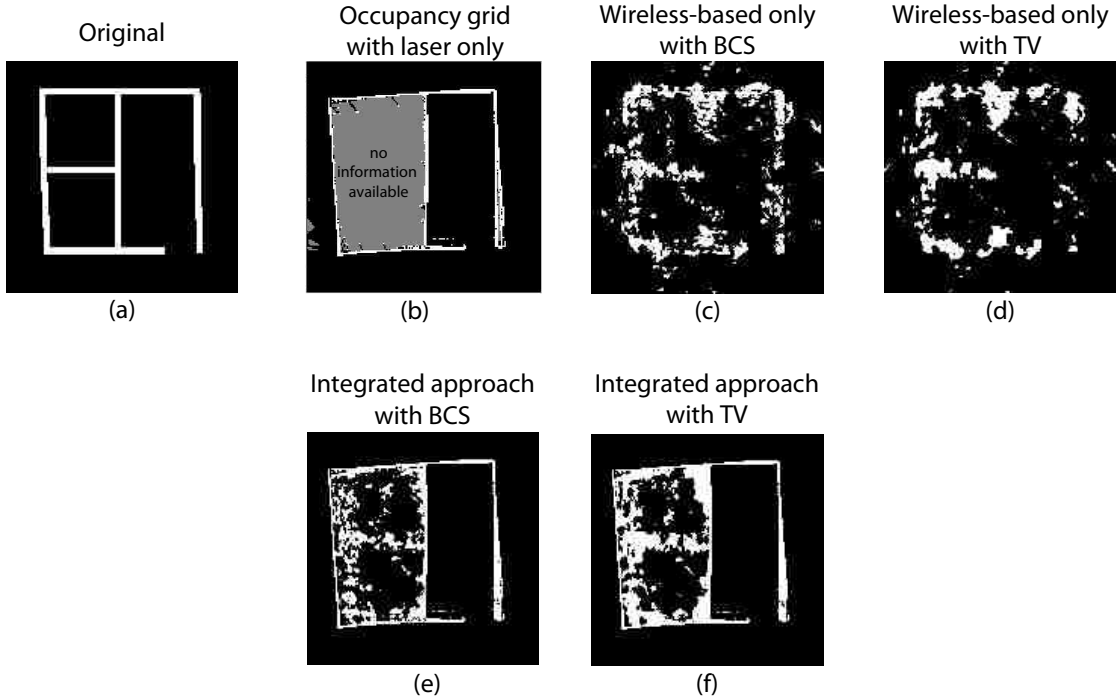
Figure 5.16: (a) Horizontal cut of the obstacle map of Fig. 5.15, (b) occupancy grid mapping with laser scanners, reconstruction using wireless measurements with (c) BCS and (d) TV minimization, our proposed integrated framework with (e) BCS and (f) TV minimization. The percentage of wireless measurements is 18% of the unknown part, which corresponds to 6% of the overall map.

5.15 (right). Both the transmitter and receiver positions are uniformly distributed along the dashed lines. For each TX/RX pair a wireless measurement is available, while avoiding the cases where both transmitting and receiving robots are on the same side of the structure. We assume that $d_{\max}$ is infinite. The next position $(\xi_{1,t+1}, \xi_{2,t+1})$ is then chosen using our proposed strategies. Note that random wireless measurements are used for all the experimental results, as mentioned earlier.

In summary, our experimental results confirmed that the proposed integrated framework can map occluded obstacles based on a small number of wireless measurements and overcome the deficiencies of both laser-based and wireless-based mapping approaches.

Furthermore, our adaptive wireless measurement collection can further improve the performance. Finally, both integrated TV and BCS-based approaches provide comparable reconstruction results, with the BCS-based approach performing better with random measurements and TV-based approach with coordinated measurements. Additionally, the BCS-based approach can result in a better online adaptation by utilizing the estimated variance information. However, integrated BCS-based approach requires estimating the underlying model parameters as compared to the TV-based approach. This needs an initial estimation of the model parameters, which can be prone to errors. Thus, depending on the system requirements, the integrated mapping choice that is more suitable can be selected in practice.
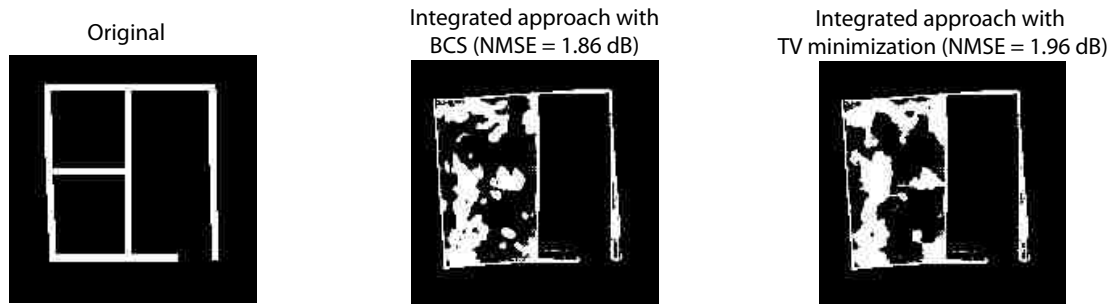
Figure 5.17: The reconstruction of the obstacle of Fig. 5.15 using laser scanner data and 193 wireless measurements (corresponding to 2.7% of the unknown part or 0.8% of the overall map). As can be seen, the number of collected wireless measurements is too small to detect the occluded parts.

5.8   Summary

In this chapter we considered the problem of obstacle/object mapping using a team of mobile robots that are equipped with a laser scanner, a wireless communication device and a directional antenna. We proposed an integrated framework for mapping with see-
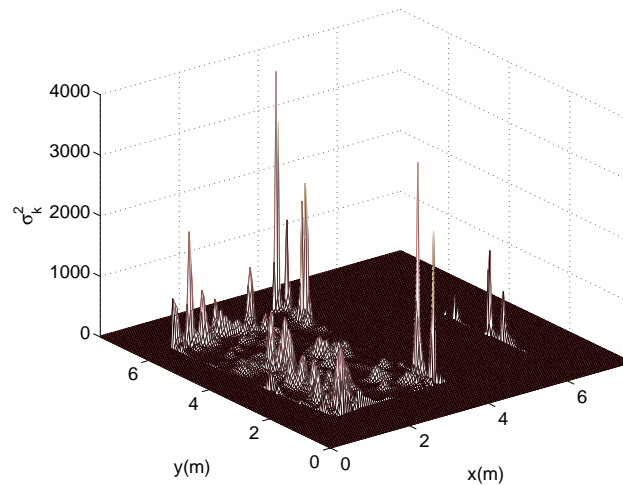
Figure 5.18: Variance of the reconstruction of Fig. 5.17 for the integrated BCS-based strategy.

through capabilities based on both laser and wireless channel measurements. We specifically showed how to integrate occupancy grid mapping with two CS-based reconstruction methods: Bayesian compressive sensing (BCS) and total variation (TV) minimization. We compared the performance of these two approaches using both simulated and real data from our robotic platforms. For instance, our results indicated that the integrated BCS-based method is more appropriate for mapping based on random wireless measurements while TV-based integrated approach performs better with coordinated wireless measurements. The integrated BCS-based approach furthermore provides an estimate of the variance, which can be more informative for adaptive path planning and wireless measurement collection. It, however, requires an initial estimation of the underlying model parameters. We finally proposed an adaptive path planning strategy that utilizes the current estimate of uncertainty to better guide the robots for wireless measurement collection.
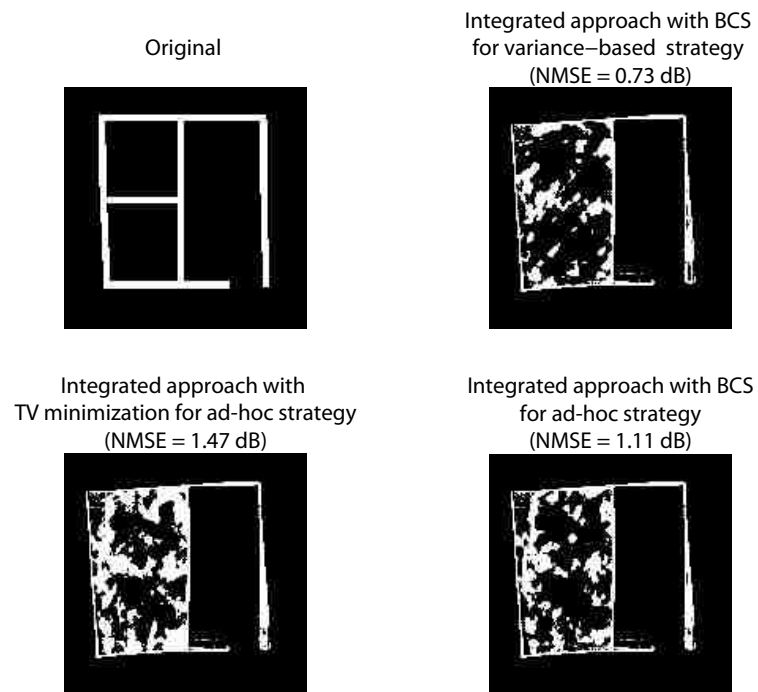
Figure 5.19: Improvement to the reconstruction of Fig. 5.17 based on an additional 7.03% (of the unknown part) wireless measurements that are collected using our adaptive strategies of Section 5.6.
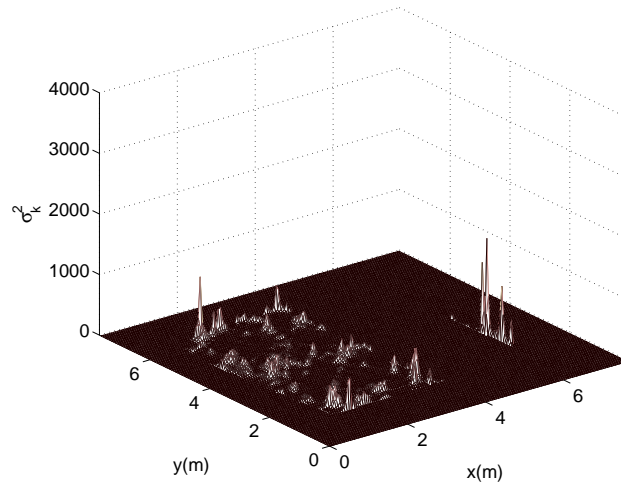
Figure 5.20: Variance of the reconstruction of Fig. 5.19 for the integrated BCS adaptive variance-based strategy.
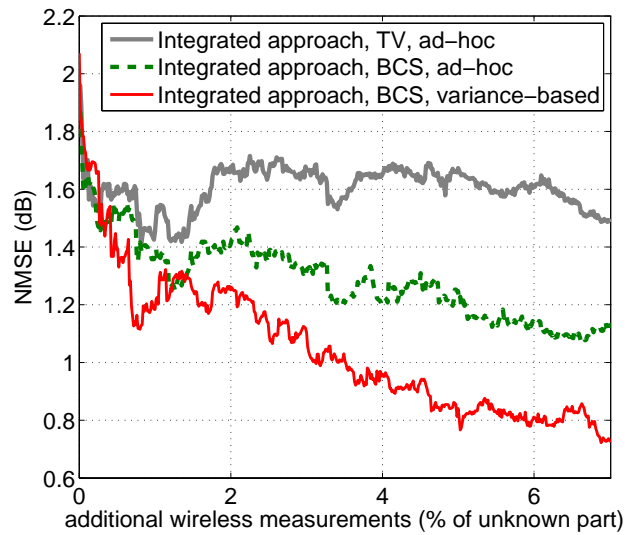
Figure 5.21: MSE versus number of additional wireless measurements for the proposed adaptive motion planning strategies of Section 5.6. Initial wireless measurements corresponding to 2.7 % of the unknown part or 0.8% of the whole map are used.

Chapter 6

Conclusion and Future Extensions

In this dissertation, we considered the problem of obstacle/object mapping in robotic networks. Our goal was to develop a framework for mapping obstacles, including occluded ones, by using a small number of wireless measurements. We started by tapping into the knowledge available in the wireless communication literature in order to provide a comprehensive overview of the key underlying dynamics of wireless channels: small-scale fading, shadowing and the distance-dependent path loss. We confirmed the characteristics of these dynamics experimentally by making an extensive number of channel measurements with our robotic testbed. In order to automate the channel measurement process, we developed a robotic testbed and showed how adaptive directional antennas can effectively reduce the effects of multipath fading on the received signal strength.

We then proceeded with our wireless-based obstacle mapping framework. The framework was based on the fact that the shadowing component of a wireless transmission contains implicit information on the objects located on the path between the transmitter and receiver. In order to limit the number of needed measurements we made use of compressive sampling theory. Specifically, we exploited the sparse representation of the map in space, wavelet and total variations in order to build it with minimal sensing, and without

directly sensing a large percentage of the area. We also considered different reconstruction approaches based on Basis Pursuit, Matching Pursuit and Total Variation minimization.

We then showed the underlying tradeoffs of different sampling, sparsity and reconstruction techniques. For instance, we saw that coordinated space or frequency sampling with total variation minimization can provide a good reconstruction quality. We established that the right way to compare the performance of the random and coordinated sampling patterns is to consider the relationship between the reconstruction quality and the angular directions where the map is sampled. More specifically, we showed that the total number of available channel measurements should be distributed over a small number of angles (bigger than or equal to the number of jump angles of the structure), with a preference given to the angles of jumps.

Finally, we considered a scenario where each robot is equipped with a laser scanner, a wireless communication device and a directional antenna. We proposed an integrated framework for mapping with see-through capabilities that allows the robots to use laser scanners to map areas that can be directly sensed, and wireless channel measurements to map the occluded areas. We specifically showed how to integrate occupancy grid mapping with two compressive sensing reconstruction methods: Bayesian compressive sensing (BCS) and TV minimization. We compared the performance of these approaches using simulated and real data from our robotic platforms. For instance, our results indicated that the integrated BCS-based method is more appropriate when using random wireless measurements, while the TV-based integrated approach performs better for coordinated wireless measurements. The integrated BCS-based approach furthermore provides an estimate of the variance, which can be more informative for adaptive path planning and wireless measurement collection. It, however, requires an initial estimation of the underlying model parameters. We then proposed an adaptive path planning framework that utilizes the current estimate of uncertainty to better guide the robots for further wireless measurement collection.

We further validated all our findings with our experimental robotic testbed. We showed the performance of our framework in efficiently mapping a number of real obstacles (including blocked ones).

There are several possible extensions of this work. For instance, mapping of more complicated structures would be an immediate extension. Along this line, understanding the complexity of the map and the related required number of wireless measurements is an interesting problem. As we indicated in previous chapters, multipath fading can negatively impact the mapping performance of our proposed framework. For the experimental platform used in this dissertation, we used transceivers operating at 2.4 GHz. Exploring other frequencies and understanding their tradeoffs for wireless-based mapping is the subject of our future work. Finally, improving the modeling of the wireless transmission to include more propagation phenomena is another line of future work.

References

[1] W. C. Jakes, *Microwave Mobile Communications*. New York: Wiley-IEEE Press, 1994.

[2] A. Goldsmith, *Wireless Communications*. Cambridge University Press, 2005.

[3] E. Candès, J. Romberg, and T. Tao, "Robust uncertainty principles: exact signal reconstruction from highly incomplete frequency information," *IEEE Trans. on Information Theory*, vol. 52, no. 2, pp. 489–509, February 2006.

[4] D. L. Donoho, "Compressed sensing," *IEEE Transactions on Information Theory*, vol. 52, no. 4, pp. 1289–1306, April 2006.

[5] D. Needell and R. Vershynin, "Signal recovery from incomplete and inaccurate measurements via regularized orthogonal matching pursuit," *Selected Topics in Signal Processing, IEEE Journal of*, vol. 4, no. 2, pp. 310 –316, april 2010.

[6] Y. Mostofi, "Compressive Cooperative Sensing and Mapping in Mobile Networks," *IEEE Transactions on Mobile Computing*, vol. 10, no. 12, pp. 1769–1784, Dec. 2011.

[7] ——, "Compressive cooperative obstacle/object mapping and see-through capabilities in robotic networks,," 2012, accepted to appear, IEEE Transactions on Mobile Computing.

[8] Y. Mostofi and P. Sen, "Compressive Cooperative Mapping in Mobile Networks," in *Proceedings of the 28th American Control Conference (ACC)*, St. Louis, MO, June 2009, pp. 3397–3404.

[9] I. F. Akyildiz, S. Weilian, Y. Sankarasubramaniam, and E. Cayirci, "A Survey on Sensor Networks," *IEEE Communications Magazine*, vol. 40, no. 8, pp. 102 – 114, Aug. 2002.

References

[10] V. Kumar, D. Rus, and S. Singh, " Robot and Sensor Networks for First Responders ," *IEEE Pervasive Computing*, pp. 24–33, October-December 2004.

[11] W. B. Heinzelman, A. P. Chandrakasan, and H. Balakrishnan, "An Application-Specific Protocol Architecture for Wireless Microsensor Networks," *IEEE Transactions on Wireless Communications*, vol. 1, no. 4, pp. 660 – 670, Oct. 2002.

[12] W. Wang, V. Srinivasan, B. Wang, and K.-C. Chua, "Coverage for target localization in wireless sensor networks," *IEEE Transactions on Wireless Communications*, vol. 7, no. 2, pp. 667 –676, february 2008.

[13] N. Heo and P. Varshney, "Energy-efficient deployment of intelligent mobile sensor networks," *IEEE Transactions on Systems, Man and Cybernetics, Part A: Systems and Humans*, vol. 35, no. 1, pp. 78 – 92, jan. 2005.

[14] C. Chong and S. Kumar, "Sensor networks: evolution, opportunities and challenges," *Proceedings of the IEEE*, vol. 91, no. 8, pp. 1247–1256, August 2003.

[15] J. Lu and T. Suda, "Differentiated surveillance for static and random mobile sensor networks," *IEEE Transactions on Wireless Communications*, vol. 7, no. 11, pp. 4411 –4423, november 2008.

[16] T. Melodia, D. Pompili, V. Gungor, and I. Akyildiz, "Communication and coordination in wireless sensor and actor networks," *IEEE Transactions on Mobile Computing*, vol. 6, no. 10, pp. 1116 –1129, oct. 2007.

[17] J. Gu, S. Chen, and T. Sun, "Localization with incompletely paired data in complex wireless sensor network," *IEEE Transactions on Wireless Communications*, vol. 10, no. 9, pp. 2841 –2849, september 2011.

[18] M. Anisetti, C. Ardagna, V. Bellandi, E. Damiani, and S. Reale, "Map-based location and tracking in multipath outdoor mobile networks," *IEEE Transactions on Wireless Communications*, vol. 10, no. 3, pp. 814 –824, march 2011.

[19] C. E. Shannon, "Communication in the presence of noise," *Proc. Institute of Radio Engineers*, vol. 37, no. 1, pp. 10–21, January 1949.

[20] S. Thrun, "Robotic Mapping: A Survey," in *Exploring Artificial Intelligence in the New Millenium*.   Morgan Kaufmann, 2002.

[21] H. Durrant-Whyte and T. Bailey, "Simultaneous localization and mapping: part I," *IEEE Robotics Automation Magazine*, vol. 13, no. 2, pp. 99 –110, june 2006.

[22] H. D.-W. T. Bailey, "Simultaneous localization and mapping (slam): part II," *IEEE Robotics Automation Magazine*, vol. 13, no. 3, pp. 108 –117, sept. 2006.

References

[23] S. Thrun, W. Burgard, and D. Fox., *Probabilistic Robotics*. Cambridge, MA: MIT Press, 2005.

[24] S. Thrun, "Learning Occupancy Grids With Forward Sensor Models," *Autonomous Robots*, vol. 15, pp. 111–127, 2002.

[25] H. Durrant-Whyte and T. Bailey, "Simultaneous localization and mapping (slam): Part I," *IEEE Robotics & Automation Magazine*, vol. 13, no. 2, pp. 99–110, June 2006.

[26] T. Bailey and H. Durrant-Whyte, "Simultaneous localization and mapping (slam): Part II," *IEEE Robotics & Automation Magazine*, vol. 13, no. 3, pp. 108–117, 2006.

[27] S. Thrun, W. Burgard, D. Fox, H. Hexmoor, and M. Mataric, "A Probabilistic Approach to Concurrent Mapping and Localization for Mobile Robots," in *Machine Learning*, 1998, pp. 29–53.

[28] F. Dellaert, F. Alegre, and E. B. Martinson, "Intrinsic localization and mapping with 2 applications: Diffusion mapping and macro polo localization," in *IEEE Intl. Conf. on Robotics and Automation*, vol. 2, 2003, pp. 2344 – 2349.

[29] R. Sim, G. Dudek, and N. Roy, "A closed form solution to the single degree of freedom simultaneous localisation and map building (SLAM) problem," in *IEEE Conference on Decision and Control*, vol. 1, 2000, pp. 191–196.

[30] P. Krauthausen, F. Dellaert, and A. Kipp, "Exploiting locality by nested dissection for square root smoothing and mapping," in *Robotics: Science and Systems (RSS)*, 2006.

[31] M. W. M. G. Dissanayake, P. Newman, S. Clark, H. Durrant-Whyte, and M. Csorba, "A Solution to the Simultaneous Localization and Map Building (SLAM) Problem," *IEEE Transactions on Robotics and Automation*, vol. 17, no. 3, pp. 229–241, June 2001.

[32] M. Montemerlo, S. Thrun, D. Koller, and B. Wegbreit, "FastSLAM: A Factored Solution to the Simultaneous Localization and Mapping Problem," in *Proceedings of the AAAI National Conference on Artificial Intelligence*. AAAI, 2002, pp. 593–598.

[33] ——, "FastSLAM 2.0: An Improved Particle Filtering Algorithm for Simultaneous Localization and Mapping that Provably Converges," in *Proceedings of the Sixteenth International Joint Conference on Artificial Intelligence (IJCAI)*. Acapulco, Mexico: IJCAI, 2003.

References

[34] K. Murphy, "Bayesian Map Learning in Dynamic Environments," in *Advances in Neural Info. Proc. Systems (NIPS)*, San Mateo, CA, 1999, pp. 1015–1021.

[35] G. Grisetti, C. Stachniss, and W. Burgard, "Improved Techniques for Grid Mapping With Rao-Blackwellized Particle Filters," *IEEE Transactions on Robotics*, vol. 23, no. 1, pp. 34–46, Feb. 2007.

[36] R. Gartshore, A. Aguado, and C. Galambos, "Incremental map building using an occupancy grid for an autonomous monocular robot," in *7th Intl. Conf. on Control, Automation, Robotics and Vision*, vol. 2, Dec. 2002, pp. 613–618.

[37] G. Oriolo, G. Ulivi, and M. Vendittelli, "Real-time map building and navigation for autonomous robots in unknown environments," *IEEE Transactions on Systems, Man, and Cybernetics, Part B: Cybernetics*, vol. 28, no. 3, pp. 316 –333, jun 1998.

[38] H. Gonzalez-Banos and J. C. Latombe, "Navigation strategies for exploring indoor environments," *The International Journal of Robotics Research*, vol. 21, no. 10-11, pp. 829–848, 2002.

[39] R. Pito, "A solution to the next best view problem for automated surface acquisition," *IEEE Transactions on Pattern Analysis and Machine Intelligence*, vol. 21, no. 10, pp. 1016–1030, October 1999.

[40] J. J. Kuffner and S. M. LaValle, "RRT-connect: An efficient approach to single-query path planning," in *In IEEE Int. Conf. on Robotics and Automation*, April 2000.

[41] A. Ganguli, J. Cortes, and F. Bullo, "Maximizing visibility in nonconvex polygons: nonsmooth analysis and gradient algorithm design," in *Proceedings of the 2005 American Control Conference*, June 2005.

[42] R. Grabowski, P. Khosla, and H. Choset, "Autonomous exploration via regions of interest," in *Proceedings of the IEEE/RSJ International Conference on Intelligent Robots and Systems (IROS'03)*, October 2003.

[43] C. Debes, M. Amin, and A. Zoubir, "Target detection in single- and multiple-view through-the-wall radar imaging," *IEEE Transactions on Geoscience and Remote Sensing,*, vol. 47, no. 5, pp. 1349 –1361, may 2009.

[44] G. Alli and D. Difilippo, "Beamforming for through-the-wall radar imaging," in *Through-the-Wall Radar Imaging*, M. Amin, Ed.   Boca Raton, FL: CRC Press, 2011, ch. 3, pp. 81–119.

References

[45] G. Wang and M. Amin, "Imaging through unknown walls using different standoff distances," *IEEE Transactions on Signal Processing*, vol. 54, no. 10, pp. 4015 – 4025, oct. 2006.

[46] T. Dogaru and C. Le, "SAR images of rooms and buildings based on FDTD computer models," *IEEE Transactions on Geoscience and Remote Sensing*, vol. 47, no. 5, pp. 1388 –1401, may 2009.

[47] G. Alli and D. Difilippo, "Impulse SAR and its application for through-the-wall detection and identification of people and wepaons," in *Through-the-Wall Radar Imaging*, M. Amin, Ed.   Boca Raton, FL: CRC Press, 2011, ch. 10, pp. 345–377.

[48] E. Baranoski, "Through wall imaging: Historical perspective and future directions," in *IEEE International Conference on Acoustics, Speech and Signal Processing, ICASSP*, 31 2008-april 4 2008, pp. 5173 –5176.

[49] T. Ralston, G. Charvat, and J. Peabody, "Real-time through-wall imaging using an ultrawideband multiple-input multiple-output (mimo) phased array radar system," in *2010 IEEE International Symposium on Phased Array Systems and Technology (ARRAY)*, oct. 2010, pp. 551 –558.

[50] E. Baranoski, "Visibuilding: Sensing through walls," in *2006. Fourth IEEE Workshop on Sensor Array and Multichannel Processing*, july 2006, pp. 1 –22.

[51] M. C. Wicks, "RF tomography with application to ground penetrating radar," in *Asilomar Conference on Signals, Systems and Computers*, November 2007, pp. 2017–2022.

[52] J. Wilson and N. Patwari, "Radio tomographic imaging with wireless networks," *IEEE Transactions on Mobile Computing*, vol. 9, no. 5, pp. 621 –632, may 2010.

[53] M. Kanso and M. Rabbat, "Compressed RF tomography for wireless sensor networks: Centralized and decentralized approaches," in *IEEE Intl. Conference on Distributed Computing in Sensor Systems*, June 2009.

[54] D. Porrat and D. C. Cox, "UHF propagation in indoor hallways," *IEEE Transactions on Wireless Communications*, vol. 3, no. 4, pp. 1188–1198, July 2004.

[55] J. Tsao, D. Porrat, and D. Tse, "Prediction and Modeling for the Time-Evolving Ultra-Wideband Channel," *IEEE Journal of Selected Topics in Signal Processing*, vol. 1, no. 3, pp. 340–356, Oct. 2007.

[56] P. Kyritsi, D. C. Cox, R. A. Valenzuela, and P. W. Wolniansky, "Correlation Analysis based on MIMO Channel Measurements in an Indoor Environment," *IEEE*

Journal on Selected Areas in Communications, vol. 21, no. 5, pp. 713–720, June 2003.

[57] J. Ling, D. Chizhik, P. Wolinansky, R. A. Valenzuela, N. Costa, and K. Huber, "MIMO Measurement in Manhattan," in *13th IEEE International Symposium on Personal, Indoor and Mobile Radio Communications*, vol. 4, Sept. 2002, pp. 1631–1635.

[58] W. M. Smith, "Urban propagation modeling for wireless systems," Ph.D. dissertation, Stanford University, 2004.

[59] Y. Lustmann and D. Porrat, "Indoor Channel Spectral Statistics, K-Factor and Reverberation Distance," *IEEE Transactions on Antennas and Propagation*, vol. 58, no. 11, pp. 3685–3692, Nov. 2010.

[60] Adept Mobilerobots: http://www.mobilerobots.com/Mobile_Robots.aspx.

[61] Laird Technologies, 2010, http://www.lairdtech.com/Products/Antennas-and-Reception-Solutions/.

[62] N. Nakagami, "The m-distribution, a general formula for intensity distribution of rapid fading," in *Statistical Methods in Radio Wave Propagation*, W. G. Hoffman, Ed. Oxford, England: Pergamon, 1960.

[63] T. S. Rappaport, *Wireless Communications: Principles and Practice*. Upper Saddle River, NJ, USA: Prentice-Hall, 2001.

[64] H. Hashemi, "A Study of Temporal and Spatial Variations of the Indoor Radio Propagation Channel," in *5th IEEE International Symposium on Personal, Indoor and Mobile Radio Communications, 1994. Wireless Networks - Catching the Mobile Future*, vol. 1, Sept. 1994, pp. 127–134.

[65] V. Erceg, L. J. Greenstein, S. Y. Tjandra, S. R. Parkoff, A. Gupta, B. Kulic, A. A. Julius, and R. Bianchi, "An Empirically Based Path Loss Model for Wireless Channels in Suburban Environments," *IEEE Journal on Selected Areas in Communications*, vol. 17, no. 7, pp. 1205–1211, July 1999.

[66] S. S. Ghassemzadeh, L. J. Greenstein, A. Kavcic, T. Sveinsson, and V. Tarokh, "UWB Indoor Path Loss Model for Residential and Commercial Buildings," in *58th IEEE Vehicular Technology Conference, VTC*, vol. 5, Oct. 2003, pp. 3115–3119.

[67] Y. Mostofi, M. Malmirchegini, and A. Ghaffarkhah, "Estimation of Communication Signal Strength in Robotic Networks," in *Proceedings of IEEE International Conference on Robotics and Automation (ICRA)*, Anchorage, AK, May 2010, pp. 1946–1951.

References

[68] A. Ghaffarkhah and Y. Mostofi, "Channel Learning and Communication-Aware Motion Planning in Mobile Networks," in *Proceedings of the American Control Conference (ACC)*, Baltimore, MD, June 2010, pp. 5413–5420.

[69] ——, "Communication-Aware Motion Planning in Mobile Networks," *IEEE Transactions on Automatic Control*, vol. 56, no. 10, pp. 2478–2485, Oct. 2011.

[70] M. Gudmundson, "Correlation Model for Shadow Fading in Mobile Radio Systems," *Electronics Letters*, vol. 27, no. 23, pp. 2145–2146, Nov. 1991.

[71] F. Santosa and W. W. Symes, "Linear inversion of band-limited reflection seismograms," *SIAM Journal on Scientific and Statistical Computing*, vol. 7, no. 4, pp. 1307–1330, 1986.

[72] R. Gribonval and M. Nielsen, "Sparse representations in unions of bases," *IEEE Trans. on Information Theory*, vol. 49, no. 12, pp. 3320–3325, December 2003.

[73] E. J. Candès, J. Romberg, and T. Tao, "Stable signal recovery from incomplete and inaccurate measurements," *Comm. Pure Appl. Math*, vol. 59, no. 8, pp. 1207–1223, 2005.

[74] http://www.dsp.ece.rice.edu/cs/.

[75] M. Rudelson and R. Vershynin, "Sparse reconstruction by convex relaxation: Fourier and Gaussian measurements," 2006, preprint.

[76] W. B. Johnson and J. L. (editors), *Handbook of the Geometry of Banach Spaces*. North-Holland, Amsterdam: Elsevier Science Ltd, 2001, vol. 1,2.

[77] S. J. Szarek, "Condition numbers of random matrices," *J. of Complexity*, vol. 7, no. 2, pp. 131–149, 1991.

[78] A. E. Litvak, A. Pajor, M. Rudelson, and N. Tomczak-Jaegermann, "Smallest singular value of random matrices and geometry of random polytopes," *Advances in Mathematics*, vol. 195, no. 2, pp. 491–523, 2005.

[79] E. J. Candès, "The restricted isometry property and its implications for compressed sensing," *Compte Rendus de l'Academie des Sciences*, vol. 346, pp. 589–592, 2008.

[80] S. Boyd and L. Vandenberghe, *Convex Optimization*. Cambridge University Press, 2004.

[81] "ℓ_1 magic toolbox," http://www.acm.caltech.edu/l1magic/.

References

[82] S. Wright, R. Nowak, and M. Figueiredo, "Sparse reconstruction by separable approximation," in *IEEE International Conference on Acoustics, Speech and Signal Processing*, April 2008, pp. 3373–3376.

[83] M. Figueiredo, R. Nowak, and S. Wright, "Gradient projection for sparse reconstruction: Application to compressed sensing and other inverse problems," *IEEE Journal of Selected Topics in Signal Processing*, vol. 1, no. 4, pp. 586–597, Dec. 2007.

[84] Y. Nesterov, "Gradient methods for minimizing composite objective function," *Center for Operations Research and Econometrics Discussion Paper*, no. 76, 2007.

[85] J. Tropp and A. Gilbert, "Signal recovery from random measurements via orthogonal matching pursuit," *IEEE Trans. on Information Theory*, vol. 53, no. 12, pp. 4655–4666, December 2007.

[86] Y. Mostofi and P. Sen, "Compressed mapping of communication signal strength," proceedings of IEEE MILCOM 2008.

[87] C. Li, "An efficient algorithm for total variation regularization with applications to the single pixel camera and compressive sensing," Ph.D. dissertation, RICE University, 2009.

[88] Y. Wang, J. Yang, W. Yin, and Y. Zhang, "A new alternating minimization algorithm for total variation image reconstruction," *SIAM J. on Imaging Sciences*, vol. 1, no. 3, p. 248272, 2008.

[89] L. I. Rudin, S. Osher, and E. Fatemi, "Nonlinear total variation based noise removal algorithms," *Physica D*, vol. 60, pp. 259–268, November 1992.

[90] J. Romberg, "Compressive sensing by random convolution," *SIAM Journal on Imaging Science*, December 2009.

[91] D. Strong and T. Chan, "Edge-preserving and scale-dependent properties of total variation regularization," *Inverse Problems*, vol. 19, no. 6, p. S165, 2003.

[92] Y. Mostofi, A. Gonzalez-Ruiz, A. Ghaffarkhah, and D. Li, "Characterization and Modeling of Wireless Channels for Networked Robotic and Control Systems - A Comprehensive Overview," in *Proceedings of 2009 IEEE/RSJ International Conference on Intelligent Robots and Systems (IROS)*, St. Louis, MO, October 2009.

[93] A. Gonzalez-Ruiz, A. Ghaffarkhah, and Y. Mostofi, "A Comprehensive Overview and Characterization of Wireless Channels for Networked Robotic and Control Systems," *Journal of Robotics*, vol. 2011, 2011.

References

[94] A. C. Kak and M. Slaney, *Principles of Computerized Tomographic Imaging*. IEEE, 1988.

[95] R. Ketcham, *Computed Tomography for Paleontology and Geology*. Cambridge University Press, 2004.

[96] R. Ng, "Fourier slice photography," in *International Conference on Computer Graphics and Interactive Techniques, ACM SIGGRAPH*, 2005, pp. 735 – 744.

[97] S. Ji, Y. Xue, and L. Carin, "Bayesian Compressive Sensing," *IEEE Transactions on Signal Processing*, vol. 56, no. 6, pp. 2346–2356, June 2008.

[98] L. He and L. Carin, "Exploiting Structure in Wavelet-Based Bayesian Compressive Sensing," *IEEE Transactions on Signal Processing*, vol. 57, no. 9, pp. 3488–3497, Sept. 2009.

[99] M. E. Tipping, "Sparse Bayesian Learning and the Relevance Vector Machine," *J. Mach. Learn. Res.*, vol. 1, pp. 211–244, Sep. 2001.

[100] S. Ji, Y. Xue, and L. Carin, "Bayesian compressive sensing," *IEEE Transactions on Signal Processing*, vol. 56, no. 6, pp. 2346 –2356, june 2008.

[101] A. Goldsmith, *Wireless Communications*. Cambridge University Press, 2005.

[102] H. H. H. H. Gonzalez-Banos and J.-C. Latombe, "Navigation Strategies for Exploring Indoor Environments," *The International Journal of Robotics Research*, vol. 21, no. 10-11, pp. 829–848, Oct. 2002.

[103] D. Fox, J. Ko, K. Konolige, B. Limketkai, D. Schulz, and B. Stewart, "Distributed multi-robot exploration and mapping," *Proceedings of the IEEE*, 2006.

[104] W. Burgard, M. Moors, C. Stachniss, and F. Schneider, "Coordinated Multi-Robot Exploration," *IEEE Transactions on Robotics*, vol. 21, pp. 376–386, 2005.

[105] Robot Operating System (ROS): http://www.ros.org/wiki/.